Air Force Institute of Technology

AFIT Scholar

12-1995

Fatigue Response of Cracked Aluminum Panel with Partially Bonded Composite Patch

Jason J. Denney

Follow this and additional works at: https://scholar.afit.edu/etd

Part of the Mechanics of Materials Commons, and the Structures and Materials Commons

FATIGUE RESPONSE OF CRACKED ALUMINUM PANEL WITH PARTIALLY BONDED COMPOSITE PATCH

THESIS

Jason J. Denney, Captain, USAF

AFIT/GAE/ENY/95D-7

DEPARTMENT OF THE AIR FORCE

AIR UNIVERSITY

AIR FORCE INSTITUTE OF TECHNOLOGY

Wright-Patterson Air Force Base, Ohio

AFIT/GAE/ENY/95D-7

FATIGUE RESPONSE OF CRACKED ALUMINUM PANEL WITH PARTIALLY BONDED COMPOSITE PATCH

THESIS

Jason J. Denney, Captain, USAF
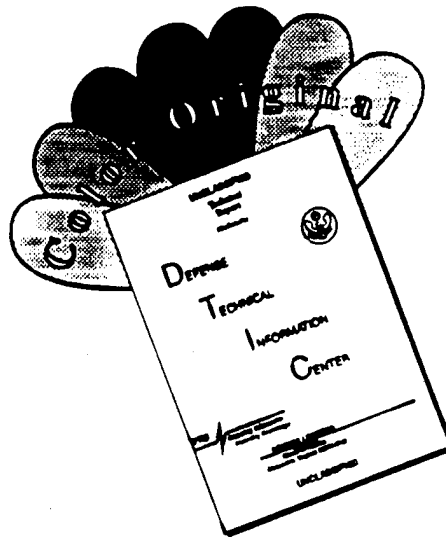
AFIT/GAE/ENY/95D-7

DISCLAIMER NOTICE

AFIT/GAE/ENY/95D-7

FATIGUE RESPONSE OF CRACKED ALUMINUM PANEL WITH PARTIALLY

BONDED COMPOSITE PATCH

THESIS

Presented to the Faculty of the Graduate School of Engineering

of the Air Force Institute of Technology

Air University

In Partial Fulfillment of the

Requirements of the Degree of

Master of Science in Aeronautical Engineering

Jason J. Denney, B.S.A.E.

Captain, USAF

December 1995

Acknowledgments

Table of Contents

List of Figures

viii

List of Tables

Abstract

More and more aircraft, both commercial and military, are being called upon to fly well beyond their economic and structural service lives. Budget cuts and dwindling new aircraft development has forced the United States Air Force (USAF) to look toward more reliable structural repairs. One of these repair techniques, which was the subject of this study, is the repair of metallic aircraft structures using high strength composite materials.

This study investigated the fatigue response of a precracked, 508x152x1 mm, 2024-T3 aluminum panel repaired with a partially bonded, unidirectional, three-ply boron/epoxy composite reinforcement with ply lengths of 68, 56 and 50 mm and a width of 50 mm. Intentional disbonds were created in the bondline of the repair using teflon inserts to simulate defects seen in real applications due to service conditions or during manufacturing. The repaired panels were subjected to constant amplitude fatigue testing at a peak load of 120 MPa to study the damage and fatigue tolerance of partially bonded composite reinforcements to cracked aluminum panels.

The effects of various disbond locations and sizes were investigated and compared to each other as well as to panels repaired with a completely bonded reinforcement and to cracked panels without any reinforcement. Five disbond locations were investigated. Also, the effect of disbond size varying from 5 to 20 % of the total bond area for a few cases of disbond location was investigated.

It was found that disbonds around the crack resulted in greater crack growth rates and reduced specimen life. The amount of patch efficiency reduction was a function of

how much of the crack was covered by the disbond during growth within the patch as well as the size of the disbond perpendicular to the crack. Disbonds at the longitudinal edges of the patch did not reduce patching efficiency, but instead, enhanced it by reducing the amount of parasitic load attraction into a shorter patch, i.e. a smaller region of higher stiffness. No growth of the pre-existing disbonds was observed, only cyclic disbonding in the wake of the crack tip was evident. Even with severe disbonds equal to 20 % of the total bond area, the patch repairs significantly improved the fatigue life of the cracked panels. A worst case of disbond was the full width of the repair which increased the life of the panel by eight times the life of the unrepaired panel and a completely bonded repair increased the panel life by approximately eleven times. In other words, repair and replacement of partially bonded patches are not necessary as these still provide adequate life improvement, at least for the configurations, material systems, and stress level used in this study.

In summary, the results of this study demonstrate that there is a definite variation in fatigue life depending on the location and size of the disbonds, however, crack growth characteristics also revealed that partially bonded composite repairs are fairly damage tolerant of pre-existing bondline disbonds.

Fatigue Response of Cracked Aluminum Panel with Partially Bonded Composite Patch

I. Introduction

Typically, commercial airframes are designed with economic service lives, the time at which repair and maintenance costs are too high for profitable operation, of twenty years. By the year 2000, over 5,700 commercial aircraft will be over twenty years old (11). As of 1993, fifty-one percent of the United States Air Force (USAF) fleet was over fifteen years old and forty-four percent of the USAF fleet was over twenty years old (21). Over such long years of service, many military and commercial aircraft have suffered structural damage from fatigue and stress corrosion due to their extended use and age. Therefore, the structural integrity of both commercial and military airframes has become a major concern. In response to this growing problem, the United States Government has placed the commercial aircraft industry under a microscope by instituting the National Aging Aircraft Research Program under the Federal Aviation Administration (FAA) and the Airframe Structural Integrity Program under the National Aeronautics and Space Administration (NASA). The USAF has also created its own Aging Aircraft Program to address concerns with older military aircraft (21).

The largest loss of life due to a single aircraft accident was determined by

investigators to be the result of an improperly performed structural repair on a Japan Air Lines Boeing 747 (15). In April 1988, Aloha Airlines' flight 243 suffered catastrophic failure of its forward fuselage as a result of fatigue cracking and served as a wake-up call for the aircraft industry to the problem of aging aircraft (10). With decreasing budgets and dwindling new aircraft development, the aging aircraft phenomenon has increased the interest of the USAF in the reliable structural repair of aircraft. Also with waiting periods of up to five years for new aircraft and costs of $35-40 million for a single new commercial aircraft, commercial airlines have additionally developed an increasing interest in better repair techniques (11). One of these repair techniques, which was the subject of this study, is the repair of metallic structures using high stiffness composite materials. This technique, commonly known as "Crack Patching," was pioneered by the Aeronautical and Maritime Research Laboratories (AMRL) in Australia. This highly effective repair technique has had considerable experience on military aircraft and has only just recently made its appearance in the commercial aircraft industry (13).

Most structural repairs today are still performed using bolted joints or doublers. These repairs are easy to fabricate and quick to install. They give the advantages that they can be subsequently disassembled if need be and they can be installed in an uncontrolled environment. However, bolted repairs require the machining of holes in the metallic structure which weakens the load carrying capability of the metallic members and creates concentrated stresses at the bearing surfaces resulting in local stress risers and future sites of fatigue damage. On the other hand, bonded repairs do not require any removal of the parent metallic structure, eliminating the possibility of future sites of fatigue damage.

Bonded composite repairs have proven to be as strong as or even stronger than bolted joints, making them a viable option to the aircraft repairer. Bonded composite patches have demonstrated their ability in reducing the stress intensity factor, K, as shown schematically in Figure 1, thus reducing the crack growth rate resulting in increased overall fatigue strength and extended structural service life (7). With a properly designed
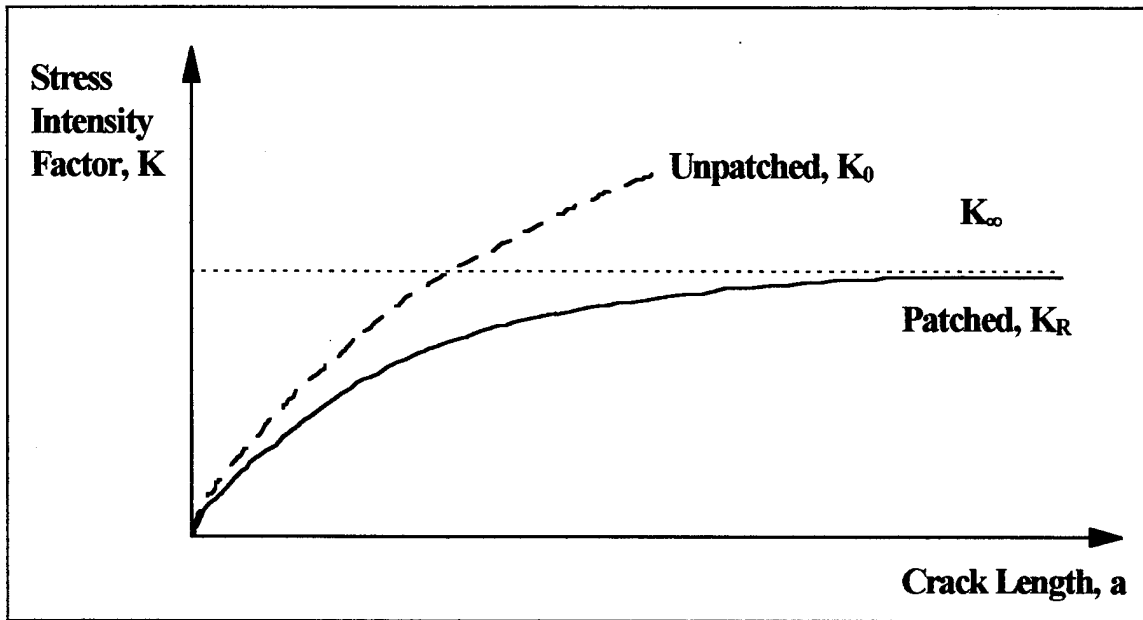
Figure 1. Reduction in Stress Intensity Factor with Repair (7)

patch, the stress intensity factor reaches a limiting value, K_∞, no matter what length the crack reaches. Further, a well designed patch significantly increases the time between inspection intervals as shown in Figure 2 (40). For the USAF this implies increased combat capability and decreased costs due to reduced downtime. Even with all these benefits of composite patching, this technique does have the drawback, i.e. it requires,
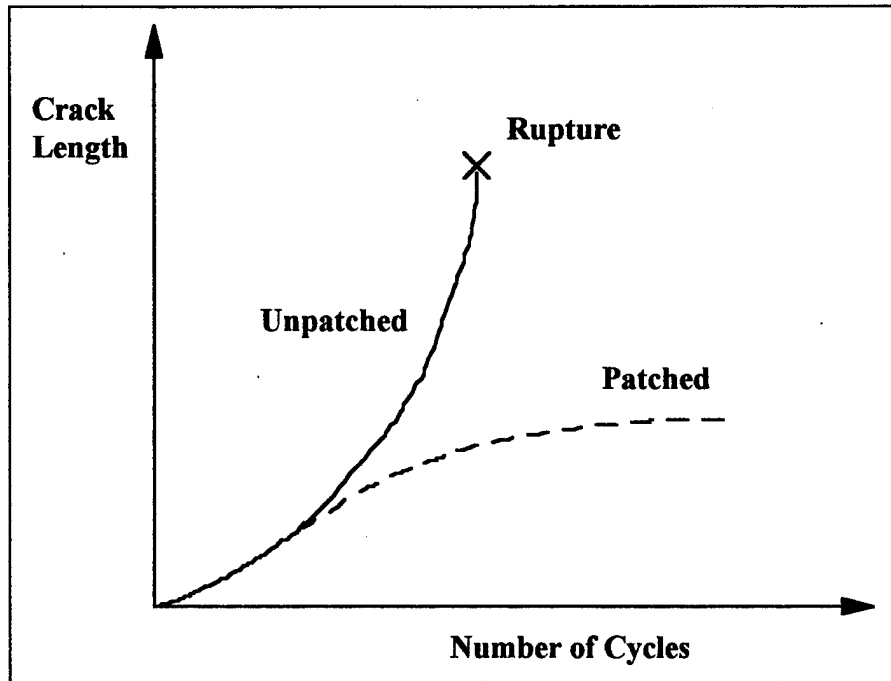
Figure 2. Effect of Patching on the Lifetime of a Cracked Structure (40)

extensive environment and process controls during bonding of the composite patch.

Cleanliness and moisture control is of utmost importance and if not given proper attention

may lead to defects/disbonds in the bondline between the adhesive layer and the metallic

adherend. This was the specific emphasis of this study.

This study was, therefore, conducted to investigate the effects of disbonds on the

fatigue response of cracked aluminum panels repaired with bonded composite patches.

For this purpose, the constant amplitude fatigue testing of precracked aluminum panels

with bonded boron/epoxy composite patches was performed. Intentional disbonds were

created in the bondline of the repair using teflon inserts. This study revealed the damage

and fatigue tolerance of partially bonded composite patches to cracked aluminum panels.

The effects of various disbond locations and sizes were studied and compared to each other as well as to panels with a completely bonded patch and to cracked panels without any patch, thus characterizing the effects of disbond size and location on fatigue crack growth.

This study involved the testing of five different intentional disbond configurations as shown in Figure 3: (1) a completely bonded patch (CBP); (2) a full width disbond (FWD) extending the full width of the patch and covering the crack; (3) crack tip disbonds (CTD) at both ends of the crack; (4) end disbonds (ED) at each end of longitudinal axis of the patch covering the tapered ends of the patch; and (5) a center disbond (CD) over the crack length. Also, a baseline configuration with no bonded repair was tested for comparison purposes. Various disbond sizes and shapes were also investigated. With the configurations listed above, disbond areas of 20%, 10%, and 5% of the total bond area of the patch were investigated depending on the location of the disbond and its severity. Additionally, various stress levels, crack lengths, stress ratios, and a high and low modulus adhesive were investigated. The aluminum adherend was a aluminum 2024-T3 panel with nominal dimensions of 508x152x1 mm. The patch was a three ply boron/epoxy composite with ply lengths of 68, 56 and 50 mm and a width of 50 mm.

The results of this study show that there is a definite variation in fatigue life depending on the location and size of the disbonds. However, the growth characteristics of the cracked aluminum panels demonstrated that bonded composite repairs with disbonds are not as critical as currently perceived, depending on the size of the disbond

5

(1) Completely Bonded Patch (CBP)

(2) Full Width Disbond (FWD)

(3) Crack Tip Disbonds (CTD)

(4) End Disbonds (ED)

Disbonds

(5) Center Disbond (CD)
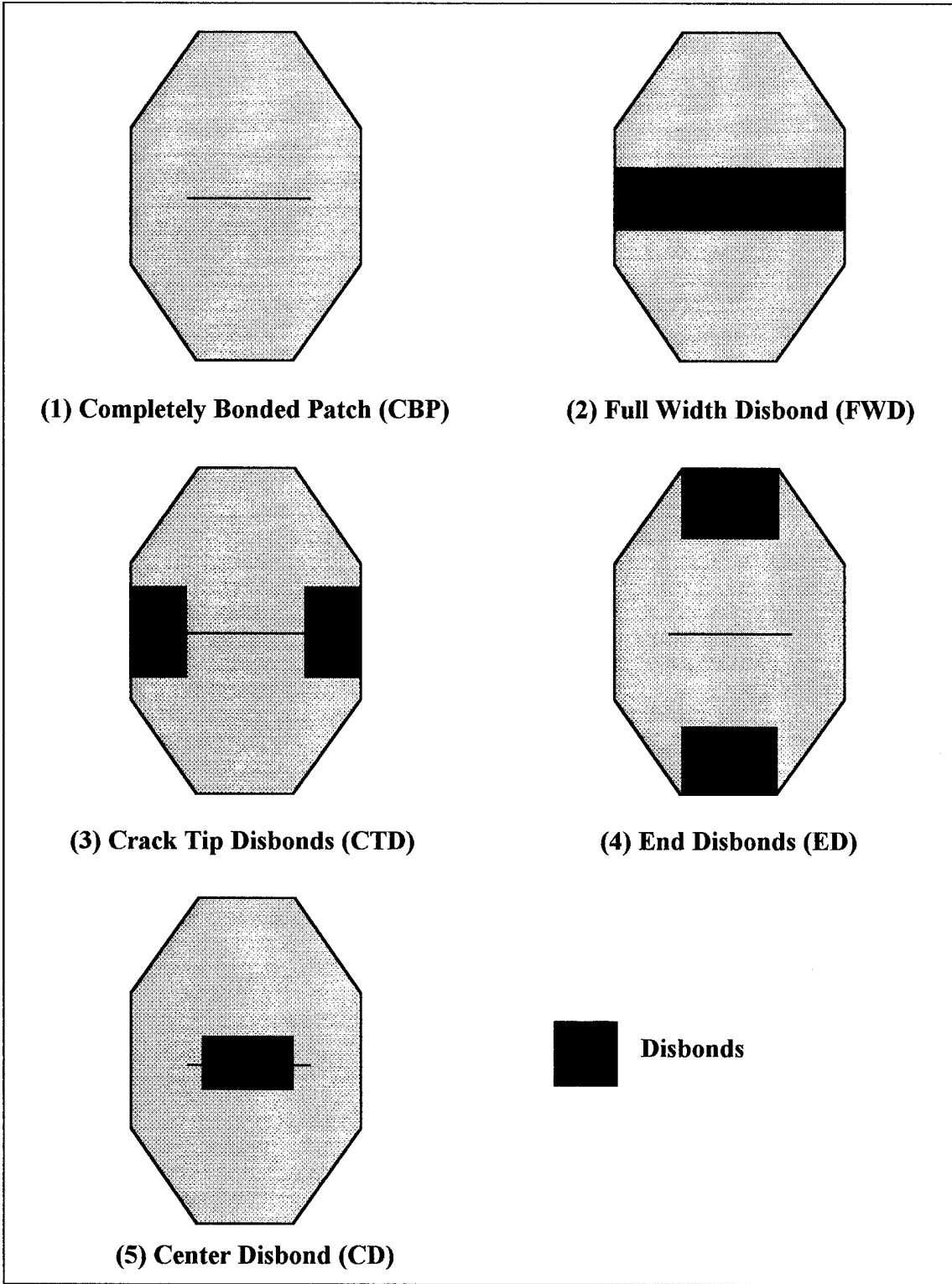
Figure 3. Disbond Configurations

and its location. This will save excessive cost and reduce aircraft downtime,

thus improving the Air Force's sustainability of air power as well as saving commercial

airlines lost revenues. Finally, a simple damage tolerance approach is presented to account

for the disbond in the bondline of the bonded composite patch when employed to repair

cracked aluminum aircraft structures.

II. Background

In the early 1970's the Aeronautical and Maritime Research Laboratories (AMRL), Australia, pioneered a method to repair fatigue and stress corrosion cracking in metallic aircraft structures using adhesively bonded high strength composites. This technique, also known as "Crack Patching," has proven to be highly cost-effective and efficient compared to conventional mechanically fastened repairs (41). Repairs to Royal Australian Air Force (RAAF) aircraft have performed exceptionally well and without incident (6, 7).

"Decreases in the availability of government funding and world arms inventories are requiring the extension of existing aircraft service life. Service Life Extension Programs are becoming more evident as older aircraft are being utilized long beyond their original design and service lives" (11:248). This situation is no more prevalent than for the USAF whose own repair and maintenance goals require increased combat capability through extended structural service lives, reduced manpower requirements and decreased costs through simplified repairs and reduced downtime (3). The implementation of adhesively bonded high strength composite repairs will provide relief, if not a solution, to all of the above concerns.

Applications of Bonded Technology and Repairs

The use of adhesive bonding as a joining method is an accepted means of attaining

high structural efficiency and durability. Adhesive bonding in building construction, sporting goods, automobiles, clothing repair and aircraft structures are just a few of the many areas where it has made its appearance. Bonding of high strength composites is especially prevalent in sporting goods such as tennis racquets, fishing rods, golf club shafts and both water and snow skis (11). The Australians have even reinforced the superstructure of the Royal Australian Navy FFG-7 frigate using a 5x1 m carbon composite doubler to reduce the cyclic stresses causing cracking in welded joints (20). Just recently, the Wright Laboratory's Materials Directorate at Wright-Patterson Air Force Base, Ohio, has employed graphite/epoxy doublers to reinforce concrete bridge support beams in rural southwestern Ohio, thus opening a low-cost and efficient way to repair thousands of substandard bridges across the United States. Testing is also underway, with promising results, demonstrating that high strength composites could also be used to wallpaper the inside of federal buildings making them more resistant to terrorist bombings (19).

For many years adhesive bonding has been adopted as a method of achieving high structural efficiency and improved fatigue life in aircraft construction, especially in aircraft secondary structure. Sixty-two percent of the Boeing 747 wetted area, the area that would get wet if the aircraft is submerged in water, is adhesively bonded structure. The Lockhead C5A contains 3,250 m^2 (35,000 ft^2) of bonded structure. Also, some selected aircraft employ adhesive bonding of primary structure such as wing stiffeners, fuselage longerons and fuselage skin panel splice areas. The most significant of these aircraft, having over twenty-five years of successful service, is the Fokker F-27 aircraft (25). Now

this highly effective method of joining structure has added the repair of damaged metal components using high strength composites to the arsenal of aircraft maintenance personnel.

Some applications and demonstrator programs using adhesively bonded high strength composite repairs are listed in Table 1 (6). The first application of this technique was on the General Dynamics F-111 fighter/bomber wing pivot fitting that dates back to 1971. This repair employed a boron/epoxy doubler and in the twenty plus year life of this repair no doubler has ever debonded from this pivot fitting (6). Other primary applications of this repair technique include the Grumman F-14 fighter horizontal stabilizer, the McDonnell Douglas F-15 empannage skins, the Rockwell B-1 dorsal longeron, the Dessault Mirage 2000/4000 rudder, and the Sikorsky Blackhawk main blade and stabilizer reinforcement (11).

Mechanically Fastened versus Bonded Repairs

Compared to the more conventional mechanical repair methods such as riveting and bolting, adhesively bonded repairs provide a more uniform and efficient load transfer into the repair from the cracked structural component. Having yet to be totally accepted by the commercial airlines, adhesively bonded repairs have had considerable experience and experimentation on military aircraft throughout the world. The primary goal of any repair applied to an aircraft structure is to eliminate crack growth or at least to reduce it to the extent that the structure's service life and integrity is restored. Much practical experience and experimental evidence exists demonstrating that "bonded repairs are

10

Table 1. Aircraft Applications and Demonstrator Programs (6)

Aircraft	Problem	Remarks
C130	Stress corrosion cracking in wing stiffeners	Over 3000 repairs. No crack growth in 19 years of service.
Macchi	Fatigue cracking in landing wheel	Life doubled
Mirage III	Fatigue cracking in lower wing skin	180 wings repaired or reinforced
F111-C	Secondary bending of wing pivot fitting leading to fatigue cracking	30% strain reduction in critical region. 18 aircraft reinforced to date.
F111-C	Stress corrosion cracking in weapon longeron flange	More than 10 aircraft repaired. no anomalies after five years of operation.
C-141 (USAF)	Fatigue cracking in wing riser weep holes	55 aircraft repaired. Over 260 patches applied.
F/A-18	Fatigue cracking in fatigue test bulkhead	Doubler withstood over 10,000 hours of severe cyclic loading.
Bell 206	Demonstration repair of blade near tip	1400 hours of operation
Boeing 747	Simulated repairs to several regions including fuselage lap-joint, wing leading edge, trailing edge flap and engine thrust reversal cowl.	Demonstrator repairs; 12,600 flying hours and 2,660 landings with no anomalies
Boeing 767	Corrosion damage in fuselage keel beam	Demonstrator repair experienced, 8,300 flying hours, 5,900 landings with no anomalies
Boeing 727	Simulated damage in fuselage lap seam region	Demonstrator repair; 5,570 flying hours and 4,670 landings with no anomalies
Airbus A340 (Test fuselage)	Repairs to saw cuts in lap seam joint representing multi-site damage.	Patches have survived over 28,000 pressurization cycles to date with no disbonding or crack growth
Being 747-400 series (Test fuselage)	Repairs to fatigue cracks in a range of locations in the forward fuselage, including a shear tie, door skin and fuselage skin.	Repairs (other than one frame) withstood over 20,000 pressurization cycles with no crack growth or disbonds.

substantially more effective in retardation of crack growth than conventional mechanically fastened repairs" (41:1).

Both mechanically fastened and adhesively bonded repairs have proven to be effective, but each offers advantages and disadvantages over the other. Following is a discussion of the advantages and disadvantages of each, showing that when adhesively bonded repairs are applicable in a certain situation, the advantages far exceed those of mechanically fastened repairs.

Advantages of Adhesively Bonded Repairs. Most importantly, bonded repairs eliminate stress concentrations at fastener holes by distributing the load more evenly over a greater area, thus increasing the overall fatigue life of the repaired structure. Bonded composite repairs are lighter and thinner (1/3 to 1/2 as thick) than comparable bolted metallic repairs due to their higher stiffness. This results in significant weight savings and more aerodynamic repairs. Bonded composite repairs offer tailorable properties allowing them to conform to complex contours and meet varying stiffness requirements in different directions. Variable stiffening reduces unwanted parasitic load into the repaired region. Bonded repairs are corrosion resistant once installed as the cured bondline acts as a sealant against environmental effects. In service Nondestructive Inspection (NDI) is possible using ultrasonic techniques for bondline integrity inspection. For non-conducting composite laminates, eddy current may be utilized to monitor the condition of the underlying structure for crack growth or additional cracking. Selected composites eliminate galvanic corrosion by not forming a galvanic couple when in contact with metal surfaces, although, other composite materials may be isolated from the metal with a thin

12

layer of glass fabric. Finally, quick aircraft repair is possible at both depot and field repair levels, especially with low temperature cure adhesives (3, 7, 11, 13, 25, 41).

Advantages of Mechanically Fastened Repairs. Probably the most important feature of mechanically fastened repairs is that they are easy to fabricate and quick to install. This makes them more suitable for battle operational level repairs in combat situations. They also give the advantage that they can be subsequently disassembled if need be and that they can be assembled in an uncontrolled environment (25). These features make them cheap and less complicated. That is why mechanically fastened repairs have been so popular in the past.

Disadvantages of Adhesively Bonded Repairs. Although bonded repairs are relatively simple to install, stringent cleaning and process steps within a controlled environment lead to a greater chance of error during installation. The development of adverse residual stresses due to possible coefficient of thermal expansion (CTE) mismatch between the adherends being bonded is also of concern (6). Curing time can cause problems, especially to commercial airlines who lose hundreds of thousands of dollars a day in lost revenues when certain repairs require extensive curing for bondline durability. Technicians must be certified due to the fact that this technology is still being introduced in some areas and also because of the increased environmental and process controls. Bonded repairs cannot be used in cases where high service temperatures are expected because bondline durability will be reduced. And if the situation arises, the bonded repair cannot be easily removed if the need arises (3, 6, 13, 25).

Disadvantage of Mechanically Fastened Repairs. Mechanical fastener/bolt holes weaken the load carrying capability of the primary structure. Holes produce stress concentrations at the bearing surfaces, potentially creating future sites of fatigue damage. Also, the machining of fastener holes may create additional damage to underlying hydraulic lines, electrical wiring and other mechanical and structural components on the side opposite that being repaired. Finally, the potential for corrosion under the repair exists when employing mechanical repairs (11, 25).

Design, Materials and Surface Preparation for Adhesively Bonded Repairs

Design of Adhesively Bonded Repairs. "The goal of a properly designed repair is to restore the damaged structure's ultimate load carrying capability. Damage growth should either be arrested or significantly retarded. The repair must be carried out without causing further damage or creating a new weak link in the structure. In short, the repair allows the structure to fulfill its original intended function" (15:68).

Shear and normal loads or a combination of them, peel and cleavage loading, make up the primary loads acting on adhesive bonds as shown in Figure 4 (15). An ideal repair would eliminate peel and cleavage loading. However, minimizing their effects using good repair practices is the best that can be done. A single-sided lap-joint, the configuration investigated in this effort, creates unwanted secondary bending moments due to the offset of the neutral axis. These bending moments create high peel forces at the ends of the repair which also happens to be the location of highest shear. Tapering the repair ends and increasing the overlap length, one-half the longitudinal length, of the repair reduces
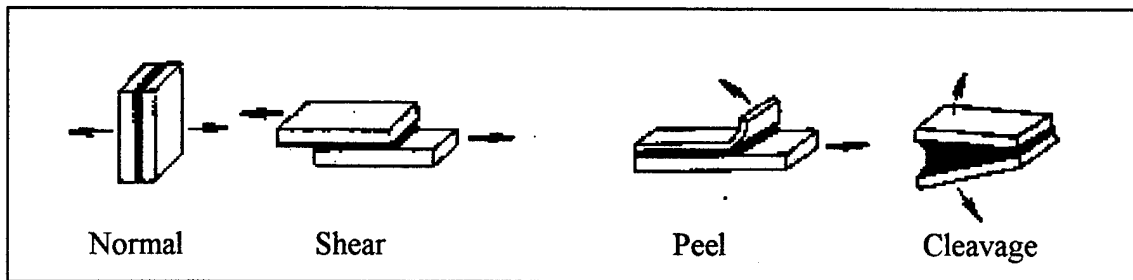
Figure 4. Loading on Adhesive Bonds (15)

the effects of peel (15, 22).

Maximum effectiveness of bonded repairs to cracked metallic structures can be achieved if the designer practices the following basic techniques:

- Select a repair material that has at least the static load capability of the metal being reinforced.

- Use a double-lap as compared to a single-lap repair, when possible, to reduce out of plane secondary bending.

- If using a composite repair material, use an overlap length of at least 30 times the repair thickness for a double-lap joint and 80 to 100 times the repair thickness for a single-lap joint.

- Use a stiffness ratio, $E_R t_R / E_P t_P$, greater than 1, where $E_R t_R$ is the repair stiffness and $E_P t_P$ is the plate stiffness.

- Taper the ends of the repair to reduce peel loading effects (15).

Materials. Major material properties of concern in a bonded repair, given that the parent materials are set, are the elastic modulus and strength of the reinforcement, and the adhesive shear modulus and strength.

With the development of high strength composites, repairers have exploited this

15

technology to create stronger, lighter, thinner, and more durable repairs. Increasing the elastic modulus, E, resulting in an increase in patch stiffness, $E_R t_R$ (patch modulus times patch thickness), will reduce the stress intensity factor, the adhesive stress as well as the stress in the repair. Therefore, for the most aerodynamic repairs, patch materials must have the highest modulus possible. However, benefits from increasing the stiffness of the repair material diminish with increasing thickness. High modulus composite fiber systems like boron/epoxy are most beneficial for thin repairs while cheaper more compliant fiber systems should be used for thicker repairs (41). With thinner repairs also comes the added benefit of less secondary bending due to minimum offset of the neutral axis, again making high modulus systems more attractive. Some patch materials and their properties are shown in Table 2, where the subscript L designates longitudinal properties and the subscript T designates transverse properties.

Table 2. Patch Materials (15, 26)

Patch Material	E_L / E_T (GPa)	Poisson Ratio	CTE, α_L ($10^{-6}/°C$)	Strength (MPa)
2024-T3	72.4 / 72.4	.33	22.7	324
Boron/Epoxy	210 / 25	.168	4.5	1590
GLARE 2	65.6 / 50.7	.33	17.9	390
Graphite/Epoxy	138 / 14.5	.20	-1	1447
Glass/Epoxy	50 / 14.5	.30	6.1	1130

Selection parameters for adhesives are shear strength and modulus. High adhesive shear modulus reduces the stress intensity factor, and both adhesive and repair patch stresses. A low adhesive shear modulus will create a compliant repair resulting in a

greater crack opening displacement of the crack faces giving greater crack growth rate. Finally, a high shear strain capability improves the efficiency/performance of the repair (41).

Required adhesive cure temperature should also affect the decision of what adhesive to use. Higher temperature adhesives usually exhibit high strength and durability while low cure temperature adhesives exhibit poor environmental durability. Although high cure temperature adhesives exhibit favorable properties, their application warrants heating of the aircraft parent material resulting in post cure residual thermal stresses in the repair domain as well as possible damage to underlying systems due to heat exposure. Low cure temperature adhesives, even with less favorable properties, lend themselves to operational, battle damage type applications where cure equipment is scarce and time is of the essence. Whenever possible, high cure temperature adhesives should be employed (41).

Adhesives for structural bonding can be separated into three main physical forms: (1) film adhesives; (2) paste adhesives; and (3) foam adhesives. Film adhesives are supplied in a tape form which gives the advantage of bondline thickness uniformity making them easy to apply. The major disadvantages of film adhesives is that they are expensive, need heat and pressure during cure, and require refrigerated storage. A film adhesive was the primary adhesive used in this study. Paste adhesives are available in both one and two-part form, and are designed to be applied by a spatula or other spreading equipment. These adhesives lend themselves to human error due to nonuniformity of the bondline and improper mixing when using two-part forms. They do, however, lessen the requirement

for refrigerated storage and can be cured at both room and elevated temperature. This makes them attractive for operational applications. Two specimens investigated in this study used a two-part paste adhesive. Foam adhesives are designed with foaming agents that make them expand during cure. Therefore, they are used to fill gaps and voids in damaged splice areas (25). Some examples of film, paste and foam adhesives are shown in Table 3.

Table 3. Adhesives (25)

Adhesive	Adhesive Type	Supplier	Cure Time/Temp	Storage
AF-163-2	Film	3M	1 hr/121 °C	6 months/-18 °C
FM-73	Film	American Cyanamid	1 hr/121 °C	6 months/-18 °C
FM-300	Film	American Cyanamid	1 hr/177 °C	6 months/-18 °C
EA-9309	Paste (two-part)	Dextor Corp/ Hysol	3 days/room temp or 1 hr/66 °C	12 months/room temp
EC-1386	Paste (one-part)	3M	1 hr/177 °C	4.5 °C or below
FM-39	Foam	American Cyanamid	1 hr/121 °C	6 months/-18 °C
AF-3002	Foam	3M	1 hr/°C	6 months/-18 °C or 7 days/24 °C

Surface Preparation. "The prebond surface preparation of metallic adherends is the most critical step in the adhesive bonding process. If not done correctly, all else is for naught" (32:28). Bond durability is dependent on the stability and bondability of the adherend surfaces. In other words, the shear strength of the bond is highly dependent on the surface preparation. The most durable bonds are achieved by adherends with high

surface roughness and the ability to mechanically interlock with the adhesive. To achieve this, adherend surfaces are chemically or mechanically abraded. Grit blasting was employed in this effort. Finally, the goal of surface preparation is to form an oxide film on the adherend surfaces that will remain stable during the useful life of the adhesive bonded structure (32).

The USAF operational procedures have separated the repair of aircraft structural components into three distinct categories: (1) depot level; (2) field/base level; and (3) battle operational level. With this the USAF's Primarily Adhesively Bonded Structure Technology (PABST) program evaluated a number of surface preparations for aluminum alloys. The PABST program concluded that Boeing's phosphoric acid anodize (PAA) surface treatment is the most durable treatment for aluminum alloys currently available. This treatment is primarily a depot level process because the adherends must be immersed into a PAA bath. As a result, the USAF developed a non-tank version of PAA known as the phosphoric acid non-tank anodizing process (PANTA) and equipped all of its depots and some base level facilities. The PABST program also evaluated less durable but, in some cases, more workable surface treatments that are used on USAF aircraft today (32).

This study involved a field level surface treatment using a silane coupling agent. At a minimum, field level treatments involve solvent degreasing, mechanical abrasion (Scotch Brite, grit blasting, etc.) and a degreasing primer. A one percent solution of silane in distilled water is brushed onto the bond surface chemically linking with the metal. Tests have shown comparable results with the PANTA process for 2024-T3 aluminum. This surface treatment process is simple and eliminates the need for more complex equipment

and procedures as required by the PANTA process (41). More details of the treatment and processes used in this study are presented in chapter three.

Past Studies/Efforts

Bonded reinforcement of cracked metallic components using high strength composite materials has proven to be highly effective in reducing the stress intensity factor. This reduction in stress intensity factor is the result of: (1) reduced stress at the crack tip by transferring load to the patch; and (2) bridging of the crack faces. Earlier studies were primarily aimed at the determination of the stress intensity factor of cracked components repaired with bonded patches, henceforth referred to as the repaired stress intensity factor, K_R, and the related crack growth rate, da/dN, i.e. the repair patch efficiency. These early efforts concluded that patching efficiency, with bonded reinforcements, is very high as compared to unpatched specimens. High efficiency has two major benefits in regards to crack growth: (1) retard re-initiation of crack growth; and (2) reduce the rate of crack growth once growth resumes (8). As a result, extensive government and industry exploratory programs were initiated to increase the knowledge base of this relatively new, but, highly effective repair technology.

Much of the early work was accomplished by Australia's AMRL. The Australians have employed bonded composites to stiffen underdesigned regions, restore strength/stiffness and to reduce stress intensity. Even though the concept of bonded reinforcement is simple, the Australians have invested much time and effort into the research and development (R&D) of such areas as computation of patch efficiency,

material allowables for repairs, surface treatment, adhesive characterization, optimization of curing conditions, repair analysis, evaluation, and repair application through extensive demonstrator programs, some of which are shown in Table 1 (6). The USAF has also initiated R&D efforts that have improved adhesives, primers, surface preparation as well as improving laboratory testing to more closely simulate service conditions. Also, NDI techniques for adhesive bonds have been vastly improved. One example of this technology thrust was in February 1975, where under contract to the USAF, Douglas Aircraft Company initiated the Primarily Adhesively Bonded Structure Technology (PABST) program, a technology validation program for adhesively bonded structures (2).

Much effort has been invested in understanding the mechanics of bonded repairs through modeling and experimentation. Many models have been proposed including analytical and finite element models. Probably the most well known analytical model for estimating the patch efficiency is the Rose model (33, 34, 35), to be discussed later. Two finite element models of particular importance, especially in estimating out of plane bending effects, have been proposed by Ratwani (31) and Sun and Arendt (38). Thermal mismatch effects have been experimentally and analytical characterized by Baker (7) and Rose (34). Also, recent experimental efforts by Fredell have reduced thermal mismatch effects by employing patch materials possessing similar thermal properties as of the parent structure (16, 17, 18). The list of past studies is endless, therefore, the rest of this section is devoted to those studies/conclusions most pertinent to this effort.

Rose, in his development of an analytical model to characterize bonded reinforcement behavior, to be discussed later, stated that the repaired stress intensity

factor range, ΔK_R, for a repaired component is independent of crack length. As a result, the crack growth rate, da/dN, within the repair is also independent of crack length as per the well known empirical relation da/dN $\propto (\Delta K)^n$. This is based on the assumption, by Baker and Rose, that the crack growth law for unrepaired cracks also holds for repaired cracks (8, 33). Baker corroborated this by demonstrating that well bonded repairs with no disbond growth exhibit constant crack growth within the repair (6).

Baker has shown through experiment and analysis that the rate of crack growth can be ranked according to the size of the disbond present. He demonstrated, using teflon inserts and an edge cracked specimen, that patching efficiency falls dramatically for a disbond over the crack as the disbond size increases perpendicular to the crack as shown in Figure 5 (6). He also stated that disbonds in front of the crack tip had little effect on the rate of crack propagation. Post-test investigation of the disbonds revealed minor, if any, disbond growth. This lack of disbond growth resulted in a constant repaired stress intensity factor range, ΔK_R, and crack growth rate, da/dN (6).

For nominally patched specimens, with no disbonds, Baker has also shown experimentally and analytically that patching efficiency is reduced by cyclic disbonding of the bonded patch repair. He showed that disbonding occurred in the wake of the crack tip as the crack propagated and that the cyclic disbonds appeared wedge or elliptical in shape. The disbond occurred in the composite-adhesive interface due to a combination of the adhesive properties, as suggested by Russell and to be discussed next, and a very light scrim of glass cloth impregnated within the matrix epoxy resin of the boron/epoxy which acts as a weak link under loading. With decreasing patch efficiency, the repaired stress
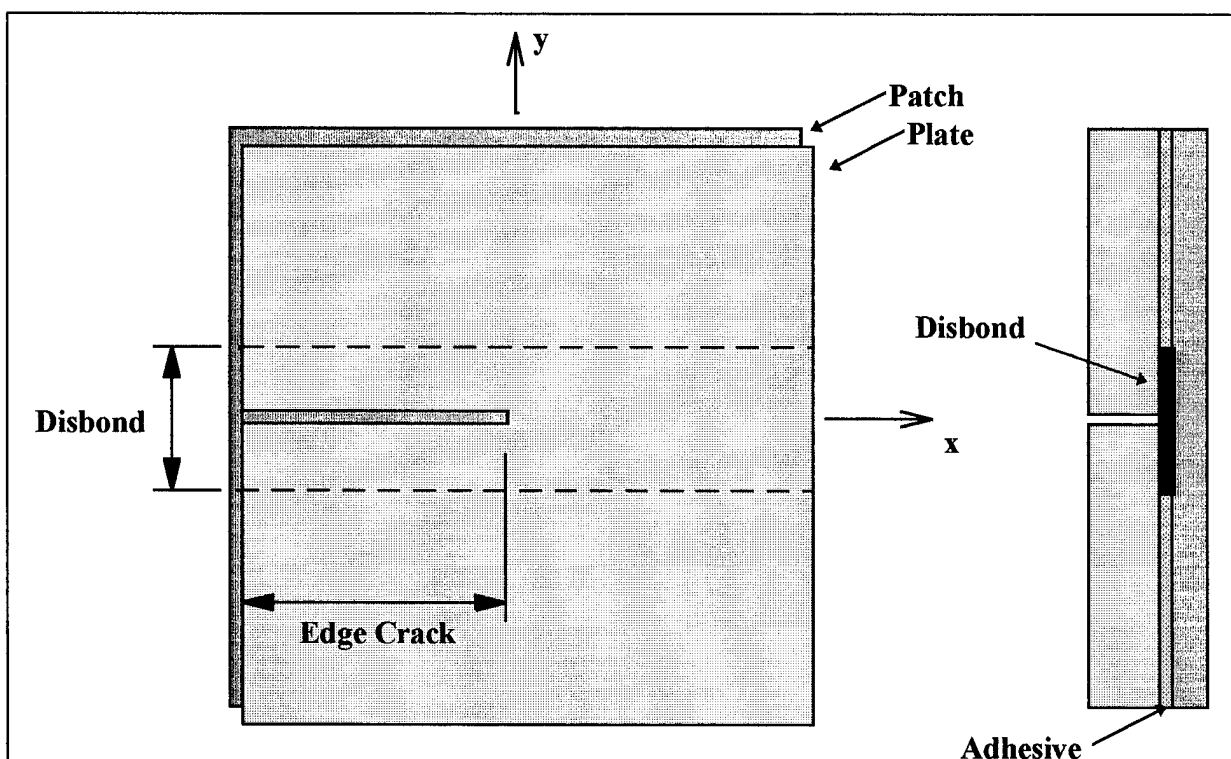
Figure 5. Disbond Configuration Studied by Baker (6)

intensity factor range, ΔK_R, increases and the crack length versus cycles curve takes on the more characteristic parabolic shape as in the case of unrepaired cracked structures, however, the repaired da/dN is still significantly less than that for an unrepaired case (6, 8).

Russell considered the influence of adhesive modulus on damage. Russell theorized that high modulus adhesives concentrate stresses at the repair-adhesive interface resulting in high adhesive strains. The high adhesive strains encouraged cohesive failure of the repair-adhesive bond rather than disbonding due to cracking in the adhesive (36). This explained the more noticeable disbonding, between the patch and the adhesive, in Baker's

experiments using high modulus film adhesives as compared to those conducted with low modulus acrylic adhesives (8).

As a result of testing under the PABST program, Hart-Smith stated that adhesive bonds are far more tolerant of flaws and porosity than had previously been believed, especially for thin aluminum panels. For the thinnest aluminum panels, the shear strength of the bond far exceeds that of the parent aluminum structure. The adhesive bond is not the weak link and the parent aluminum panel will yield long before the bond fails under increasing load. As a result, the adhesive bond is damage tolerant to small disbonds as long as the size of the disbond does not decrease the bond strength below that of the adherends. During testing of PABST fuselage splice joints, three disbonds were tested with no decrease in joint strength and no increase in maximum adhesive shear stress or strain. Hart-Smith also stated that most disbonds can go unrepaired except those at edges of the bonded joint. Even in this case a sealant, not an adhesive, is used to protect the remaining bondline from environmental attack. Disbonds become increasingly prevalent with thicker structures that are more highly loaded than thinner aluminum structures (22).

As stated previously, a good bonded repair either retards and/or significantly reduces the rate of crack growth once growth is initiated (Figure 6). Baker has shown that specimens repaired with high temperature cure adhesives , such as film adhesives, exhibit significantly less retardation. This retardation, or lack of it, is associated with the plasticity at the crack tip prior to patching. The use of elevated cure temperatures was found to anneal out the beneficial compressive stresses within the crack tip plastic zone allowing a much earlier re-initiation of crack growth. Baker showed that low cure
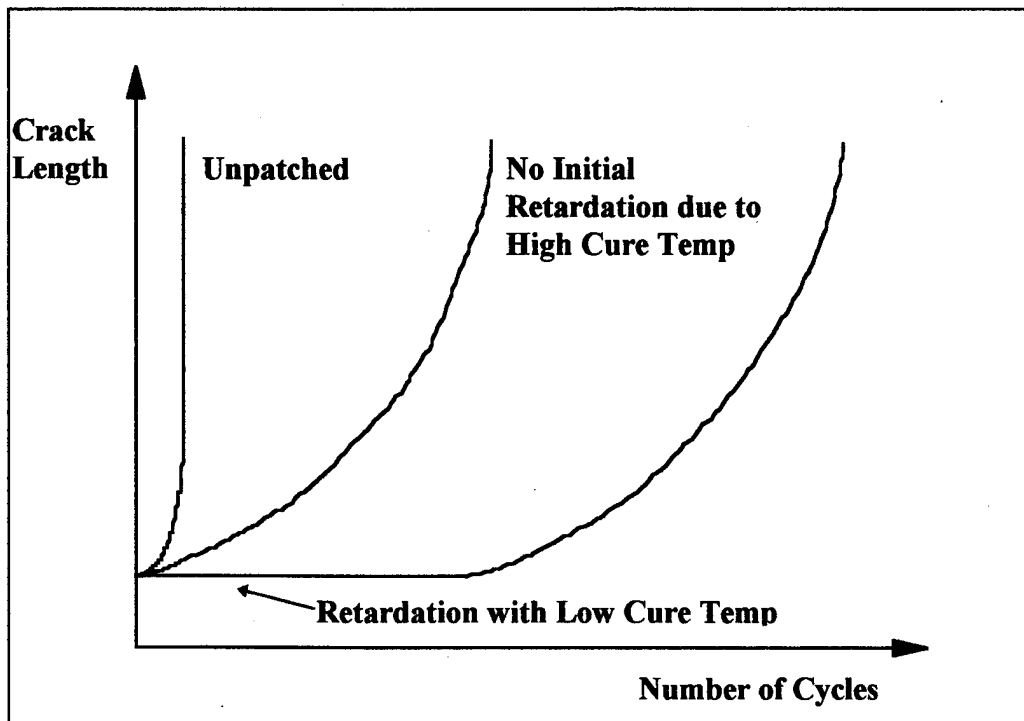
Figure 6. Effect of Adhesive Cure Temperature on Crack Retardation.

temperature acrylic adhesives had extensive retardation as compared to high cure

temperature film adhesives (6, 7, 8).

A joint effort between the United States Air Force Academy (USAFA) and the

Delft University of Technology, the Netherlands, has been ongoing to develop a user-

friendly crack patching analysis program to be ultimately used by maintenance personnel in

the repair of metallic airframes. A DOS version was originally developed at the Delft

University of Technology with a windows version currently being developed at the

USAFA. The program is called CalcuRep and is based on the Rose model to be discussed

later. The main outputs of the program are the repaired stress intensity factor, K_R, the

maximum stress in the patch repair, the maximum stress in the repaired metallic structure, the maximum shear strain in the adhesive, and the load transfer length in the adhesive bond (40).

Theoretical Analysis

Rose Model. A variety of models exist, both finite element and analytical, that mathematically characterize bonded reinforcements. The analytical model presented here, based on the original inclusion analogy by Muki and Sternberg (28), was developed by Rose of the AMRL, Australia, and is known as the Rose model. By making simplifying assumptions, the Rose model can estimate values for the repaired stress intensity factor, K_R, the maximum adhesive shear strain, γ_A^{max}, the maximum tensile stress in the patch reinforcement, σ_R^{max}, and the change in stiffness due to the addition of the crack and bonded reinforcement. The Rose model can also be expanded to include residual thermal stresses generated during adhesive curing and out-of-plane bending due to one-sided reinforcement. A summary of the Rose model, in determining K_R, γ_A^{max}, and σ_R^{max}, will be presented here. A more detailed discussion can be found in References 33, 34, and 35.

The analysis is divided into two stages, each with its own simplifying assumptions. The first stage, stage I, involves a bonded reinforcement on an uncracked plate as shown in Figure 7 with the sole purpose of determining the normal stress distribution, σ_0, in the plate within the domain of the bonded reinforcement. The major assumption here is that the adhesive forms a rigid-bond such that there is no relative displacement between the reinforcement and the plate. This assumption is reasonable because the load transfer zone
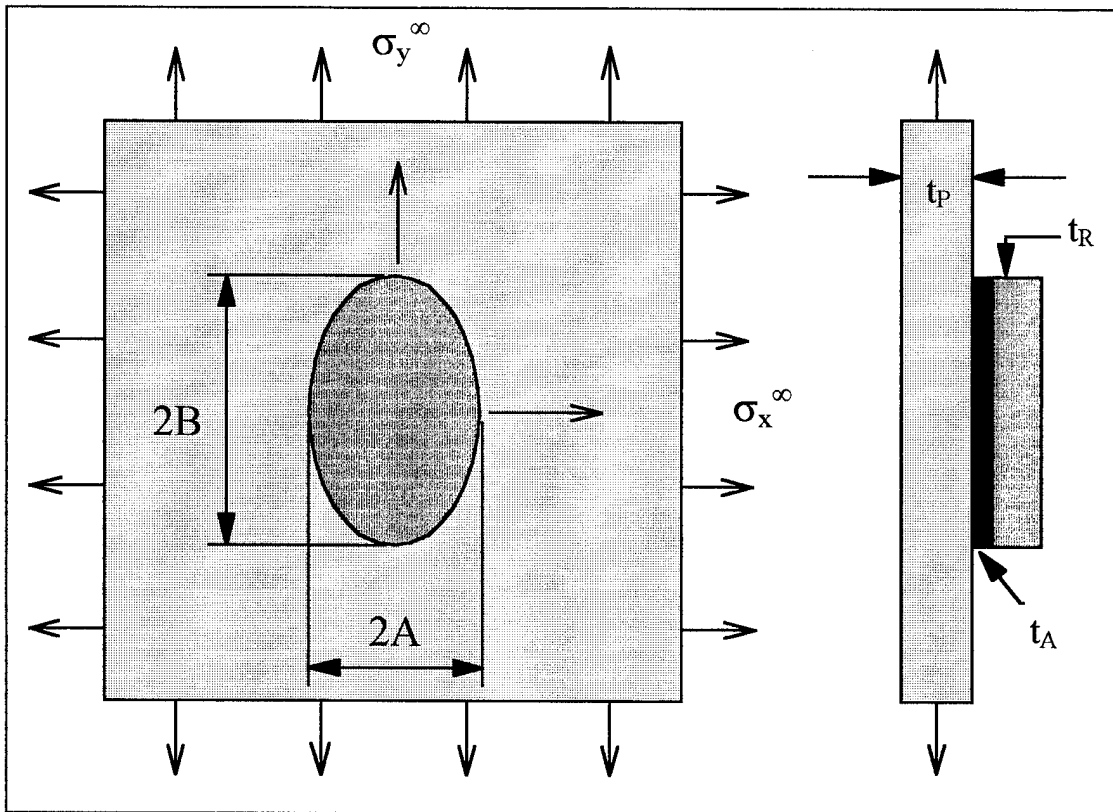
Figure 7. Bonded Reinforcement on Uncracked Plate (15:114)

around the edges of the reinforcement, i.e. the area of high load and relative displacement, is small compared to the overall reinforcement dimensions. Stage II introduces a crack in the plate allowing the stress σ_0 to relax to zero at the crack faces. The major assumption is that the reinforcement can now be assumed to be of infinite size with the end result being the repaired stress intensity factor, K_R.

From one-dimensional theory of bonded joints, the load transfer length, $1/\beta$, in terms of the system material and physical properties is

$$\frac{1}{\beta} = \left[\frac{t_A}{G_A} \left(\frac{E_P t_P E_R t_R}{E_P t_P + E_R t_R} \right) \right]^{1/2} \tag{1}$$

where t_A is the adhesive thickness, t_P is the plate thickness, t_R is the reinforcement

thickness, E_P is the plate elastic modulus in the longitudinal direction, E_R is the

reinforcement elastic modulus in the longitudinal direction, and G_A is the adhesive shear

modulus. Within the load transfer zone, the stiffness of the system is represented by a step

jump in stiffness from $E_P t_P$ to $E_P t_P + E_R t_R$.

Stage I. Reduction in the stress intensity factor is achieved in two ways. The first

reduction results from load sharing by the reinforcement which is important in stage I of

the analysis. The second reduction is due to crack bridging by the reinforcement and

appears in stage II.

In stage I, also called the inclusion analogy, the plate and reinforcement are viewed

together as an equivalent inclusion of higher stiffness than the surrounding plate as shown

in Figure 8. This equivalent inclusion is possible because the load transfer length, $1/\beta$, is

small compared to the dimensions A and B of the reinforcement. To determine the normal

stress distribution, σ_0, in the reinforced plate, the analysis involves the calculation of: (1)

the elastic constants of the equivalent inclusion in terms of the reinforcement and the plate;

(2) the stress in the equivalent inclusion; and (3) the load sharing between the

reinforcement and the plate. Calculating the stress in the equivalent inclusion can only be

accomplished for certain simple shapes, which is why Rose modeled an elliptical

reinforcement. Within an elliptical inclusion, the stress is uniform as shown in Figure 9.

To further simplify the analysis, Rose also uses the overall assumption that both the
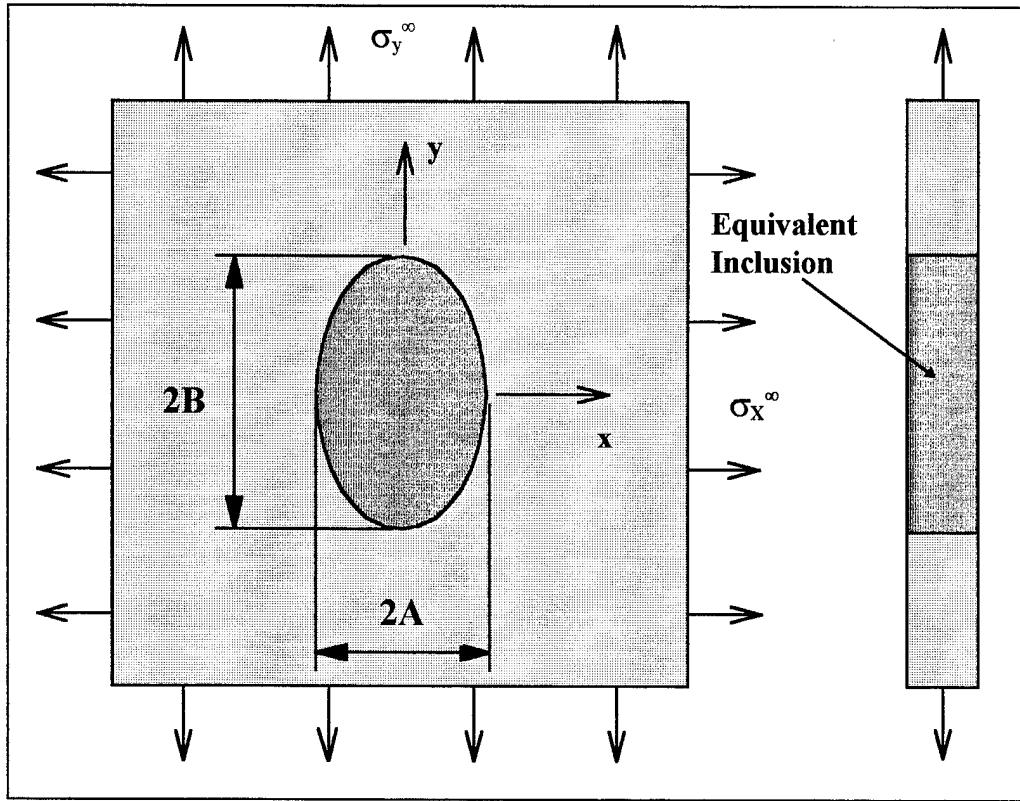
Figure 8. Equivalent Inclusion (15:115)

reinforcement and the plate are isotropic with the same Poisson ratio. This assumption

results in an equivalent inclusion stiffness of $E_P t_P + E_R t_R$. Orthotropic cases can be found

in literature (34). The load transmitted across $y = 0$ within the inclusion, $|x| < A$, is a

force per unit length, F, given by

$$F = \sigma_y^\infty t_P \left\{ 1 + \frac{S}{D} \left[1 + 2(1+S)\frac{B}{A}\left(1 - \upsilon\frac{\sigma_x^\infty}{\sigma_y^\infty} \right) + (1+S-\upsilon S)\left(\frac{\sigma_x^\infty}{\sigma_y^\infty} - \upsilon \right) \right] \right\} \qquad (2)$$

$$D = 3(1+S)^2 + 2(1+S)\left(\frac{B}{A} + \frac{A}{B} + \upsilon S \right) + 1 - \upsilon^2 S^2 \qquad (3)$$
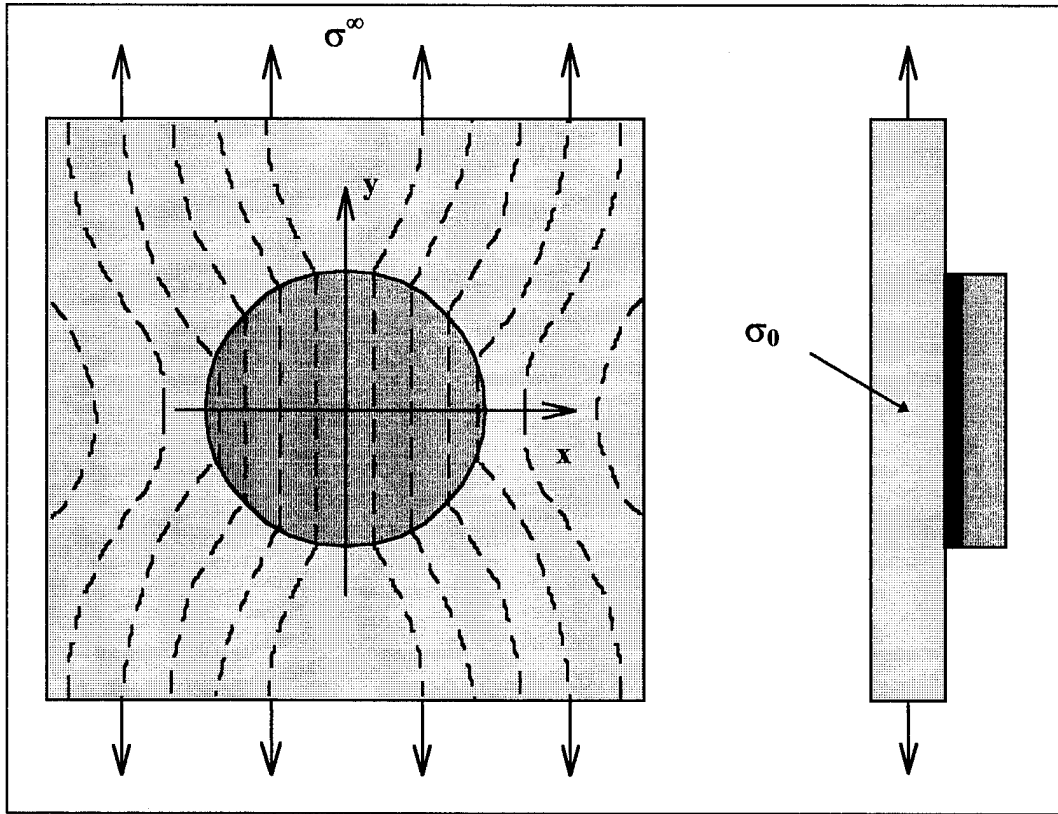
Figure 9. Uniform Load in Elliptically Reinforced Region of Plate (15:116)

$$S = \frac{E_R t_R}{E_P t_P} \tag{4}$$

This load is shared by the plate and the reinforcement with the normal stress in the plate, σ_0, given by

$$\sigma_0 = \sigma_y^P \left(|x| \langle A, y = 0 \right) = \frac{F}{t_P (1 + S)} \tag{5}$$

If desired, the inclusion analogy also provides the plate stress just outside of the reinforcement. A stress of special interest is that just outside of the patch at x = 0, y = B+ given by

$$\sigma_y^p(0,B+) = \frac{F}{t_P} = (1+S)\sigma_0 \qquad (6)$$

because this is an area of high loading in which cracking can initiate.

Stage II. Now that the stress at the crack, σ_0, is known, the plate is cracked along $|x| < a$, $y = 0$ as shown in Figure 10. As previously stated, the reinforcement is assumed
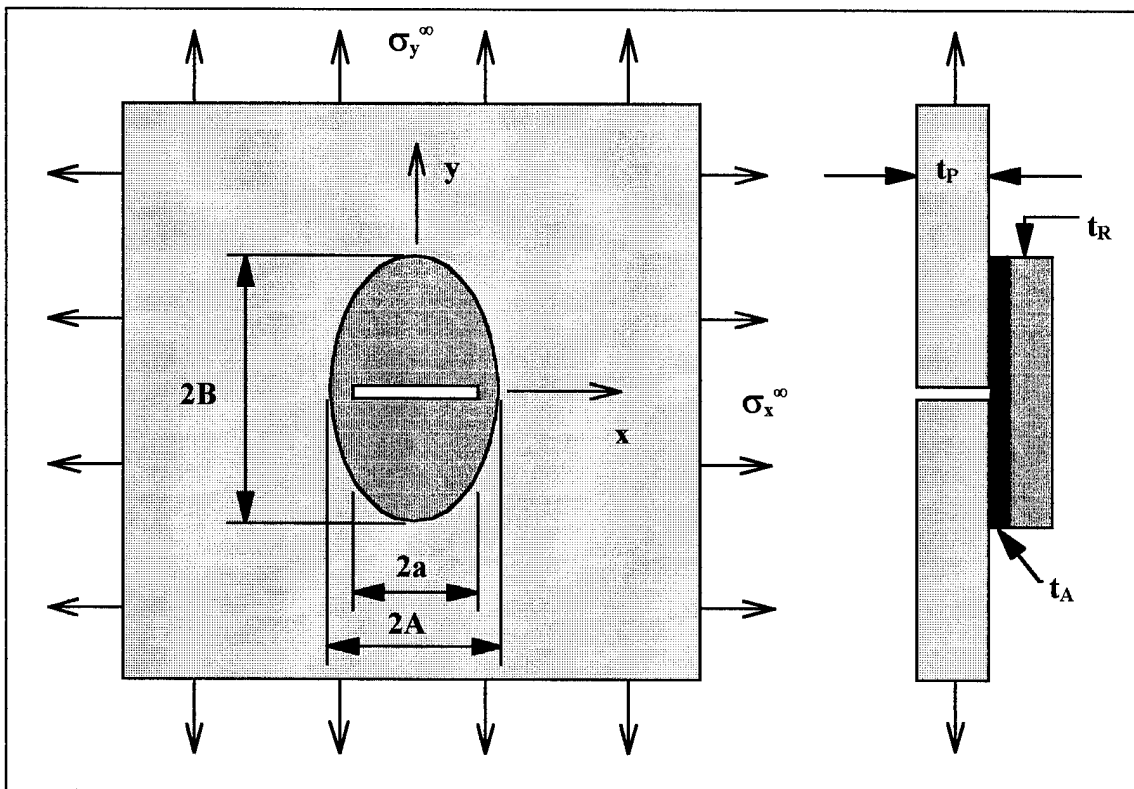
Figure 10. Crack Introduced into Plate (15:115)

to be of infinite size because the load transfer zone at the crack is small. This allows the system to be analyzed as the simple overlap joint shown in Figure 11. The overlap joint is

31
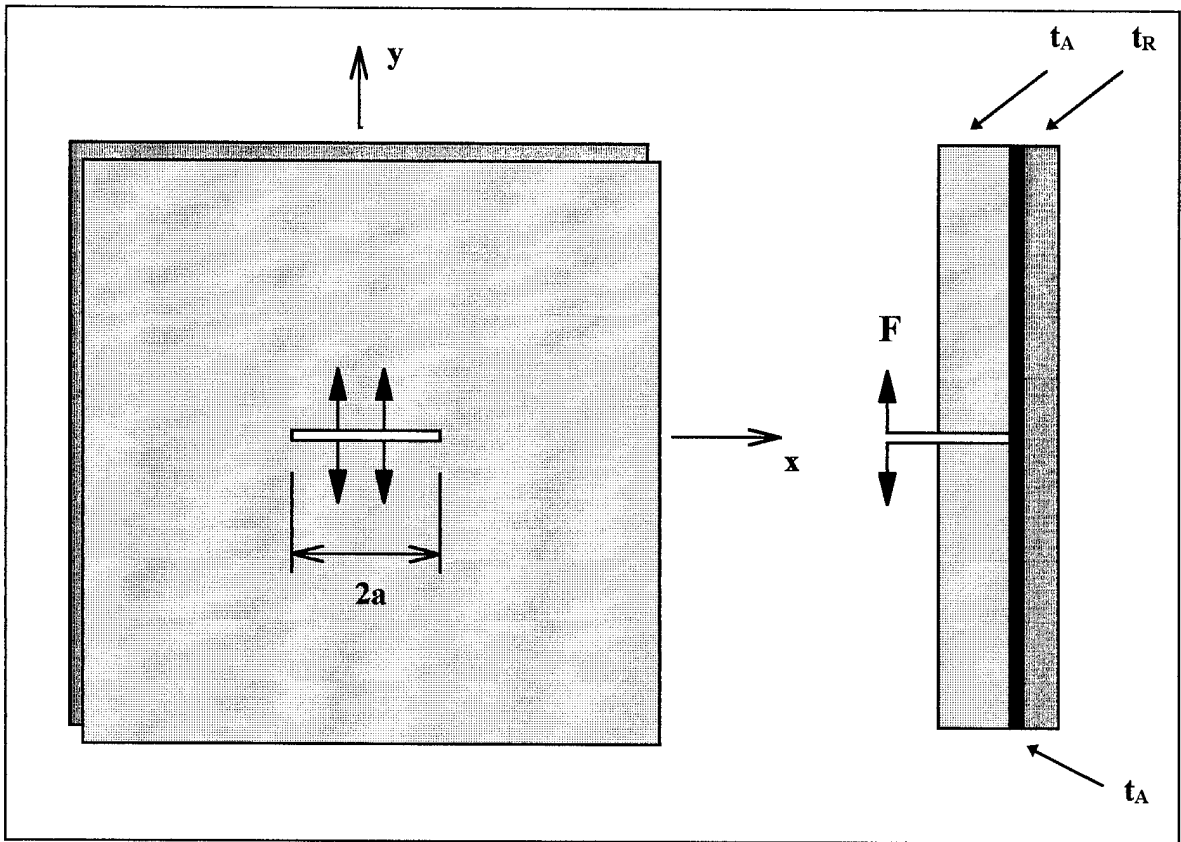
Figure 11. Overlap Joint (35:86)

much easier to analyze as compared to the original configuration in Figure 10. The stress

intensity factor for a nominal center cracked plate is commonly known to be

$$K_0 = \sigma_0 [\pi a]^{\frac{1}{2}} \tag{7}$$

which behaves as an upper bound for the repaired stress intensity factor, K_R. However, in

comparison to an unbounded K_0 with crack length for a nominal center cracked plate, K_R

does not exceed a limiting value of K_∞ as shown in Figure 12. Rose shows that $K_\infty = K_0$ at

a characteristic crack length, Λ, given by
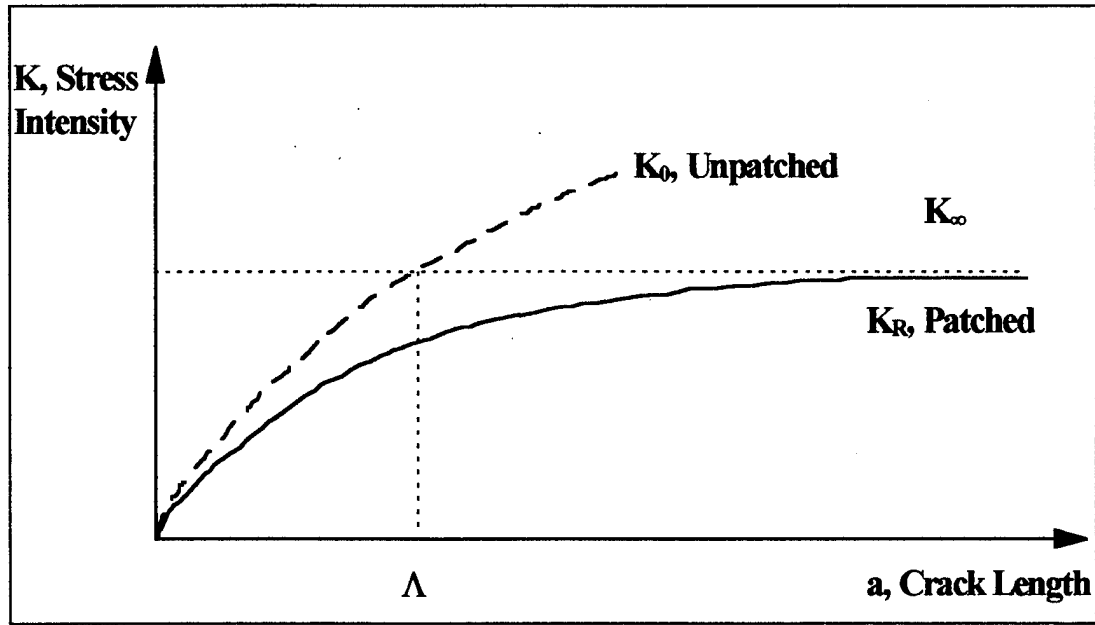
Figure 12. Variation of K_R with Crack Length with the Two Asymptotes, K_∞ and K_0. (32:86)

$$\Lambda = \frac{1}{\pi}\left[E_P t_P\left(\frac{t_A}{G_A}\right)\beta\right] = \frac{1}{\pi}\left(1+\frac{1}{S}\right)\beta^{-1} \qquad (8)$$

where $1/\beta$ is the load transfer length. K_∞ is, therefore, given by

$$K_\infty = \sigma_0[\pi\Lambda]^{\frac{1}{2}} \qquad (9)$$

and also behaves as an upper bound for K_R. K_0 and K_∞ are the first terms in the

asymptotic expansions of K_R in the limits $a/\Lambda \ll 1$ and $a/\Lambda \gg 1$. Interpolating between

these asymptotes leads to an analytical estimation for K_R given by

$$K_R = \sigma_0\left[\frac{\pi a\Lambda}{a+\Lambda}\right]^{\frac{1}{2}} \qquad (10)$$

33

Within $a/\Lambda<1$, the reduction in the stress intensity factor is primarily due to reducing the plate stress from σ^∞ to σ_0 in stage I of the analysis. For $a/\Lambda>1$, bridging of the crack also contributes to the reduction of the stress intensity factor, physically explaining Λ and the upper bound of K_∞ on K_R.

Maximum Reinforcement Stress and Adhesive Shear Strain. The maximum reinforcement stress occurs at $y = 0$. A conservative upper bound for this maximum stress is

$$\sigma_R^{\max} = \frac{F}{t_R} \tag{11}$$

where F and t_R are the same as previously defined.

Maximum adhesive shear strain also occurs at $y = 0$, the crack faces, provided the reinforcement is tapered around its edges to reduce peel. Again, a conservative estimate, assuming the adhesive remains elastic is

$$\gamma_A^{\max} = \frac{\sigma_0 t_P \beta}{G_A} \tag{12}$$

for $\sigma_0 t_P\beta < \tau_{yield_A}$. If plastic deformation occurs, $\sigma_0 t_P\beta > \tau_{yield_A}$, the maximum adhesive shear strain is

$$\gamma_A^{\max} = \frac{0.5\tau_{yield_A}}{G_A}\left[1+\left(\frac{\sigma_0 t_P \beta}{\tau_{yield_A}}\right)^2\right] \tag{13}$$

where the characteristic length in previous equations becomes

$$\Lambda = \frac{1}{3\pi}\left\{E_P t_P\left(\frac{t_A}{G_A}\right)\beta\left(\frac{\sigma_0 t_P \beta}{\tau_{yield_A}}\right)^2\left[1+2\left(\frac{\sigma_0 t_P \beta}{\tau_{yield_A}}\right)^3\right]\right\}. \tag{14}$$

34

III. Experimental Set-up and Procedure

The purpose of this chapter is to present a detailed description of the materials used, specimen design, and specimen fabrication. Also included in this chapter is the experimental set-up and procedure, as well as the details of the equipment used to analyze the specimens during fabrication and testing.

Materials

The materials investigated in this study included a unidirectional three-ply boron/epoxy composite , a clad 2024-T3 aluminum panel, AF-163-2 film adhesive and EA-9394 paste adhesive. The boron/epoxy was supplied in prepreg tape form by Warner Robbins Air Logistics Center and manufactured by Textron Specialty Materials Incorporated. The AF-163-2 film adhesive was supplied by the USAF Flight Dynamics Directorate and manufactured by 3M. The EA-9394 paste adhesive was supplied by the USAF Materials Directorate and manufactured by Hysol. The 2024-T3 aluminum was supplied by Dayton Copper and Brass Incorporated. Material properties for these materials are presented in Table 4, where the subscripts L and T stand for longitudinal and transverse values.

Specimen Design and Fabrication

The specimens used in this study were designed and fabricated to simulate an on

Table 4. Patch System Material Properties (23, 40)

Material	2024-T3	Boron/Epoxy	AF-163-2 Adhesive	EA-9394 Adhesive
E_L / E_T (GPa)	72.4 / 72.4	210 / 25	NA	NA
σ_{ultL} / σ_{ultT} (MPa)	448 / 448	1590 / 83	NA	NA
α_L / α_T (10^{-6}/°C)	22.7 / 22.7	4.5 / 20	NA	NA
G (MPa)	NA	NA	405.8	1461
γ_{yield} (%)	NA	NA	≈ 9	1.66
υ_L	0.33	0.168	NA	NA

aircraft repair of a fuselage. Five steps were involved in their preparation and include: (1) fabrication and precracking of the 2024-T3 aluminum panels; (2) patch lay-up and curing ; (3) adherend surface preparation; (4) patch application and curing; and (5) bond/disbond quality inspection and verification.

The 2024-T3 aluminum panels with nominal dimensions of 508x152x1 mm (20x6x0.04 in) were cut from much larger 1 mm (0.04 in) thick sheets of 1.8x1.2 m. Bolt holes at the ends of the panels were then punched out for grip attachment. Finally, a 15 mm (0.6 in) long Electronic Discharge Machining (EDM) cut was made in the center of each specimen, i.e. 254 mm (10 in) from each end. Two specimens had smaller 7.5 mm (0.3 in) EDM cuts. Precracking was accomplished at a frequency of 5 Hz and load levels of 100 MPa (14.50 ksi) and 90 MPa (13.05 ksi) depending on the load levels to be tested later. The fatigue cracks were grown to approximately 12.7 mm (0.5 in) and 25.4 mm (1.0 in) with the majority of specimens having approximately 25.4 mm fatigue cracks. These details are given in Table 5.

Table 5. Specimen Precracking Loads and Crack Lengths

Specimen Number	Precracking Load (MPa)	Final Crack Length After Precracking (mm/inches)
1	100	26.032 / 1.0248752
2	100	25.794 / 1.0155
3	100	25.988 / 1.023175
4	100	25.632 / 1.00915
5	100	26.176 / 1.03055
6	100	25.791 / 1.0154
7	100	25.4 / 1.00
8	100	26.597 / 1.0471
9	100	26.306 / 1.03565
10	90	25.71 / 1.0122
11	100	25.439 / 1.00155
12	100	25.799 / 1.0157
13	100	25.457 / 1.00225
14	100	25.588 / 1.0074
15	90	25.908 / 1.02
16	100	25.723 / 1.0127
17	100	25.69 / 1.01145
18	90	25.4 / 1.00
19	90	25.535 / 1.00535
20	100	27.238 / 1.07235
21	90	26.355 / 1.0376
22	100	25.208 / 0.99245
23	100	12.865 / 0.5065
24	100	12.659 / 0.4984
25	90	25.633 / 1.00915
26	100	25.277 / 0.99515
27	100	12.868 / 0.50660
28	90	12.871 / 0.506725

Patch lay-up required the fabrication of templates out of aluminum for each individual ply. The templates were cut to the exact dimensions of the three plies of the patch. A teflon backing was applied to one side of each template to keep the template

from sticking to the tacky prepreg tape as the individual plies were cut to size.

Additionally, each individual template was kept chilled before its use which also aided in

eliminating sticking to the prepreg tape. All three plies were layed-up unidirectionally, i.e.

the fibers were in the direction of load, with the following order from top to bottom,

medium, small and large as shown in Figure 13. The larger cover-ply is common practice
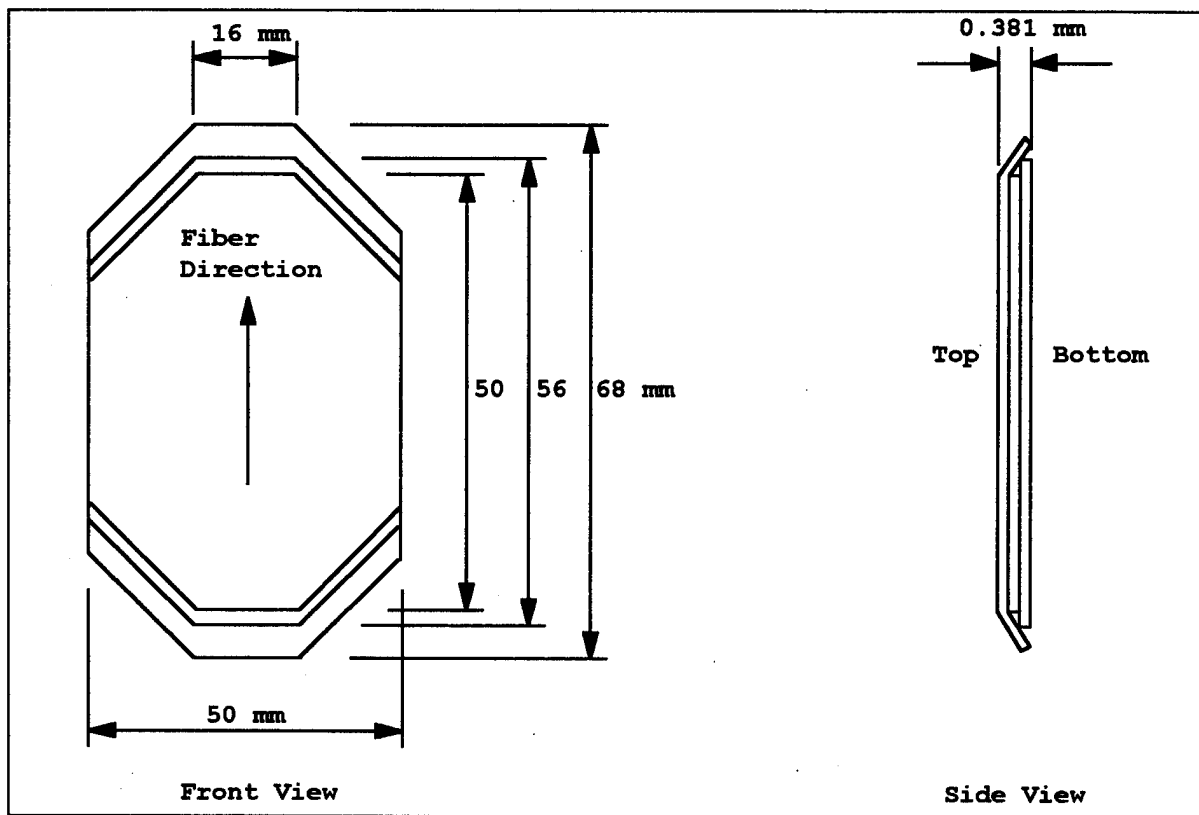
Figure 13. Patch/Reinforcement Lay-up

in composite patch repair, protecting the underlying plies from damage as well as shielding

the bondline from environmental attack. Tapering of the plies reduces out of plane loads

that cause peel and cleavage loading on the adhesive bond as shown in Figure 4. As a rule of thumb, the repair overlap length, one half the length of the repair, is 30 times the repair patch thickness for double-lap joints and 80 to 100 times the thickness for single-lap joints (22). The extra overlap length for single-lap joints reduces secondary bending moments which in turn reduces peel and cleavage loads. The overlap length of the single-lap repair in this study was approximately 89 times, 34 mm (1.3 in), the repair thickness of 0.381 mm (0.015 in). The repair stiffness ratio, $E_R t_R / E_P t_P$, was 1.125, more than the minimum required stiffness ratio of 1 (15). The patches were then pre-cured at the University of Dayton using an autoclave to enhance storability of the patches and to reduce coefficient of thermal expansion mismatch effects during bonding to the aluminum panels. A full vacuum and a 344,738 Pa (50 psi) positive pressure was applied to the patches during a 1.4-2.4 °C/minute (3-5 °F/minute) temperature ramp-up to 121 °C (250 °F). Once the temperature reached 121 °C, the 344,738 Pa pressure was released while maintaining a full vacuum for one hour. After one hour, the temperature was then dropped at 1.4-2.4 °C/minute, completing the cure process.

Aluminum pre-bond surface preparation was accomplished using a common field/base level technique to simulate actual field operations as close as possible. Preparation was conducted on a 127x102 mm (5x4 in) area over the crack, allowing adequate bonding area for the patch. Steps involved include: (1) solvent degreasing; (2) mechanical abrasion of adherends; (3) silane agent preparation; (4) wetstanding procedure; and (5) primer application and cure. Methyl Ethyl Ketone (MEK) was used to degrease

the aluminum panels. MEK was repeatedly applied and wiped-off with a lint-free paper towel until no more residue was noticed on the towel. An MEK wipe was also accomplished on the pre-cured boron/epoxy patch. Grit blasting using non-recycled 50 micron aluminum oxide grit mechanically abraded and cleaned the aluminum until the surface obtained a uniform dull, white, metal appearance. Excess aluminum oxide on the surface was blown-off using a gaseous nitrogen jet. Grit blasting of the thin pre-cured boron/epoxy patch was not done due to the fragile nature of the patch around its edges. Silane agent preparation involved a one-hour hydralization/mixing process of a 1 ml silane coupling agent, Dow Corning Z640, with a 99 ml distilled water solution. This one percent silane solution was enough for four panels during the wetstanding procedure. The solution was evenly applied to the bond area with a clean brush for 10 minutes to insure no surface contamination and complete wetability of the bond area. The surface was then dried using a gaseous nitrogen jet. If complete wetability of the bond surface was not achieved the grit blasting and wetstanding processes were repeated. The silane treated panels were then dried in an oven at 93 °C (200 °F) for one hour. Finally, a degreasing primer, American Cyanamid BR127, was applied and cured for 30 minutes at room temperature and then for one hour at 121 °C (250 °F) to protect the clean aluminum surface from contaminants.

Before the cured patches were applied to the aluminum panels, AF-163-2 film adhesive was applied to the back of the patches and cut to size. Teflon tape of 0.1 mm (0.004 in) thickness was used to simulate disbonding in the bondline of the repair and was

cut to exact dimensions and carefully placed on the bond surface in the locations desired. The patch was then applied to the bond surface. The repair was cured under 65,500 Pa (20 inches Hg, 9.5 psi) vacuum pressure at 121 °C for one hour. The one hour cure was proceeded by a 1.4-2.4 °C/minute ramp-up in temperature and followed by a 1.4-2.4 °C/minute ramp-down in temperature. Curing was accomplished using an electric driven pump and a ZIPVAC vacuum bag to supply the required pressure and the heated platen of a hydraulic press to supply the heat.

Two patches employed the EA-9394 paste adhesive instead of the AF-163-2 film adhesive. EA-9394 is a two-part paste adhesive consisting of a liquid epoxy resin and a cross-linking agent. Following mixing of the two components, the adhesive was spread onto the patch as evenly as possible using a clean razor blade. A light scrim cloth was then applied over the paste to act as a carrier cloth for the adhesive system. Another thin layer of adhesive was applied over the scrim cloth. Finally, the adhesive was spread onto the specimen before application of the patch over the cracked surface. Paste adhesives have the advantage of room or temperature cure, however, the two specimens that employed this adhesive received a 93 °C (200 °F) cure for one hour, with the same ramp-up and ramp-down in temperature as the AF-163-2 film adhesive. All equipment and procedures matched that of the AF-163-2 film adhesive specimens. The vacuum bag is shown in Figure 14 and the hydraulic press in shown in Figure 15.

Following cure, bondline inspection was made possible using an ultrasonic tank. The ultrasonic equipment provided a C-SCAN printout, allowing verification of bondline
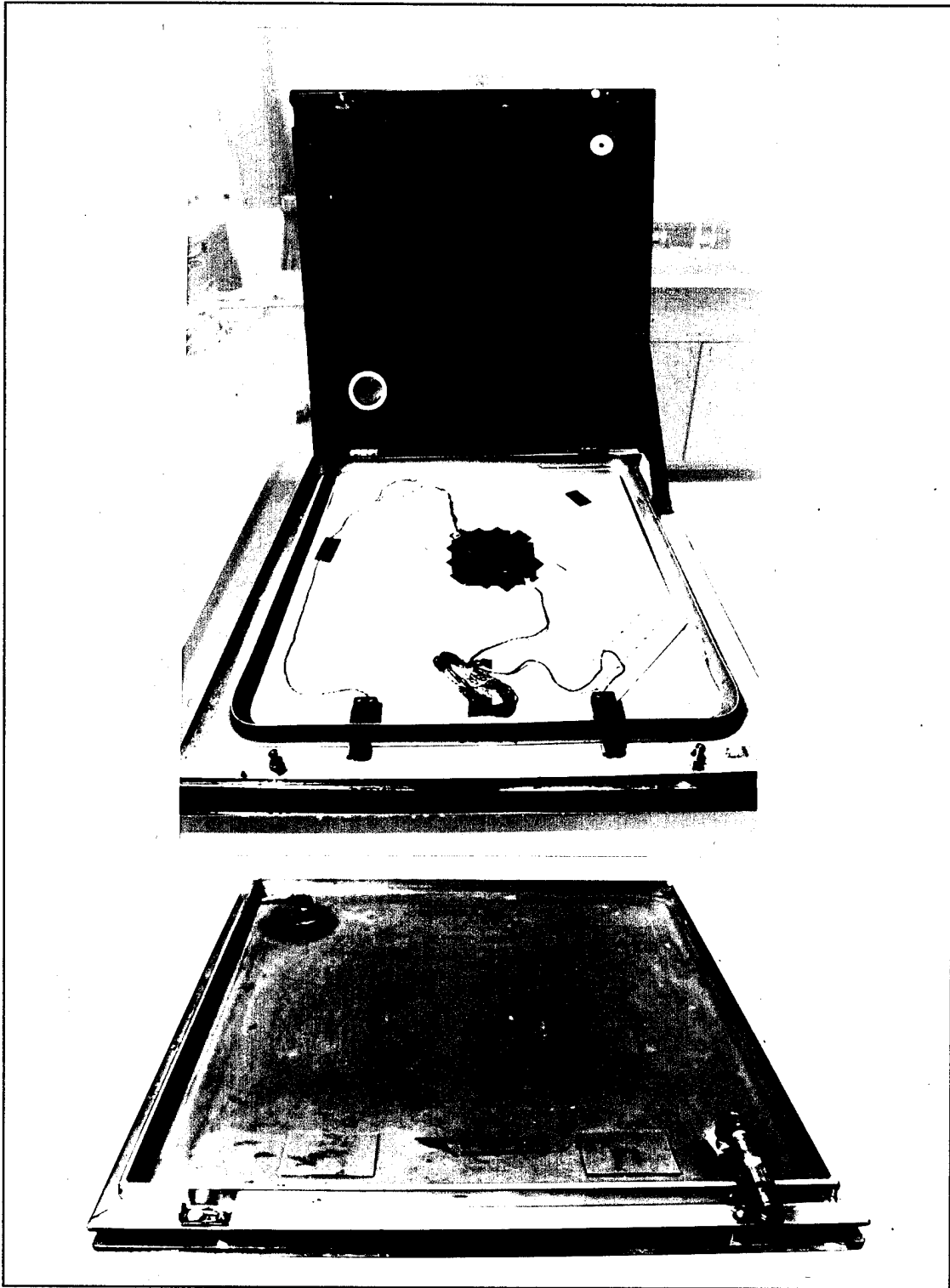
Figure 14. Vacuum Bag

42
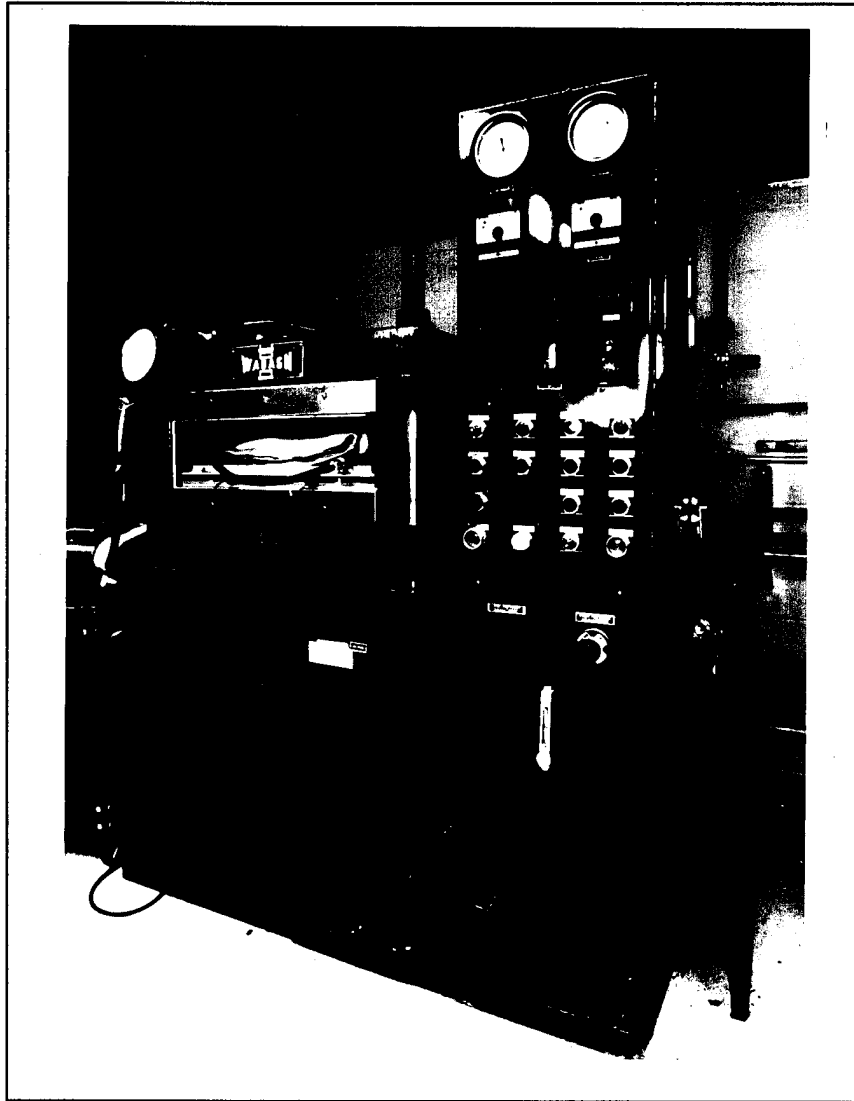
Figure 15. Hydraulic Press

integrity, as well as, disbond size and location. A schematic of the ultrasonic equipment is

shown in Figure 16. A sending transducer sends a high-frequency pulse through the test

object (patch and aluminum panel). When a disbond is encountered, the transmission of

the high-frequency pulse is interrupted. These pulses, as well as, the through the test
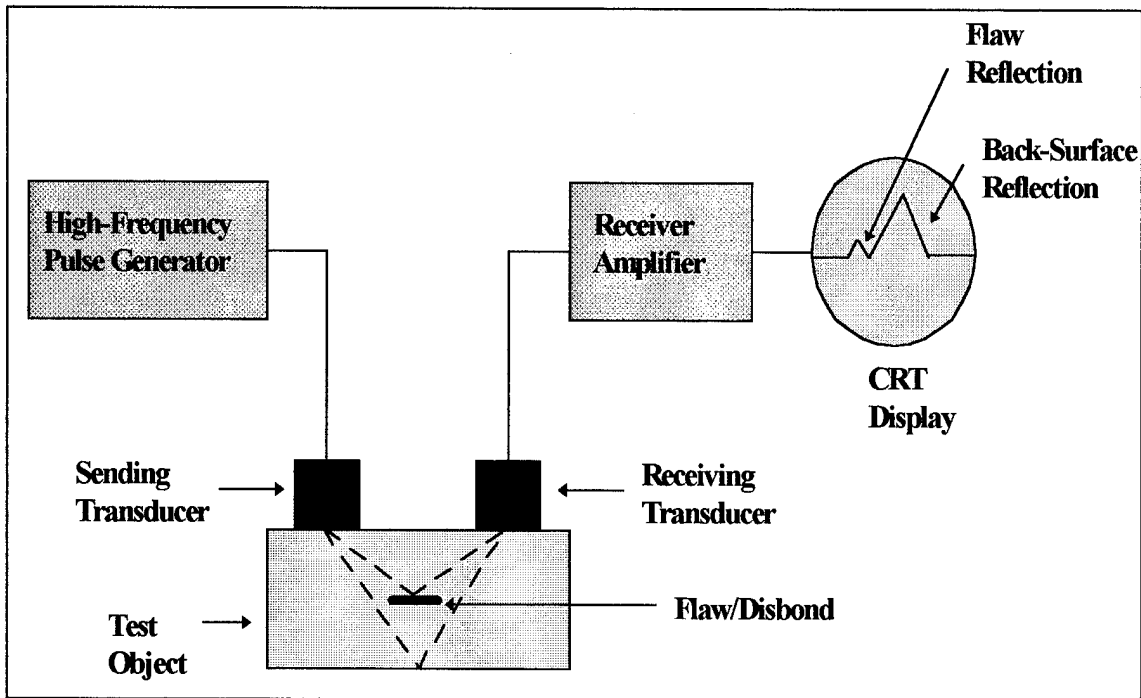
Figure 16. Schematic of Ultrasonic Equipment

object pulses are received by another transducer which feeds the information to an amplifier and CRT display. The result is a two-dimensional contour map of the bondline indicating disbond sizes and shapes. The ultrasonic tank is shown in Figure 17. The specimen configuration is shown in Figures 18.

Test Apparatus

All tests were performed on a servo-hydraulic test stand (Material Test System 810) equipped with a 9,979 kg (22,000 lb) load cell and a DC electric potential difference (EPD) system for measuring crack length. The fatigue test profile was supplied to the test stand from a Zenith 486 computer via a program called LABVIEW. The program
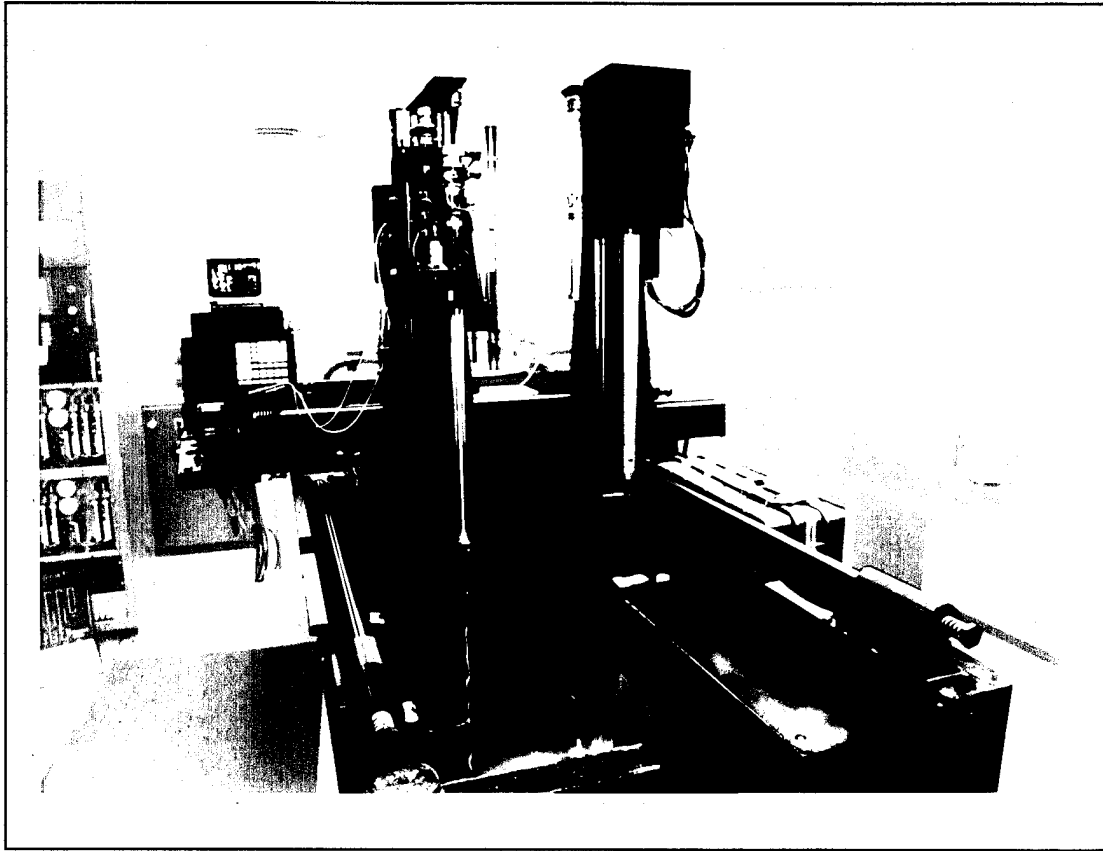
Figure 17. Ultrasonic Tank

prompts the user for the maximum stress level, the stress ratio, R, the load frequency, the

starting cycle count, the initial crack size, the specimen geometry, the data acquisition

interval (DAC) and the input current for the EPD system. When the program is initiated,

it sends commands to the MTS 458.91 micro-profiler which in turn directs the load cell to

fatigue the specimen with a sinusoidal wave at the frequency and levels desired. Data

taken at each acquisition interval included the cycle count, maximum and minimum stress

level as well as the total crack length as measured by the EPD system. Crack length was
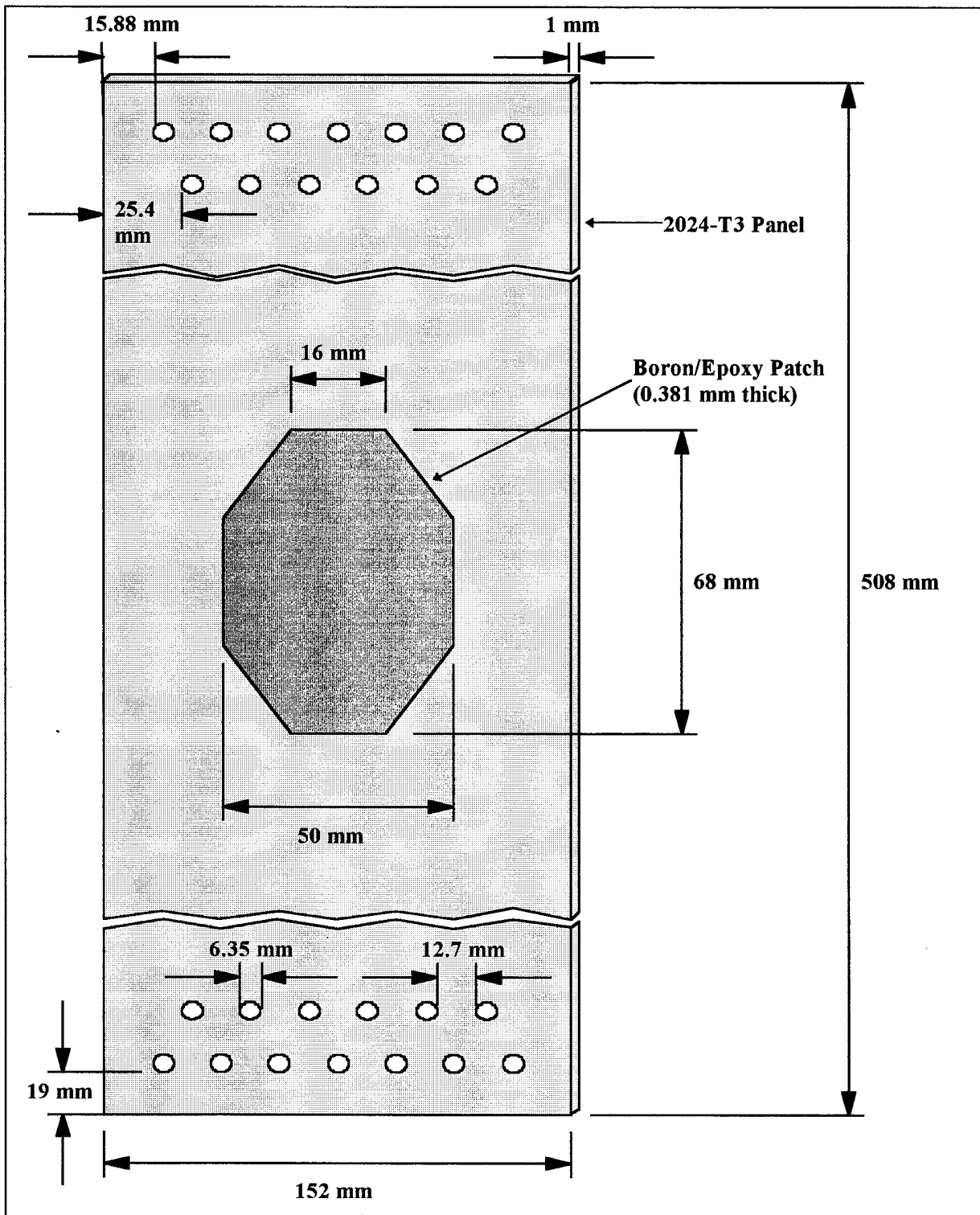
Figure 18. Specimen Configuration

also measured optically using a traveling microscope (Gaertner Scientific Corporation Model #721C.001).

EPD measurements rely on the principle that the electric field in the cracked specimen with current flowing through it is a function of specimen geometry, especially crack length. For constant current flow, the voltage drop across the crack face will increase with increasing crack size as a result of modification of the current by pertubating the current flow lines. This change in voltage is then analytically related to crack size. The DC EPD circuit, shown in Figure 19, results in a two-dimensional electric field throughout the thickness of the specimen. The voltage measurement leads at a distance of $2Y_0$ apart measure the voltage change during crack growth. Changes in voltage are a consequence of testing in an oxidizing environment. As the crack grows an oxide layer forms immediately upon the newly created crack face insulating the two specimen halves. The closed form solution used in this study to relate voltage drop to crack size for a center cracked specimen is

$$a = \frac{W}{\pi} Cos^{-1} \left\{ Cosh \left[\frac{\pi Y_0}{W} \right] \middle/ Cosh \left[\frac{V}{V_r} Cosh^{-1} \left(Cosh \left(\frac{\pi Y_0}{W} \right) \middle/ Cos \left(\frac{\pi a_r}{W} \right) \right) \right] \right\} \quad (15)$$

for $0 \leq 2a/W \leq 1$,

where a is the crack size, a_r is the reference crack size, W is the specimen width, V is the measured EPD voltage, V_r is voltage corresponding to a_r, and Y_0 is the voltage measurement lead distance from the crack plane. Note that a_r and V_r are based on an alternate method, optical in this case, of determining a_r (5:695-698).
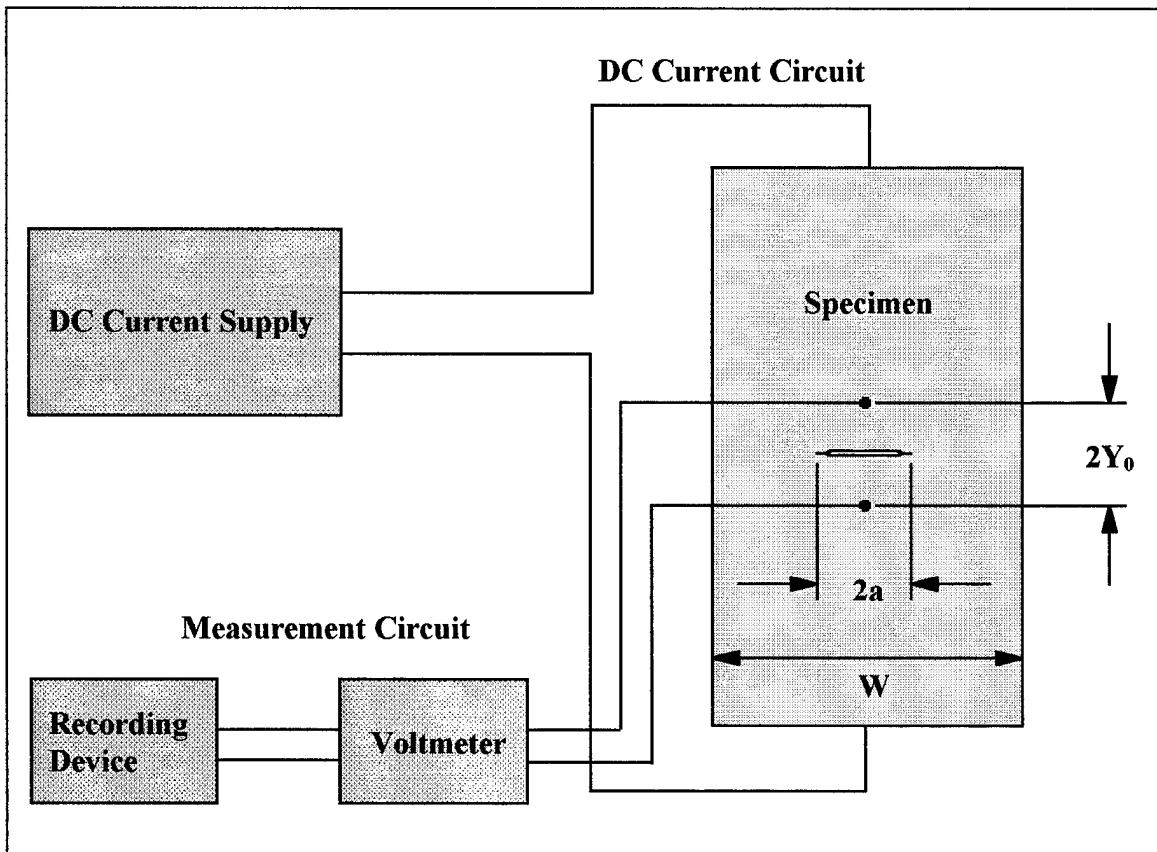
Figure 19. EPD Circuit Set-up

Disbond growth/size was qualitatively studied in real time using an Inframetrics infrared camera and controller (Model #7089). The infrared images were displayed on a monitor and recorded by a VCR to keep an ongoing log of disbond behavior for each specimen. The infrared equipment used is shown in Figure 20. Hard copy disbond data in terms of C-SCAN printouts were obtained periodically via the ultrasonic tank mentioned before. The experimental apparatus is shown in Figures 21 and 22.
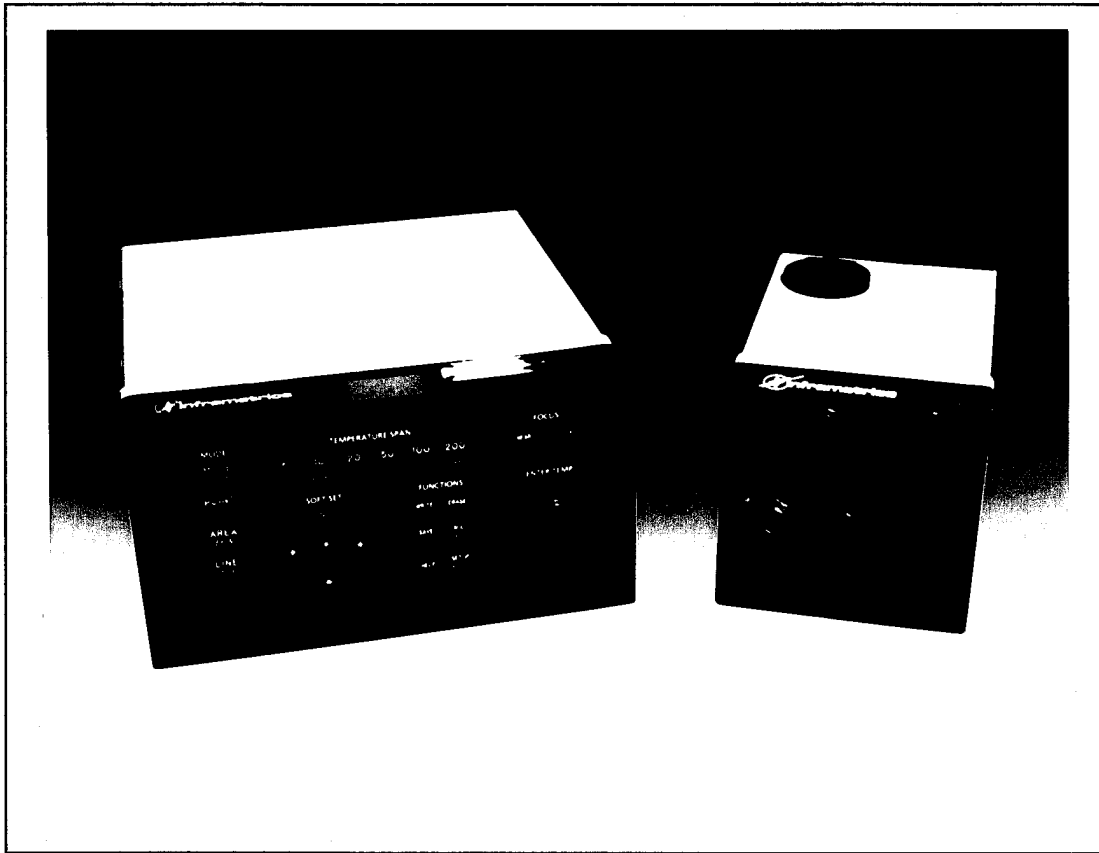
Figure 20. Infrared Camera and Controller

Experimental Procedure

After the grips were bolted to the specimen, the specimen was inserted into the test stand with the microscope facing the fatigue crack and the infrared camera facing the patch. Current leads, from the DC current source, were attached to each end of the specimen and voltmeter leads were welded one inch on either side of the fatigue crack as shown in Figures 19 and 23. Alignment of the specimen and microscope was then accomplished using a level. Required program information was then entered including a
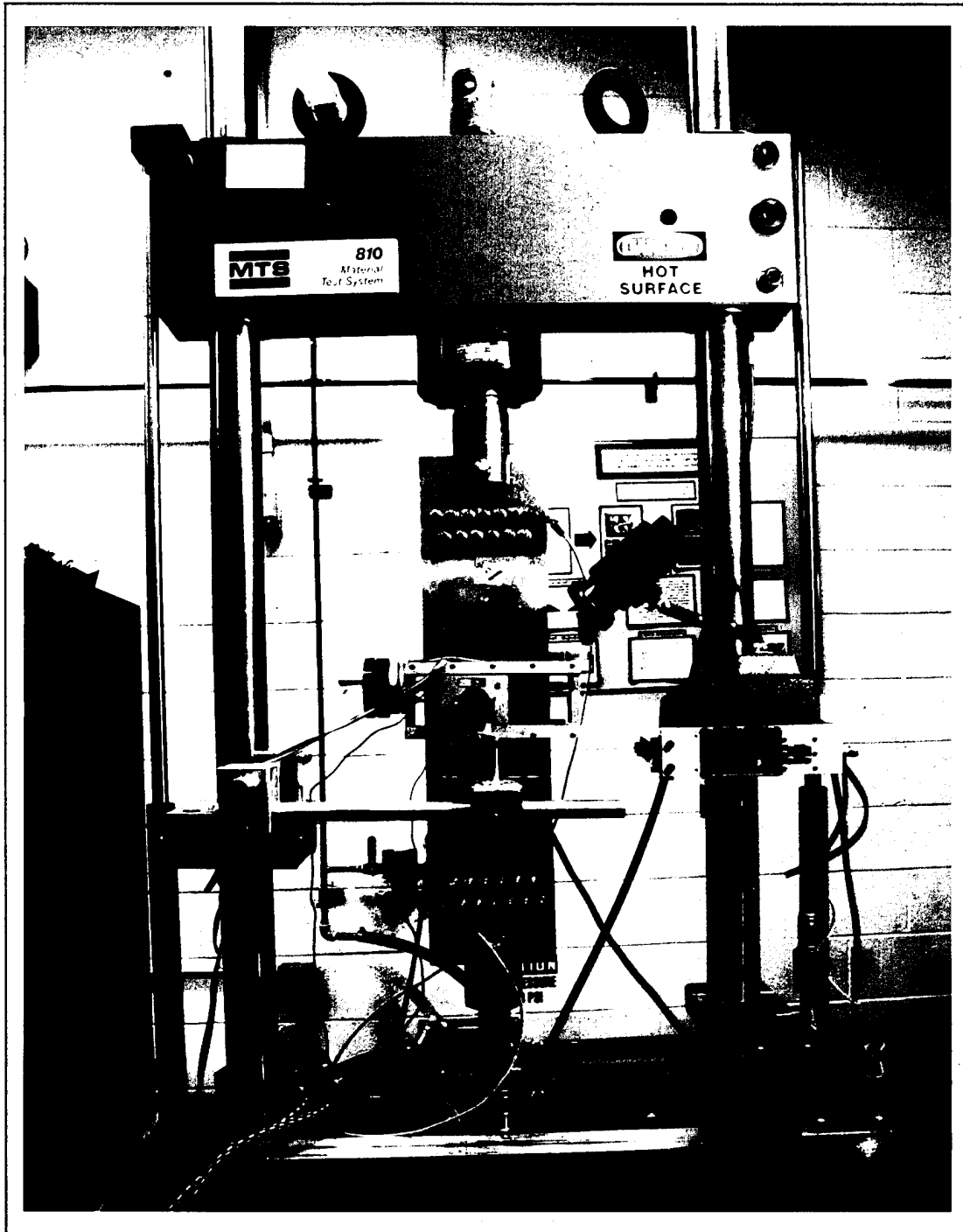
Figure 21. Experimental Apparatus

50
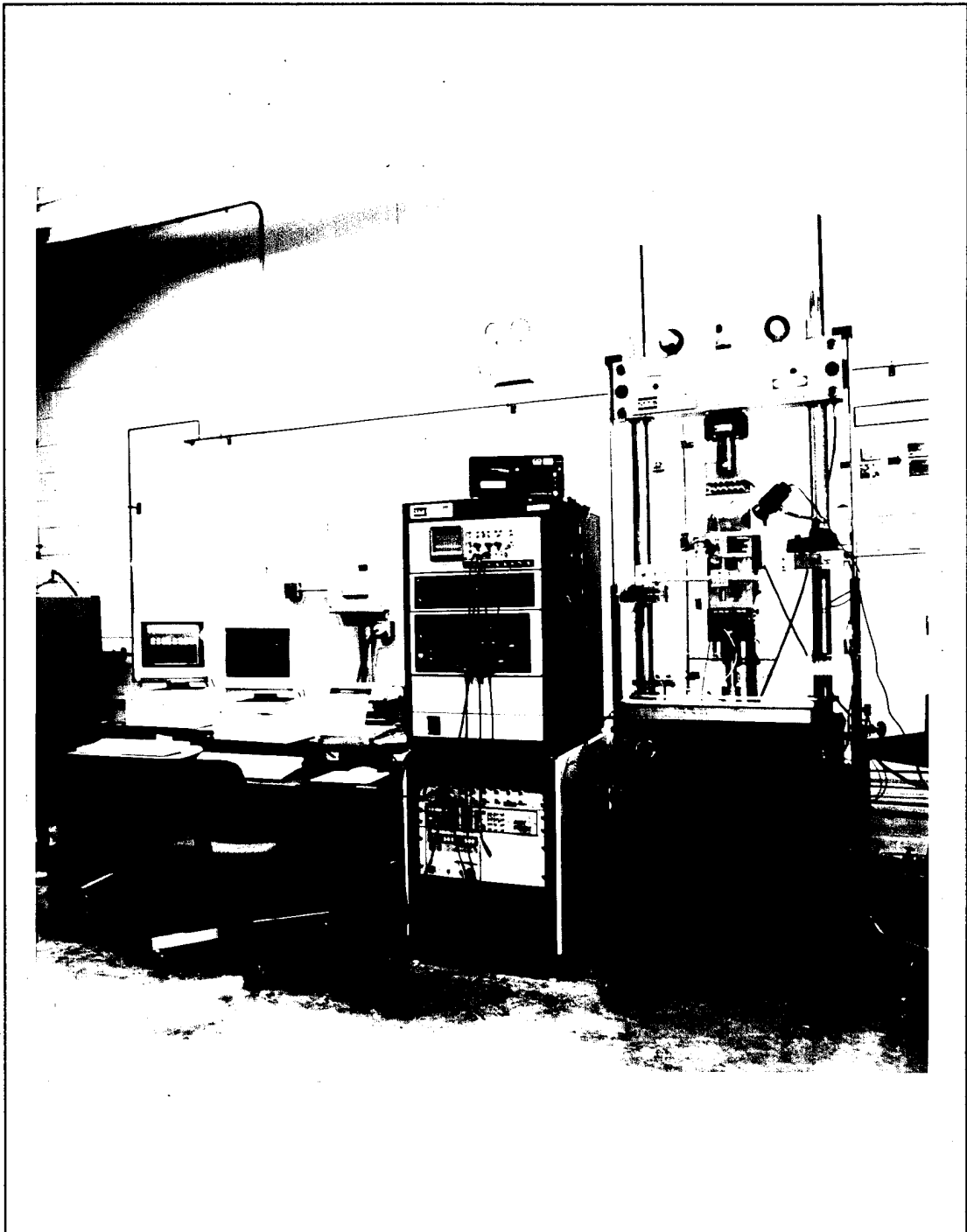
Figure 22. Experimental Apparatus

51

maximum stress level of 120 MPa or 100 MPa depending on the test, a stress ratio, R, a

load frequency of 10 Hz, the starting cycle count, the initial fatigue crack size, specimen

geometry, DAC interval and a 5.0 A current for the EPD system. Each test was stopped

frequently to take visual crack measurements. Also, the testing was stopped periodically

so that each specimen could undergo progressive ultrasonic inspections for disbond

behavior. The tests were run until each specimen failed.
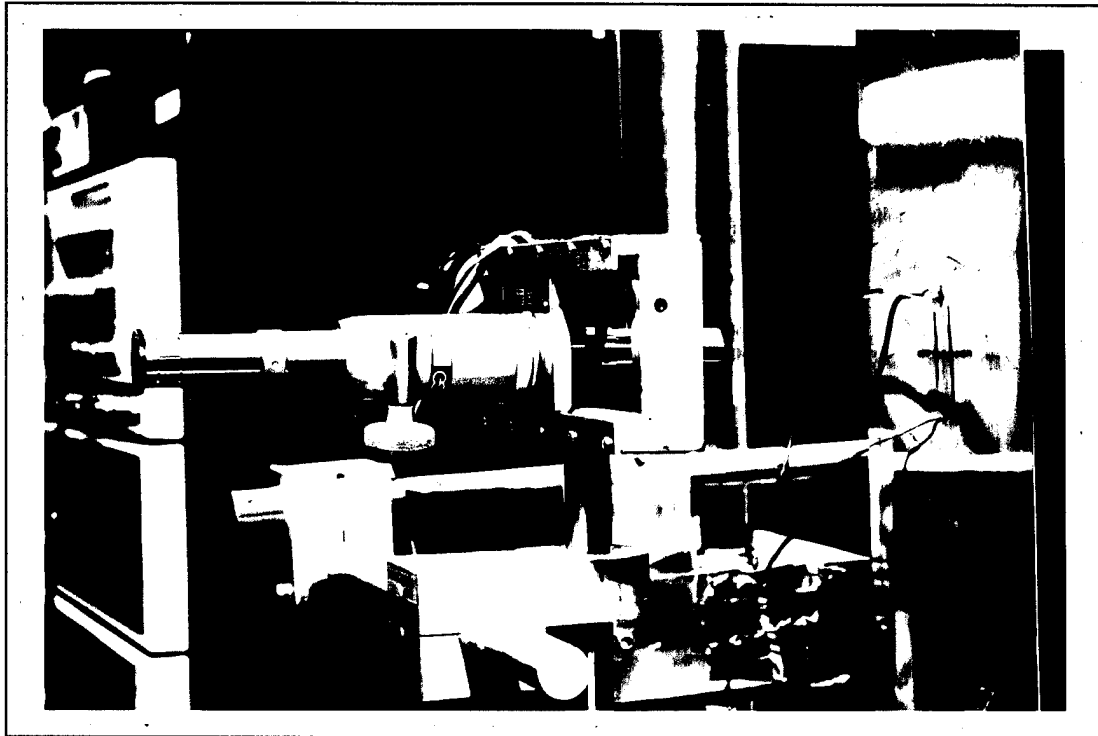
Figure 23. EPD Voltmeter Leads on Specimen

IV. Results and Discussion

The purpose of this chapter is to present the experimental results and related discussion. A total of twenty-eight tests were performed with a synopsis shown in Table 6, where a completely bonded patch (CBP), a full width disbond (FWD), crack tip disbonds (CTD), end disbonds (ED) and a center disbond (CD) are as defined in Figure 3. Two configurations of end disbonds were investigated, and are to be presented later. That is why Table 6 lists end disbonds 1 (ED1) and end disbonds 2 (ED2). Also two specimens were bonded using a high modulus adhesive (EA-9394) as compared to the rest of the specimens which were bonded with a lower modulus adhesive (AF-163-2).

The chapter is divided into five sections: (1) patching efficiency as a function of disbond location and size; (2) stress level effects; (3) stress ratio effects; (4) a comparison between high modulus and low modulus adhesives; and (5) the effectiveness of the electric potential difference (EPD) method for measuring crack growth of cracked aluminum panels repaired with bonded composite patches. Each of these sections will include a presentation of the results followed by an interpretation of the results.

For all calculations, residual thermal stress and secondary bending effects (due to a single-sided patch) are neglected. Thermal stresses are the same for each specimen, therefore, there was no difference in its effect from one case to another. Secondary bending can be neglected due to minimum neutral axis offset (since the patch was very thin; i.e. 3 plies only) and tapering of the longitudinal edges of the patch.

Table 6. Test Matrix

Specimen	Configuration**	Disbond Area (%)	Peak Load (MPa)	$R = \sigma_{min} / \sigma_{max}$
1	Baseline (No Patch)	NA	120	0.10
2*	CD	≈2.6	120	0.10
3♣	CBP	0	120	0.15
4	FWD	20	120	0.10
5	FWD	20	120	0.10
6	CTD	20	120	0.10
7	CTD	20	120	0.10
8	ED1	20	120	0.10
9	ED1	20	120	0.10
10	CBP	0	100	0.10
11	FWD	10	120	0.10
12	ED2	20	120	0.10
13	FWD	20	100	0.10
14	FWD	5	120	0.10
15	ED1	20	100	0.10
16	CD	10	120	0.10
17	CD	5	120	0.10
18	Baseline (No Patch)	NA	100	0.10
19♦	CBP	0	90, 110, 130, 140	0.10
20	CBP	0	120	0.10
21	CBP	0	120	0.10
22	ED1	20	100	0.10
23♥	CBP	0	120	0.10
24♥	CBP	0	100	0.10
25♣	CBP	0	120	0.10
26♣	CBP	0	120	0.10
27♥	Baseline (No Patch)	NA	120	0.10
28♥	Baseline (No Patch)	NA	100	1.10

* CD caused during fabrication, not intentional.

♣ R = 0.15

♦ Used for analysis to be presented in Chapter V.

♥ Initial crack length ≈ 12.7 mm (0.5 in) instead of ≈ 25.4 mm (1.0 in) in the other specimens (see Appendix B).

♣ Two-part past adhesive.

** See Figure 3

Effects of Disbond Location and Size on Patching Efficiency

This section of the chapter is divided into two major subsections, the effect of disbond location on patching efficiency and the effect of disbond size on patching efficiency. Tests conducted at 120 MPa peak load only will be presented here because the majority of disbond configurations were tested at this peak load level.

Effects of Disbond Location. Before disbond effects on patching efficiency can be presented and discussed, patching efficiency without pre-existing flaws/disbonds must be investigated. Only then can disbond location effects be logically presented. The majority of disbond configurations investigated for location effects involved disbonds approximately 20 % of the total patch area. This subsection is further divided into five parts: (1) baseline versus a completely bonded patch (CBP) effects; (2) full width disbond (FWD) effects; (3) crack tip disbond (CTD) effects; (4) end disbond (ED) effects; and (5) center disbond (CD) effects (Figure 3).

Baseline versus Completely Bonded Patch. To establish the baseline data, Specimen 1 (Table 6) with no patch and a precrack of 26 mm was tested. With a 120 MPa peak load (R = 0.10), the fatigue life of the baseline specimen was only 10,633 cycles, as shown in Table 7, verifying the severity of the conditions experienced by

Table 7. Baseline vs. CBP Fatigue Lives

Specimen Number	Configuration	Cycles to Failure
1	Baseline (No Patch)	10,633
20	CBP	118,316
21	CBP	120,325

the panels. In comparison to the baseline test, two completely bonded specimens were tested with their resulting fatigue lives also shown in Table 7. Under similar loading and damage conditions, the patched specimens exhibited significant improvement in overall fatigue life as compared to the baseline test. Specimen 20 yielded a 11.12 times life extension over the baseline test and Specimen 21 yielded a 11.32 times life extension. Specimen 21 yielded a greater fatigue life by only 2,009 cycles due to the fact that it began with a slightly smaller initial crack length (26.335 mm as compared to 27.238 mm).

Figure 24 shows the comparison between the crack length versus cycles curve for the baseline and two CBP specimens. At first glance, Figure 24 looks like a typical collection of fatigue life curves, however, it really tells the story about the mechanics and efficiency of bonded repairs. The first, and most important, feature of Figure 24 is that the crack growth rate, da/dN, was relatively constant within the domain of the patch repair. This is also shown by examining Figure 25 in which a three-point least squares method (37) was used to calculate the crack growth rate, da/dN. As shown in Figure 25, the crack growth rate was constant within the patch repair. In agreement with Rose (33) and Baker(8), the crack growth rate, and therefore, the repaired stress intensity factor range, ΔK_R, were constant inside the patch. Actually, not until the crack has extended beyond each edge of the patch does the crack growth curve change from linear to the more recognizable parabolic shape characteristic of metal fatigue. The initial stress intensity factor, K, for the baseline test was 24.26 MPa√m and the average initial repaired stress intensity factor, K_R, for the two CBP specimens was 5.43 MPa√m. K_R was calculated using the Rose model (33, 34, 35). This significant reduction in the stress intensity
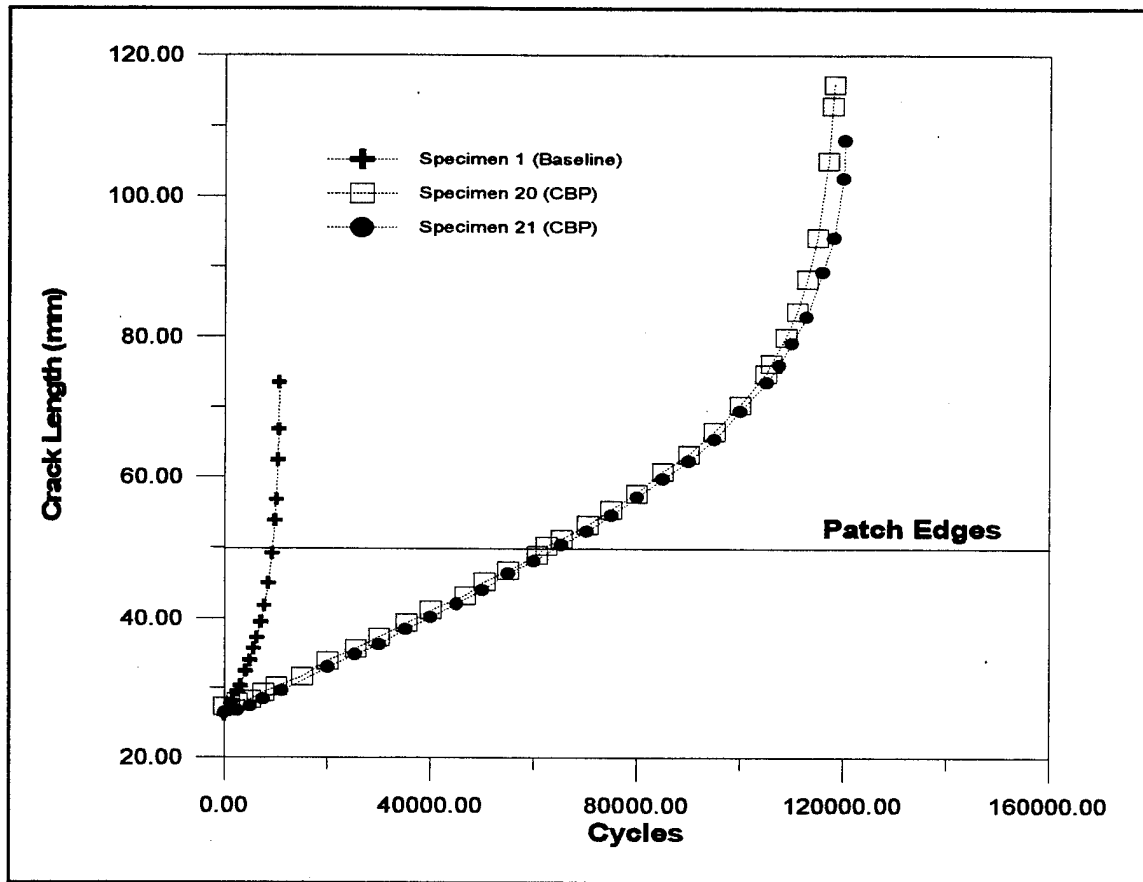
Figure 24. Baseline vs. CBP Crack Growth

factor with repair was the result of: (1) load sharing by the patch; and (2) crack bridging which reduced the crack opening displacement. The second insight gained from Figure 24 and also shown in Figure 26, for the first 20,000 cycles of both CBP specimens, is that no retardation in the crack growth rate occurred during the earlier portion of crack growth inside the patch. Again, this is in agreement with Baker (6, 7, 8) and with Figure 6. The use of the elevated cure temperature film adhesive, AF-163-2, allowed the beneficial compressive stresses in the crack tip plastic zone to be annealed out during bonding of the boron/epoxy patch to the aluminum panel, eliminating retardation in the earlier portion of
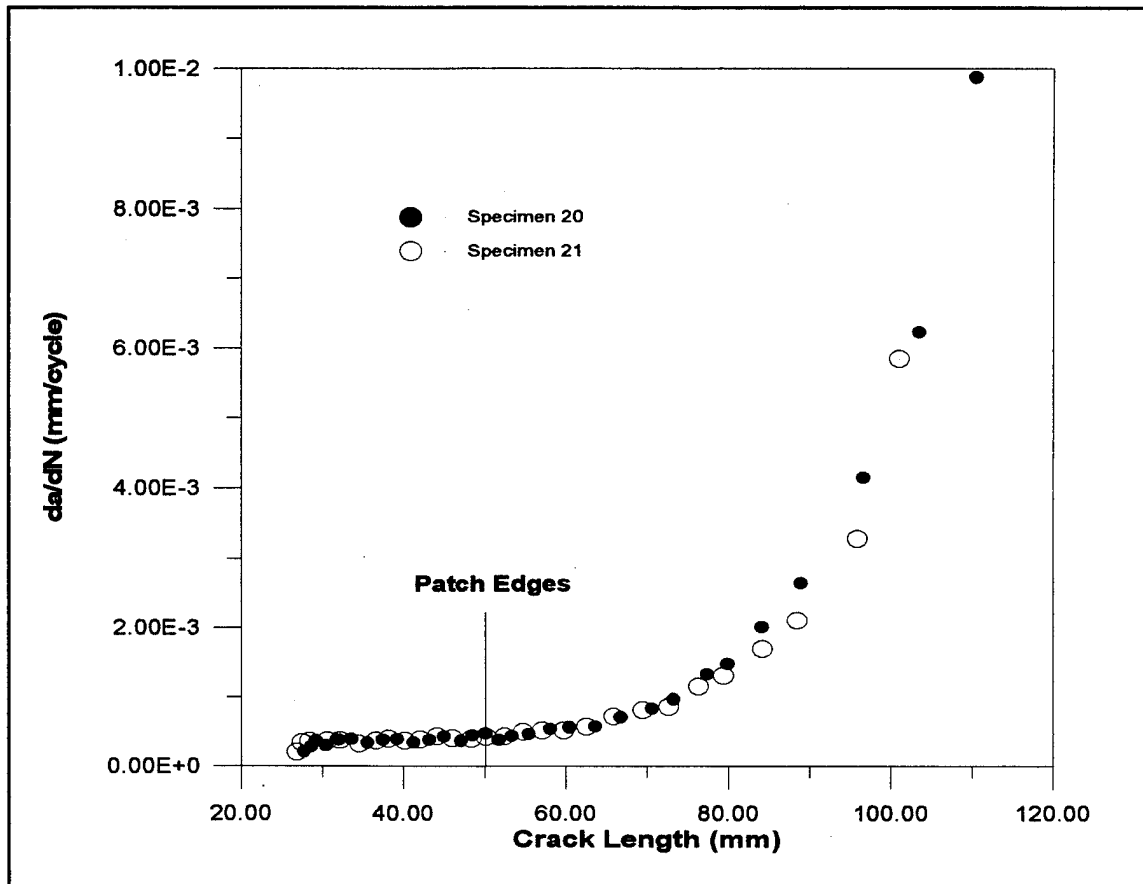
Figure 25. CBP da/dN vs. Crack Length

crack growth.

Figure 27 shows the representative pictures obtained by C-scanning at different

stages of testing of Specimen 20. Specimen 21 demonstrated similar behavior. The three

C-SCANs shown are for 0, 62,492 and 106,003 cycles which correspond to crack lengths

of 27.238 mm (1.07235 inches), 50.221 mm (1.9772 inches) and 76.211 mm (3.00045

inches). The 0 cycle C-SCAN shows no bondline flaws, i.e. a perfectly bonded patch.

The 62,492 cycle C-SCAN was taken when the crack tips had reached the patch edges.

Slight cyclic disbonding was evident in the wake of the crack tip, however, it was not
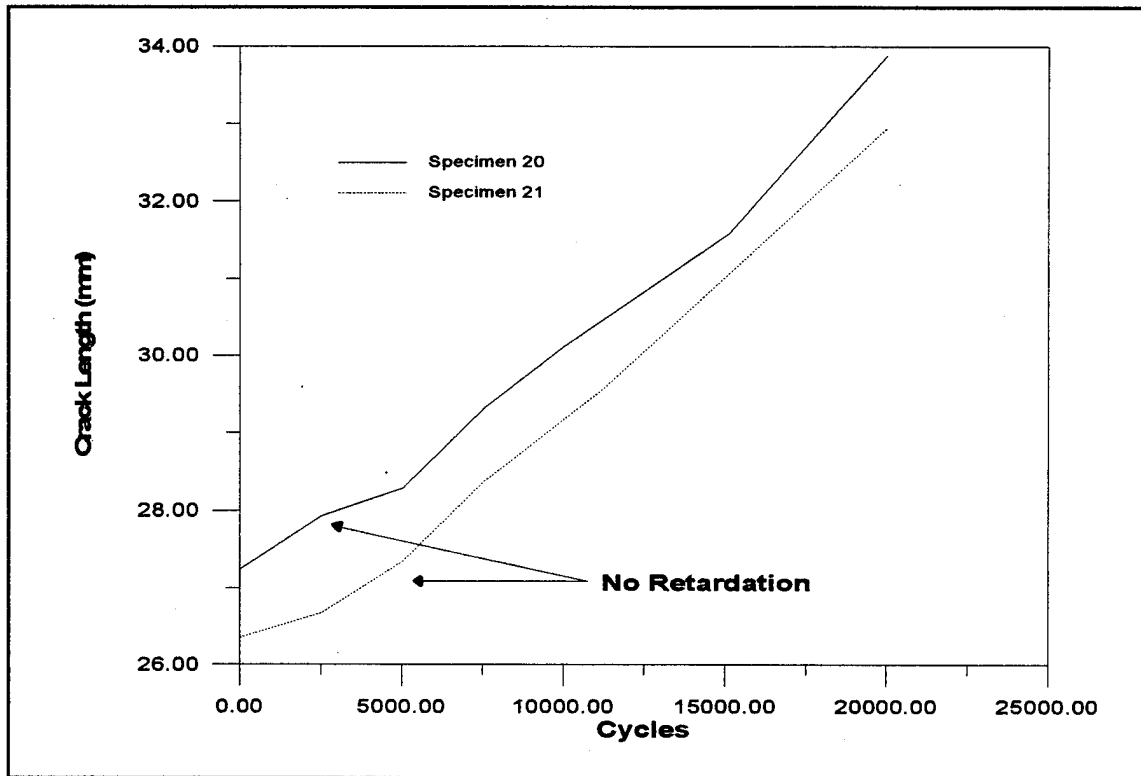
Figure 26. CBP Retardation of Crack Growth

significant and had little effect, if any, on the crack growth rate, da/dN. This is in

agreement with Baker's observations (6). This again confirms that the crack growth rate,

da/dN, and repaired stress intensity factor range, ΔK_R, should remain constant for crack

growth inside the patch. Only after the crack had extended beyond the patch edges did

considerable disbonding occur as in the 106,003 cycle C-SCAN. Also upon visual

inspection of the specimen after failure, it was determined that the cyclic disbonding

occurred between the adhesive and the boron/epoxy patch. This agreed with the findings

of Baker (8) and Russell (36) who attributed this disbonding to the light glass scrim cloth

impregnated in the epoxy of the patch and the high stresses at the repair-adhesive interface

due to the use of a high modulus adhesive.

59
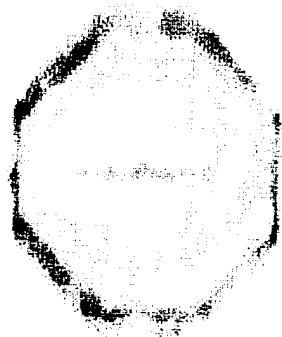
Specimen 20 (CBP)
0 Cycles
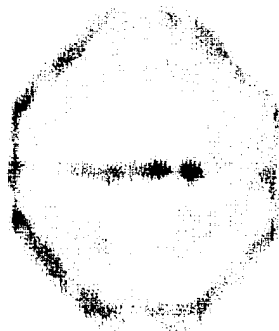
Specimen 20 (CBP)
62,492 Cycles
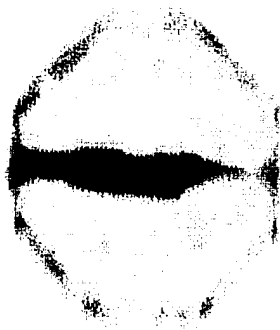
Specimen 20 (CBP)
106, 003 Cycles

Figure 27. CBP C-SCANs

Two major modes of failure occur in bonded patch repair, the patch failure mode and adhesive failure mode. Figure 28 illustrates these two failure modes. In the patch
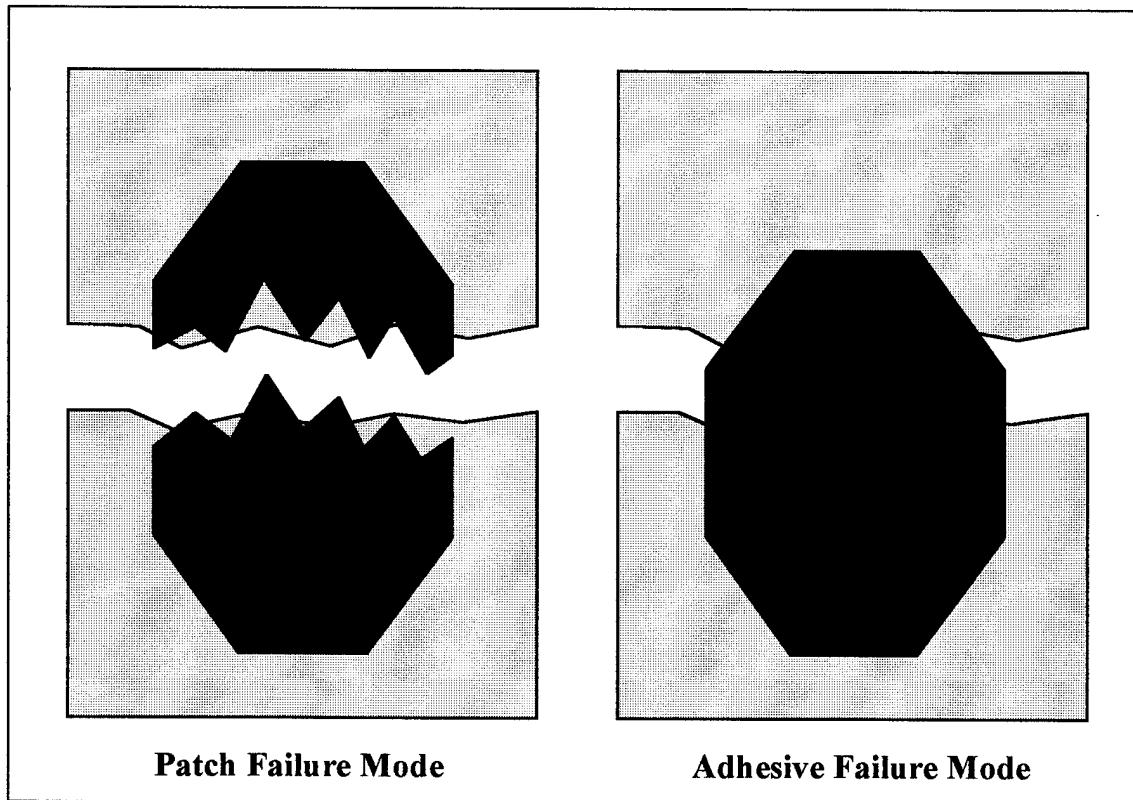
Figure 28. Failure Modes

failure mode, the patch fails with the aluminum. In the adhesive failure mode, the adhesive fails cohesively. Photographs of Specimens 20 and 21 can be found in Appendix A. These two specimens failed by the patch failure mode.

   Full Width Disbond. Two specimens with a FWD, Specimens 4 and 5, were tested with disbonds approximately 20 % of the total bond area. The total bond area

was equal to the area of the largest boron/epoxy ply which was 2822 mm^2. The disbond of the FWD specimens was 600 mm^2 with the dimensions shown in Figure 29 which was
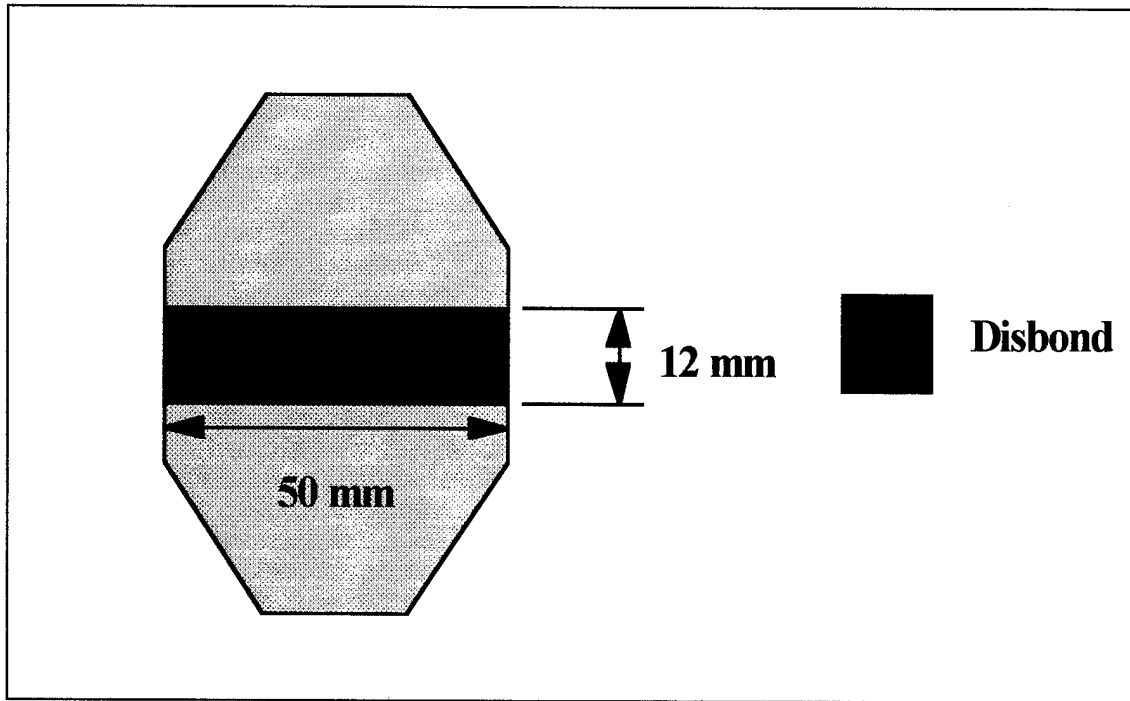
Figure 29. FWD Dimensions

21.3 % of the total bond area. The fatigue lives of these specimens are shown in Table 8, along with the baseline and two CBP specimens. The fatigue lives of Specimens 4 and 5 with a FWD were 73 % and 69 %, respectively, of the CBP specimen average of 119,320 cycles to failure, a significant reduction in total life. However, even with this reduction in patching efficiency, the FWD specimens still managed to yield an average of 7.96 times life extension over the baseline test with no patch.

Table 8. FWD vs. Baseline and CBP Fatigue Lives

Specimen	Configuration	Cycles to Failure
1	Baseline (No Patch)	10,633
4	FWD	86,995
5	FWD	82,324
20	CBP	118,316
21	CBP	120,325

Figure 30 shows the crack length versus cycles curve for the baseline, the two FWD specimens and the two CBP specimens. The crack growth rates for both FWD specimens were constant within the patch indicating that the repaired stress intensity factor range, ΔK_R, was also constant. Again, as with the CBP specimens, the crack growth curves remained constant until the crack tips had extended beyond the edges of the patch. This behavior is evident from Figure 31 using the three-point least squares method (37) to determine the relative change in crack growth rate with crack length. For comparison purposes, the average crack growth rate within the patch for the FWD and CBP specimens are shown in Table 9. On the average, the crack growth rate for the FWD specimens were 1.65 times greater than that for the CBP specimens. The greater crack growth rate was due to the point of load transfer from the plate to the patch being moved away for the crack as shown in Figure 32. Load transfer through the adhesive to the patch ceases at the point of disbonding which resulted in the aluminum plate having to carry excess load around the crack as compared to a perfectly bonded patch. This is essentially what occurs in a bolted repair. As soon as the load transfers at the rivets/bolts, the remaining load has no other means of transfer into the repair leaving it free to strain the remaining material around the crack. This causes a greater crack opening displacement,
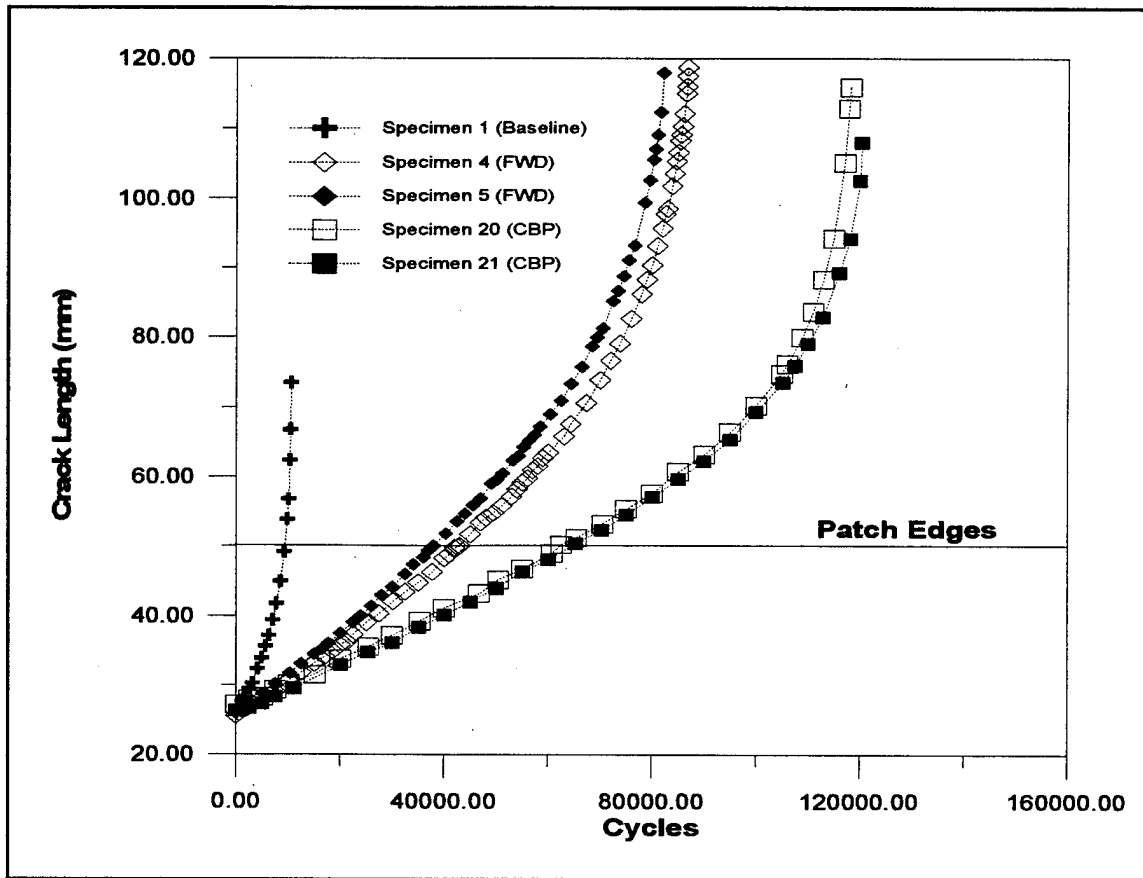
Figure 30. FWD vs. Baseline and CBP Crack Growth

thus, resulting in a greater crack growth rate.

As with the CBP specimens in Figure 26, the FWD specimens did not experience any retardation in the earlier portion of crack growth. Figure 33 shows this effect. Again this was the result of using a high cure temperature adhesive.

Figure 34 shows representative C-SCANs for Specimen 4. Specimen 5 demonstrated similar behavior. The three C-SCANs are for 0, 43,018, and 72,030 cycles which correspond to crack lengths of 25.632 mm (1.00915 inches), 50.113 mm (1.97295 inches) and 76.68 mm (3.0189 inches). The 0 cycle C-SCAN shows the FWD with
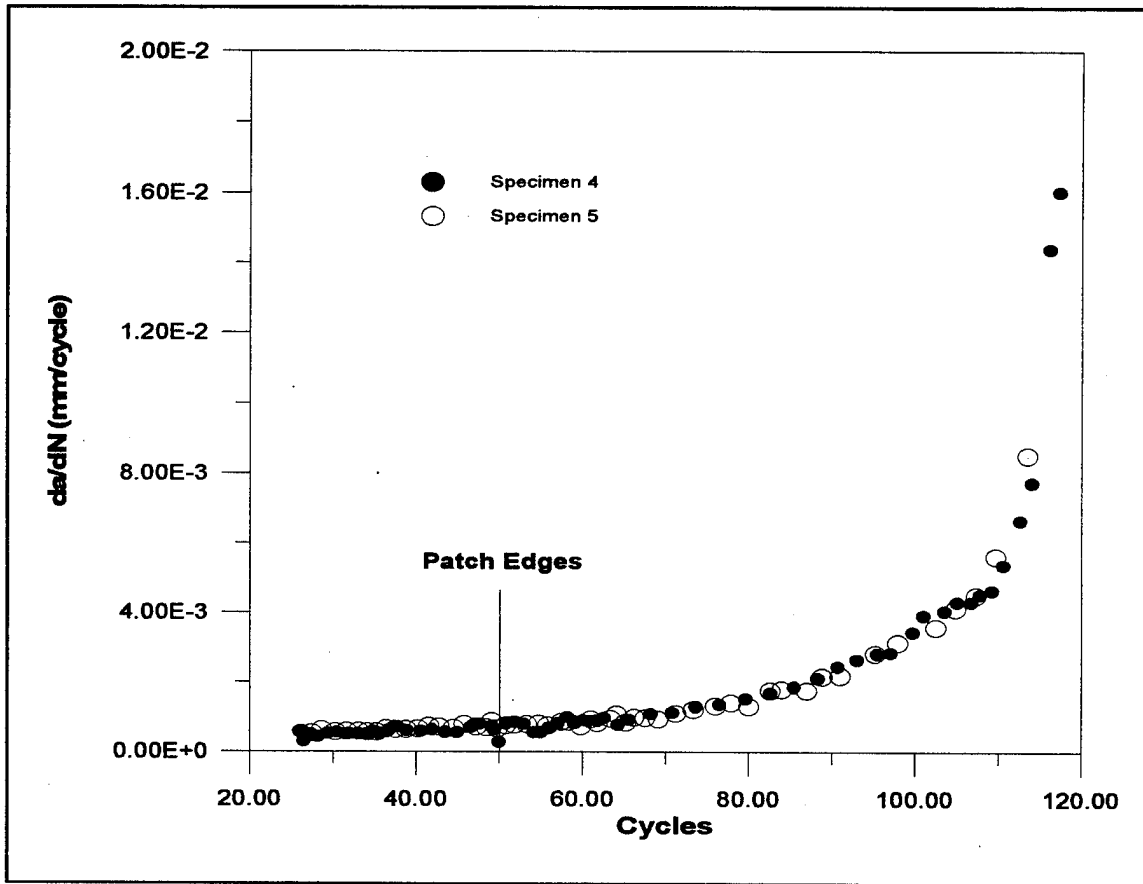
Figure 31. FWD da/dN vs. Crack Length

Table 9. da/dN for FWD and CBP Specimens

Specimen	Configuration	da/dN (mm/cycle)
4	FWD	0.0005528
5	FWD	0.00064977
20	CBP	0.00036265
21	CBP	0.00036580
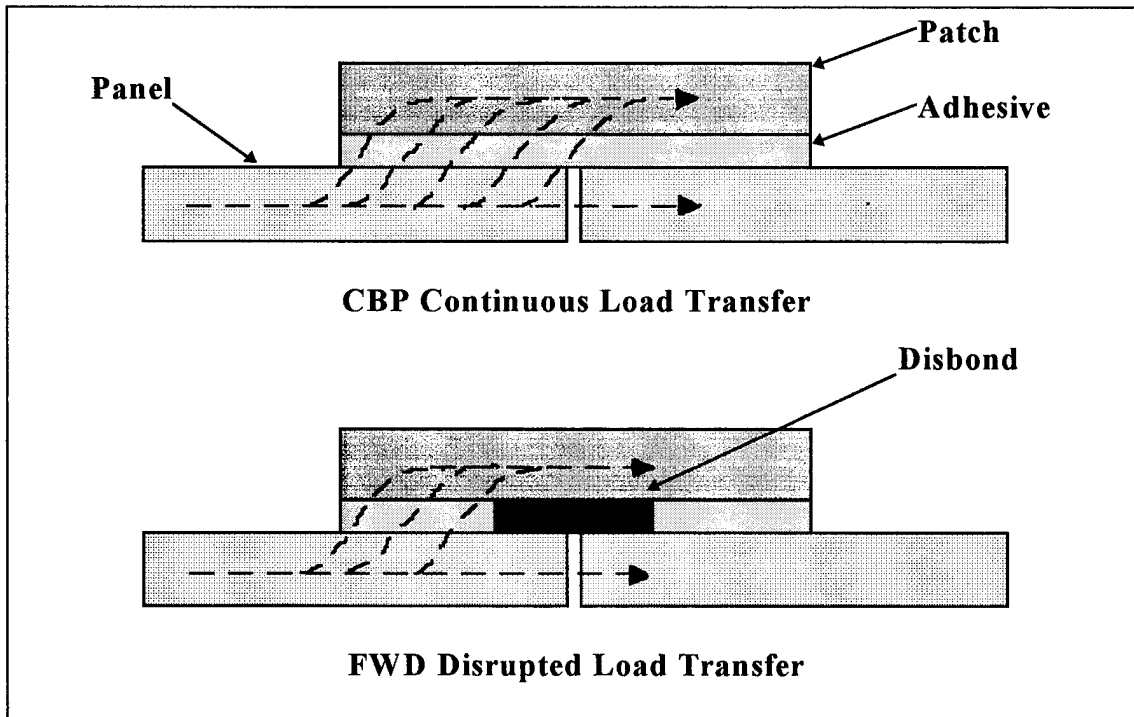
Figure 32. Load Transfer of FWD vs. CBP

dimensions as shown in Figure 29. The 43,018 cycle C-SCAN represents the point at

which the crack tips had reached the patch edges with no growth of the intentional

disbond. Even after the crack had grown beyond the patch edges, the disbond did not

increase in size or change shape. This lack of disbond growth was also reported by Baker

(6) in his study of intentional FWD specimens, i.e. there was no cyclic disbonding. Also,

as with Hart-Smith's (22) observations, the adhesive bond did not behave as a weak link,

in fact, the bondline proved to be relatively damage tolerant of the FWD. As a result of

this lack of cyclic disbonding, the crack growth rate within the patch repair was constant

as shown in Figures 30 and 31.
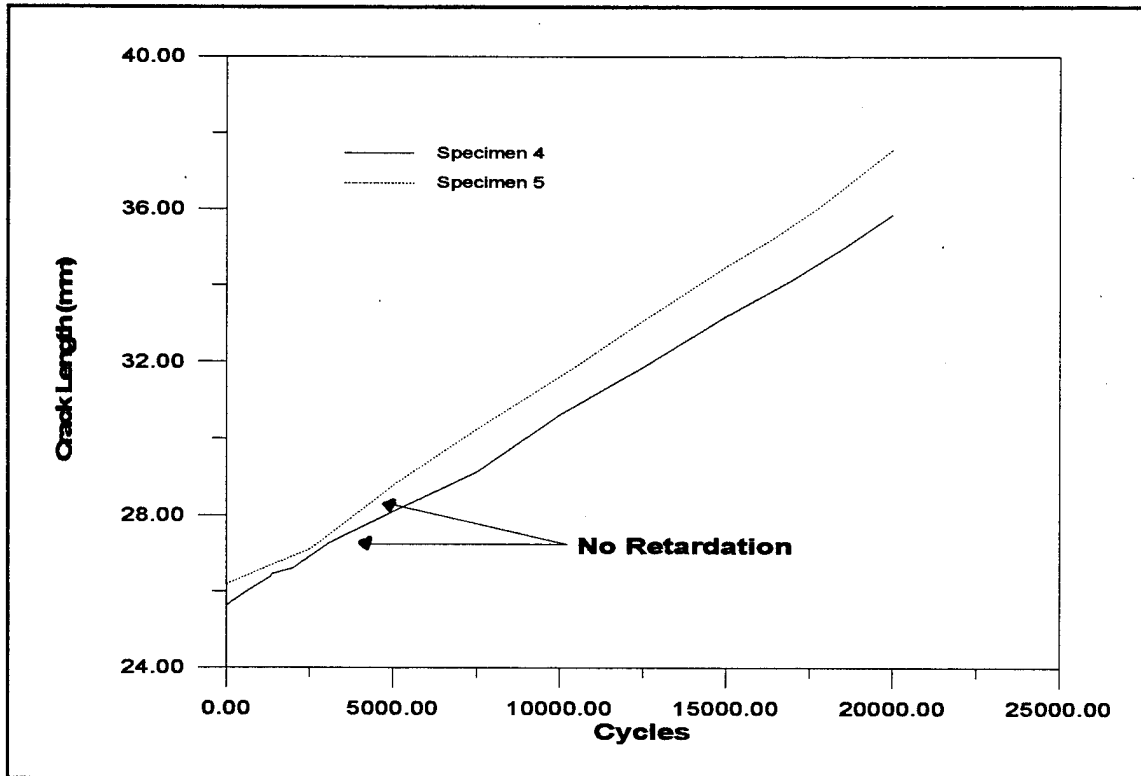
Figure 33. FWD Retardation of Crack Growth

Finally, the two FWD specimens failed by the patch failure mode as shown in Figure 28 and Appendix A.

Crack Tip Disbonds. Two specimens with CTD, Specimen 6 and Specimen 7, were tested with a disbond approximately 20 % of the total bond area. Each crack tip disbond was 288 mm^2 equaling 10.2 % of the total bond area, therefore, both crack tip disbonds resulted in a combined 20.4 % disbond of the total bond area. The disbond dimensions are shown in Figure 35. The fatigue lives of the two CTD specimens along with the baseline and CBP specimens are shown in Table 10. The fatigue life of Specimen 6 was 78 % of the average life of 119,320 cycles, for the CBP specimens, and

67
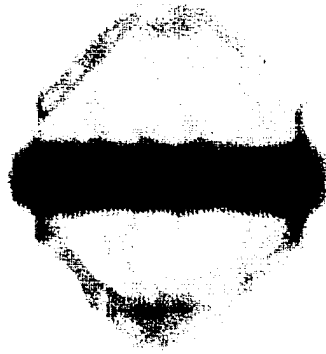
Specimen 4 (FWD)
0 Cycles
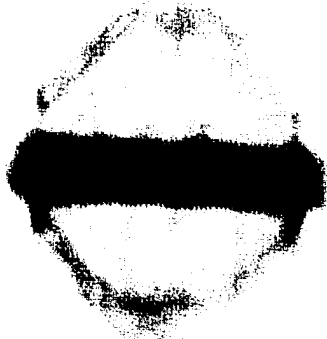
Specimen 4 (FWD)
43,018 Cycles
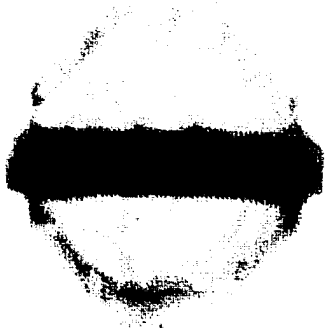
Specimen 4 (FWD)
72,030 Cycles

Figure 34. FWD C-SCANs
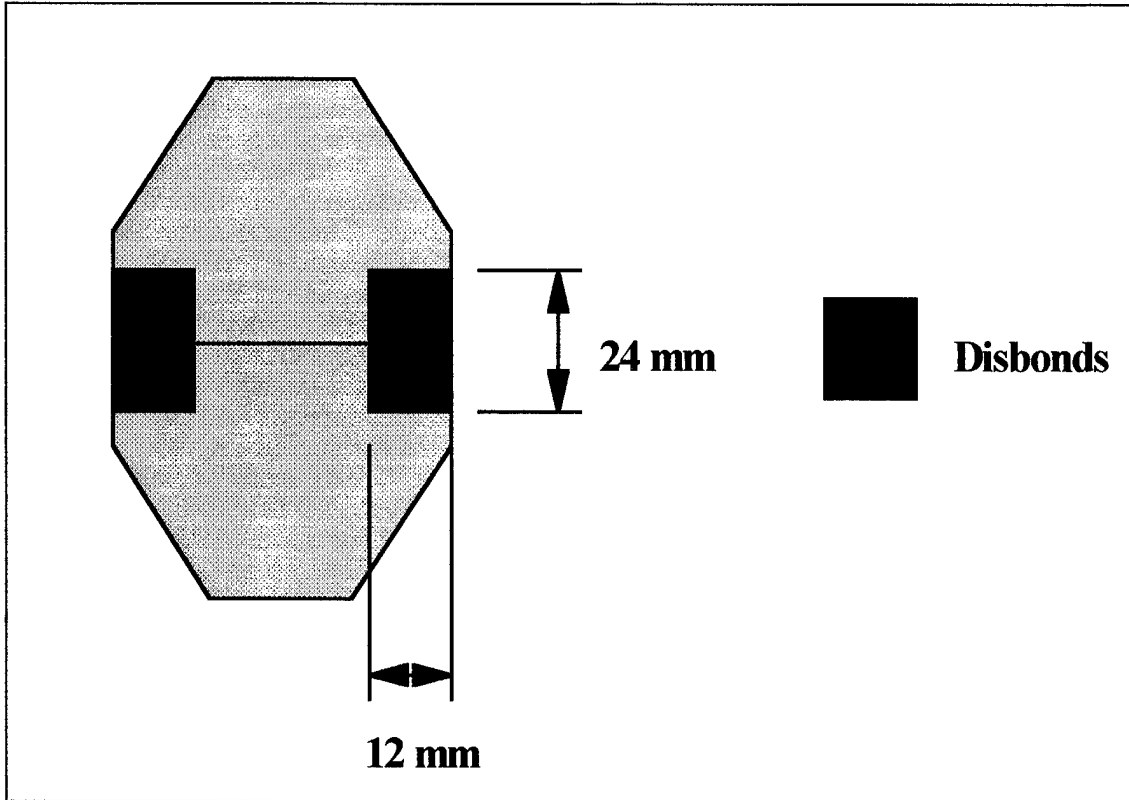
Figure 35. CTD Dimensions

for Specimen 7, it was 88 % of the CBP average. In comparison to this reduction of

patching efficiency, the CTD specimens provided an average of 9.59 times life extension

over the baseline test without a patch.

Figure 36 shows the crack length versus cycles curve for the baseline, the two

CTD specimens and the two CBP specimens. The crack growth rates for both the CTD

specimens were initially constant and similar to that of the CBP Specimens, however, the

crack growth rates of the CTD specimens tend to increase slightly as the crack grew

further into the disbond areas and closer to the patch edges. As more of the intentional

Table 10. CTD vs. Baseline and CBP Fatigue Lives

Specimen	Configuration	Cycles to Failure
1	Baseline (No Patch)	10,633
6	CTD	98,439
7	CTD	105,478
20	CBP	118,316
21	CBP	120,325

CTD disbonds made an appearance in the wake of the crack tips during crack growth, it simulated the cyclic disbonding that Baker (6, 8) described, thus resulting in a greater crack opening displacement about the crack tip and an increased repaired stress intensity factor range, ΔK_R. For the case studied here, this increasing trend in crack growth was small and can be assumed to be negligible as shown in Figure 37. However, if the patch was wider with a similar crack tip disbond, a more noticeable effect on da/dN with crack length would have been observed. This also supports Baker's (6) observation that disbonds in front of the crack tip have little effect on the rate of crack propagation, i.e. it was not until the disbonds made an appearance behind the crack tip did they have an effect. For illustration purposes, Table 11 compares the average crack growth rates for the CTD specimens with that of the CBP specimens within the patch. The crack growth rates presented are the average growth rates, within the patch, computed by the three-point least squares method (37). On average, the crack growth rate for the CTD specimens was 1.16 times greater than that for the CBP specimens.

As with the CBP and FWD specimens, the CTD specimens did not experience any retardation in the earlier portion of crack growth as shown in Figure 38. This was again the result of the annealing out of the beneficial compressive stresses ahead of the crack tip
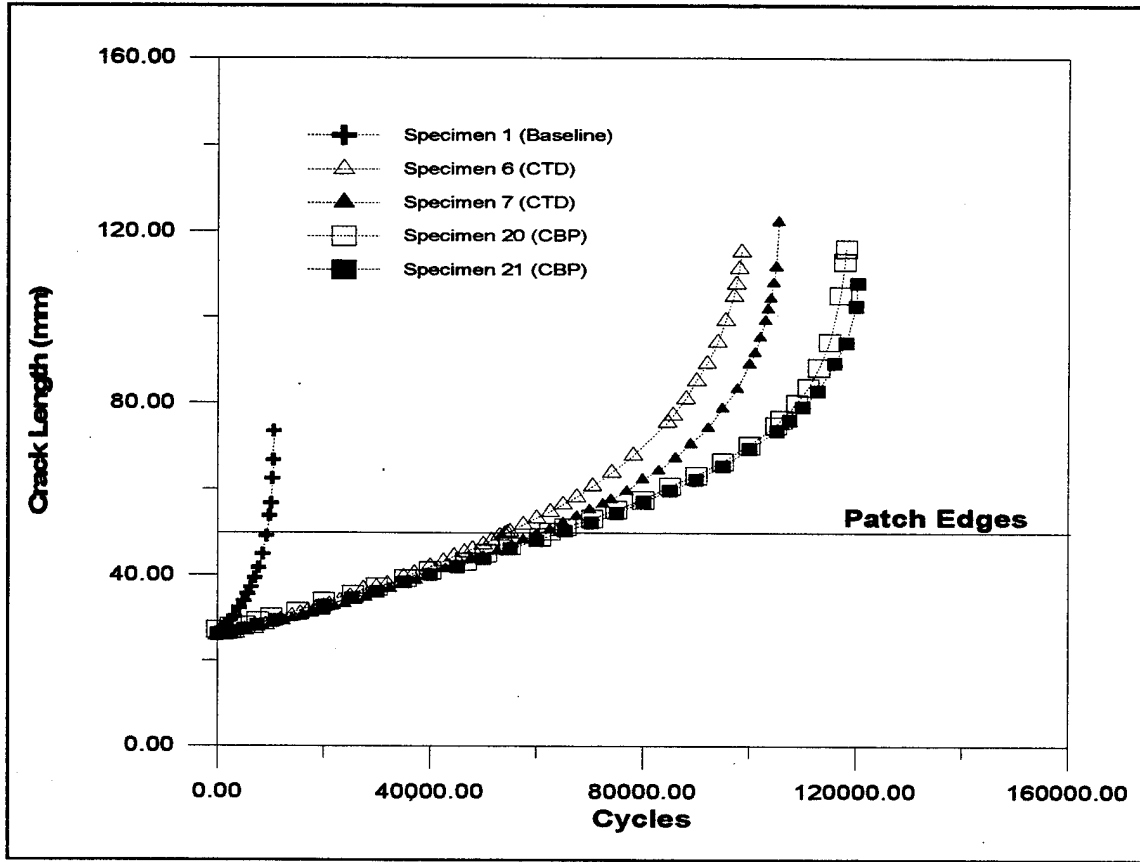
Figure 36. CTD vs. Baseline and CBP Crack Growth

during the bonding process.

Figure 39 shows the representative C-SCANs for Specimen 6. Specimen 7

demonstrated similar behavior. The three C-SCANs are for 0, 54,982, and 85,615 cycles

which corresponds to crack lengths of 25.791 mm (1.0154 inches), 50.104 mm (1.9726

inches) and 77.121 mm (3.03625 inches). The 0 cycle C-SCAN shows the intentional

disbonds in front of the crack tips with the dimensions shown in Figure 35. At 54,982

cycles, the crack tips were at the edges of the patch. No growth of the intentional

disbonds occurred up to 54,982 cycles, however, slight cyclic disbonding did occur

between the two intentional disbonds. At 85,615 cycles, the cyclic disbonding showed
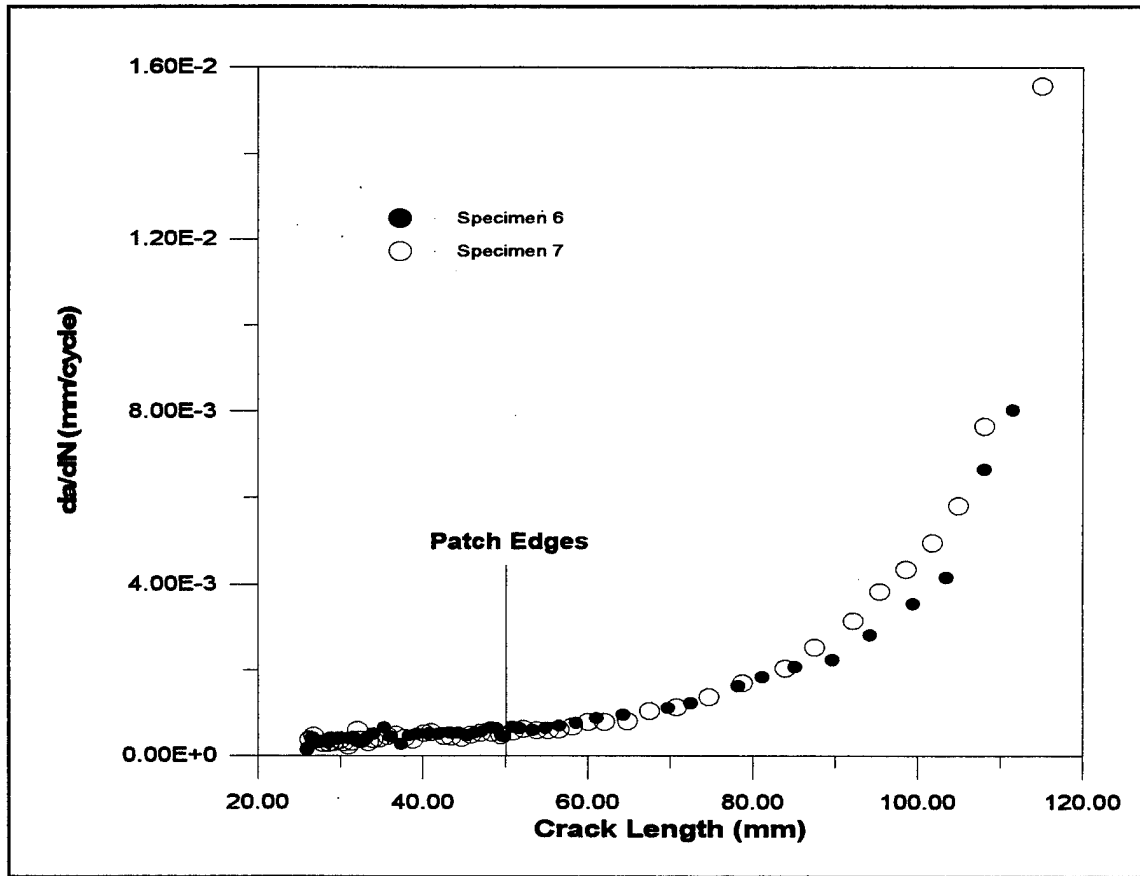
Figure 37. CTD da/dN vs. Crack Length

Table 11. da/dN for CTD and CBP Specimens

Specimen	Configuration	da/dN (mm/cycle)
6	CTD	0.00043336
7	CTD	0.00041077
20	CBP	0.00036265
21	CBP	0.00036580
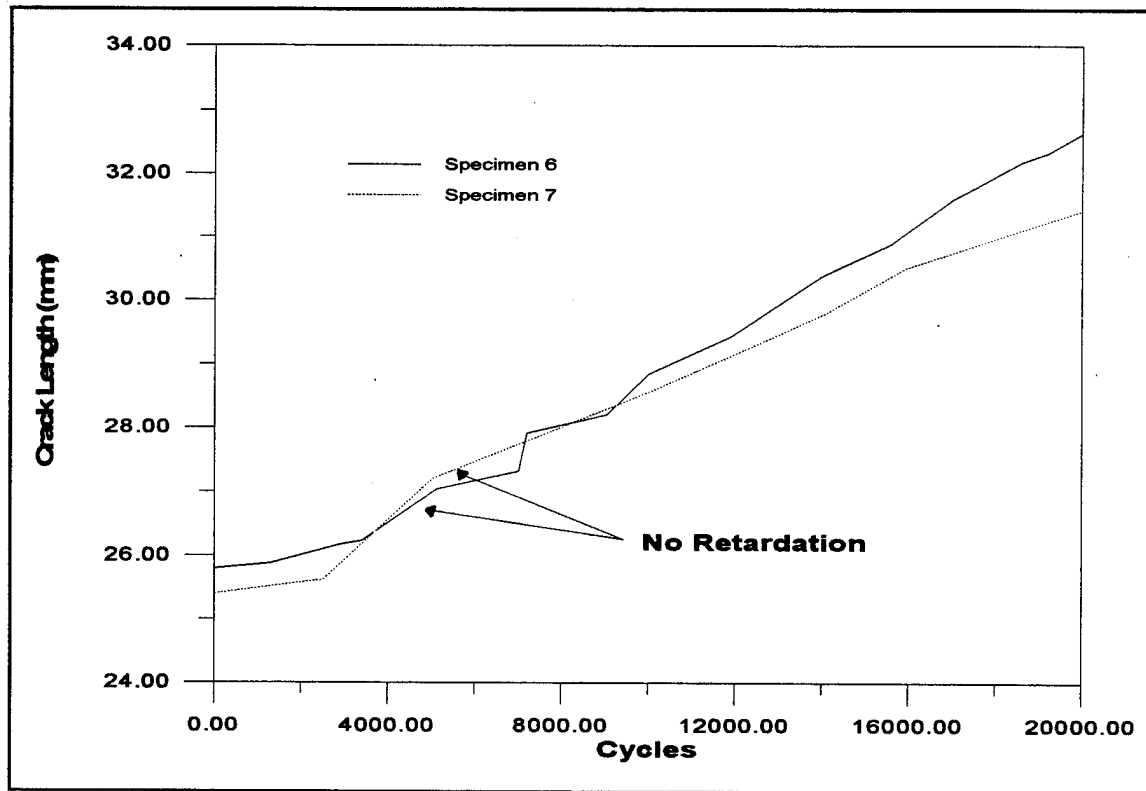
Figure 38. CTD Retardation of Crack Growth

little progression and the intentional disbonds showed no growth. Hart-Smith's (22)

findings are again true in this case. The bondline was relatively damage tolerant with no

progression of the pre-existing intentional disbonds.

Again, the two CTD specimens failed by the patch failure mode as shown in Figure

28 and Appendix A.

End Disbonds. Three specimens with ED, Specimens 8, 9 and 12, were

tested with disbonds approximating 20 % of the total bond area. Two ED specimen

configurations, ED1 and ED2, were studied with the dimensions shown in Figure 40.

Each disbond of the ED1 configuration was 288 mm^2 equaling 10.2 % of the total bond

area with both disbonds combining for a total of 20.4 % of disbond. The end disbonds

73

Specimen 6 (CTD)
0 Cycles
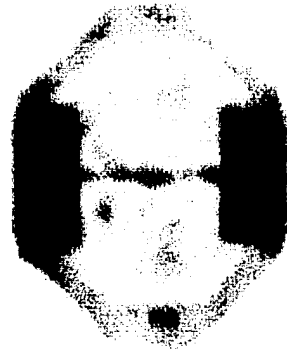
Specimen 6 (CTD)
54,982 Cycles
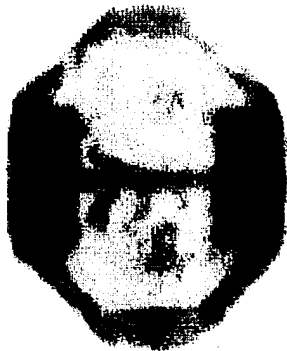
Specimen 6 (CTD)
85,615 Cycles

Figure 39. CTD C-SCANs

of the ED2 configuration were 270 mm^2 combining to give a 19.1 % total disbond. The difference between the ED1 and ED2 configurations is illustrated in Figure 40. The fatigue lives of the three ED specimens, the baseline specimen and the two CBP specimens are shown in Table 12. The fatigue life of Specimen 8 was 16.5% greater than the CBP average of 119,320 cycles and Specimen 9 was 14% greater than the CBP average. Also, Specimen 12 was 15.5% greater than the CBP average. These equate to a 13.07 times life extension over the baseline specimen for Specimen 8, a 12.78 times life extension for Specimen 9 and a 12.96 times life extension for Specimen 12. Also, there was practically no difference in the fatigue life between the two configurations of end disbonds, i.e. ED1 versus ED2.

Figure 41 shows the crack growth curves for the baseline specimen, the three ED specimens and the two CBP specimens. The crack growth rates for all three ED specimens were constant within the patch, as shown in Figure 41 and Figure 42, indicating a constant repaired stress intensity factor range, ΔK_R. As with the CBP and FWD specimens, the crack growth curves remained linear until the crack tips had extended beyond the patch. Table 13 shows the average crack growth rate within the patch as well as the initial repaired stress intensity factor, K_R, for the ED and CBP specimens. The repaired stress intensity factors were calculated using the Rose model (33, 34, 35) with the corresponding initial crack length for each specimen as shown in Table 5. In these calculations, the length of the patch with end disbonds was reduced by the length of the disbond. The presence of end disbonds essentially made the patch shorter in length. From the inclusion analogy (33, 34), the patch and the plate together behave as a region of
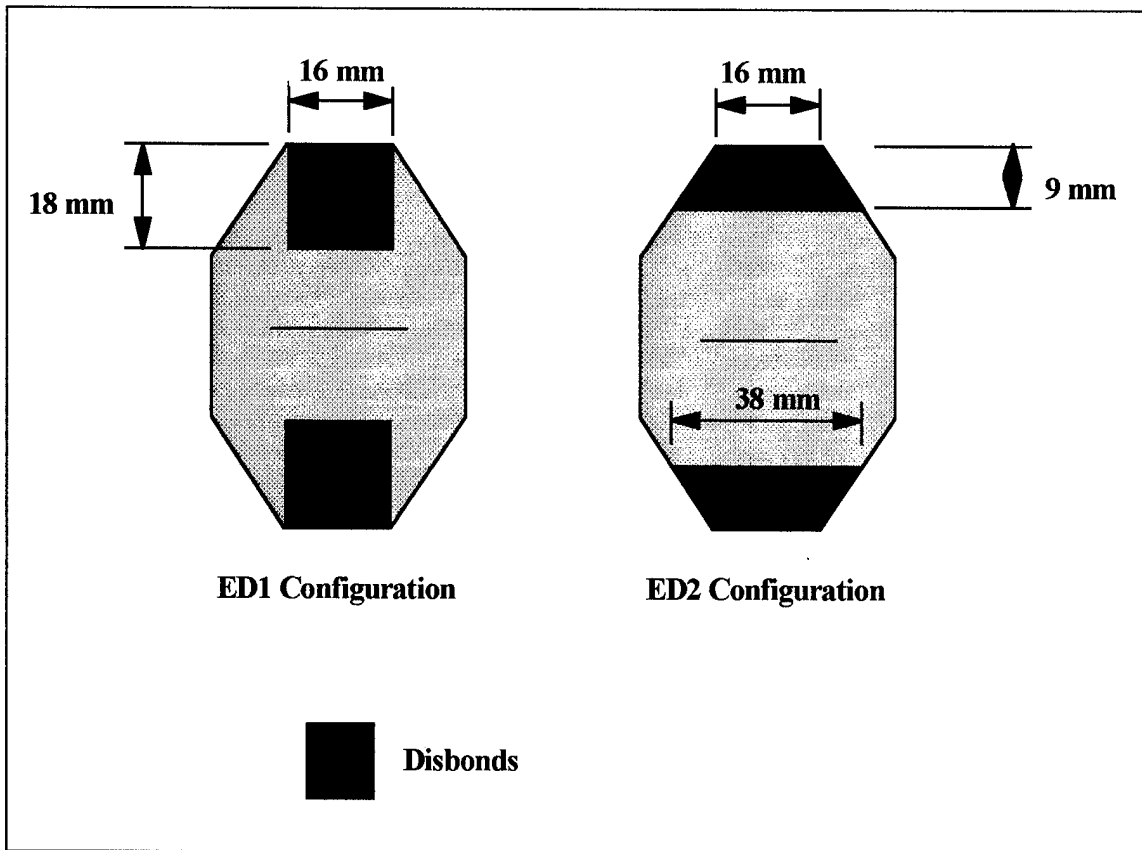
Figure 40. ED Dimensions

Table 12. ED vs. Baseline and CBP Fatigue Lives

Specimen	Configuration	Cycles to Failure
1	Baseline (No Patch)	10,633
8	ED1	139,013
9	ED1	135,942
12	ED2	137,859
20	CBP	118,316
21	CBP	120,325
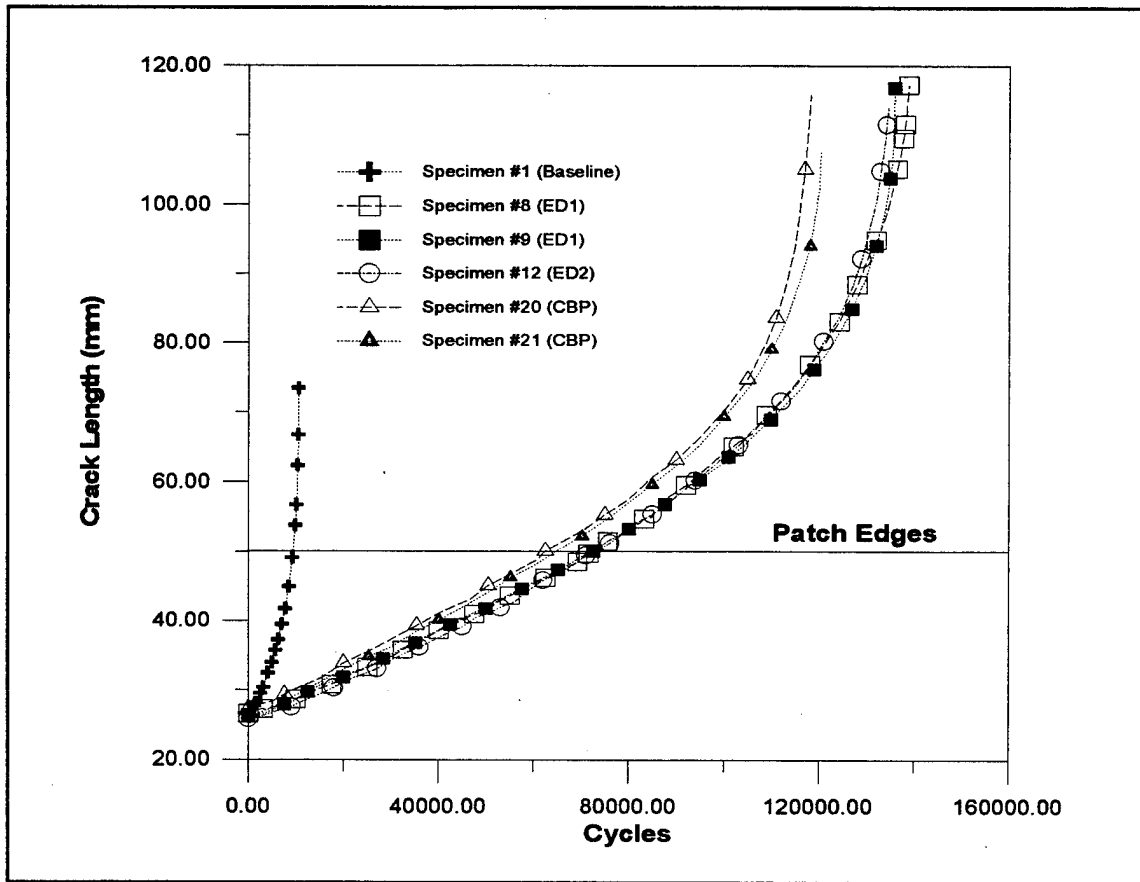
Figure 41. ED vs. Baseline and CBP Crack Growth

higher stiffness, attracting parasitic load. If this region's longitudinal length is decreased, the region of higher stiffness is reduced in size, and less load is attracted into it resulting in a reduced patch and plate stress around the crack and, thus, a reduced repaired stress intensity factor, K_R. This phenomenon is illustrated in Figure 43. However, this fact should not deter the repair designer from using a patch that meets the standard length requirements for a single-sided patch (80-100 times the repair thickness). This additional length is required for margin, especially for those cases were disbond growth is prevalent. The additional length/bond area is essentially a safety net that anchors the repair to the
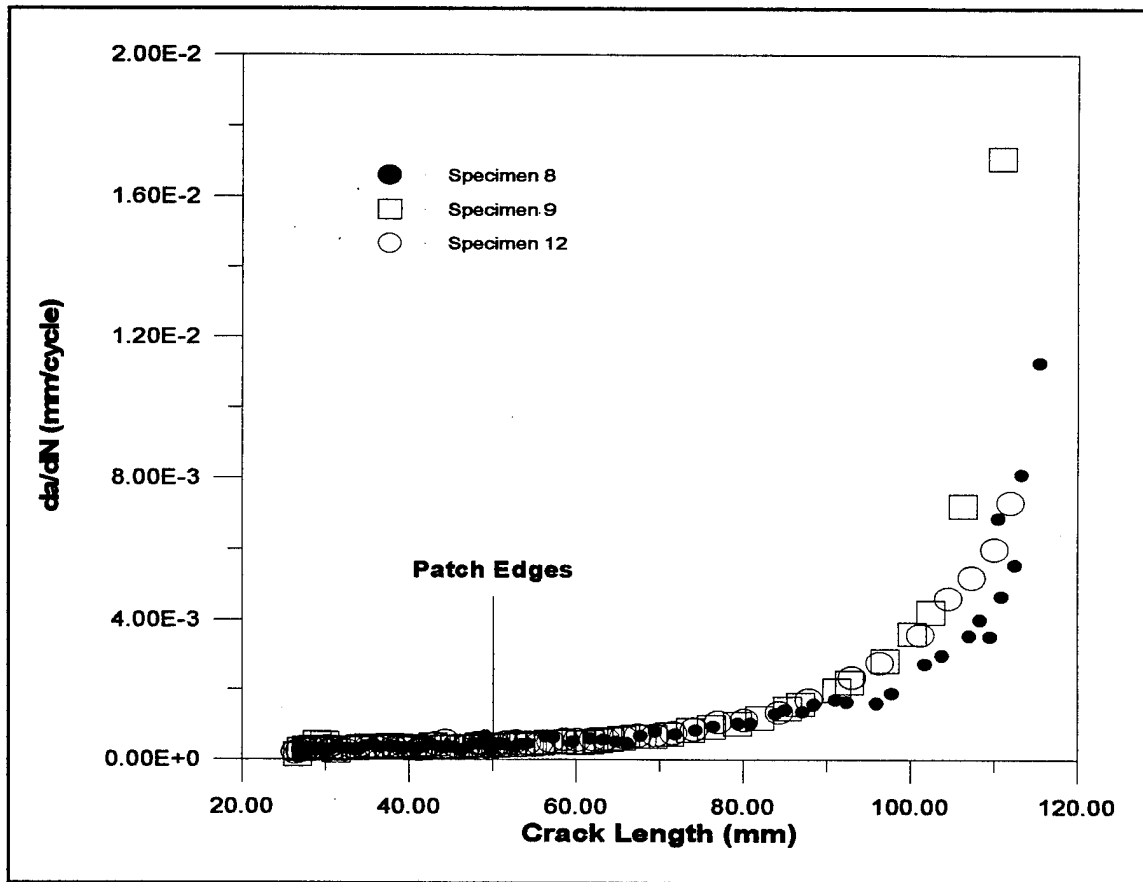
Figure 42. ED da/dN vs. Crack Length

Table 13. da/dN and K_R for ED and CBP Specimens

Specimen	Configuration	da/dN (mm/cycle)	K_R (MPa $\sqrt{m}$)
8	ED1	0.000324439	4.82
9	ED1	0.000339519	4.80
12	ED2	0.000340578	5.13
20	CBP	0.00036265	5.43
21	CBP	0.00036580	5.42
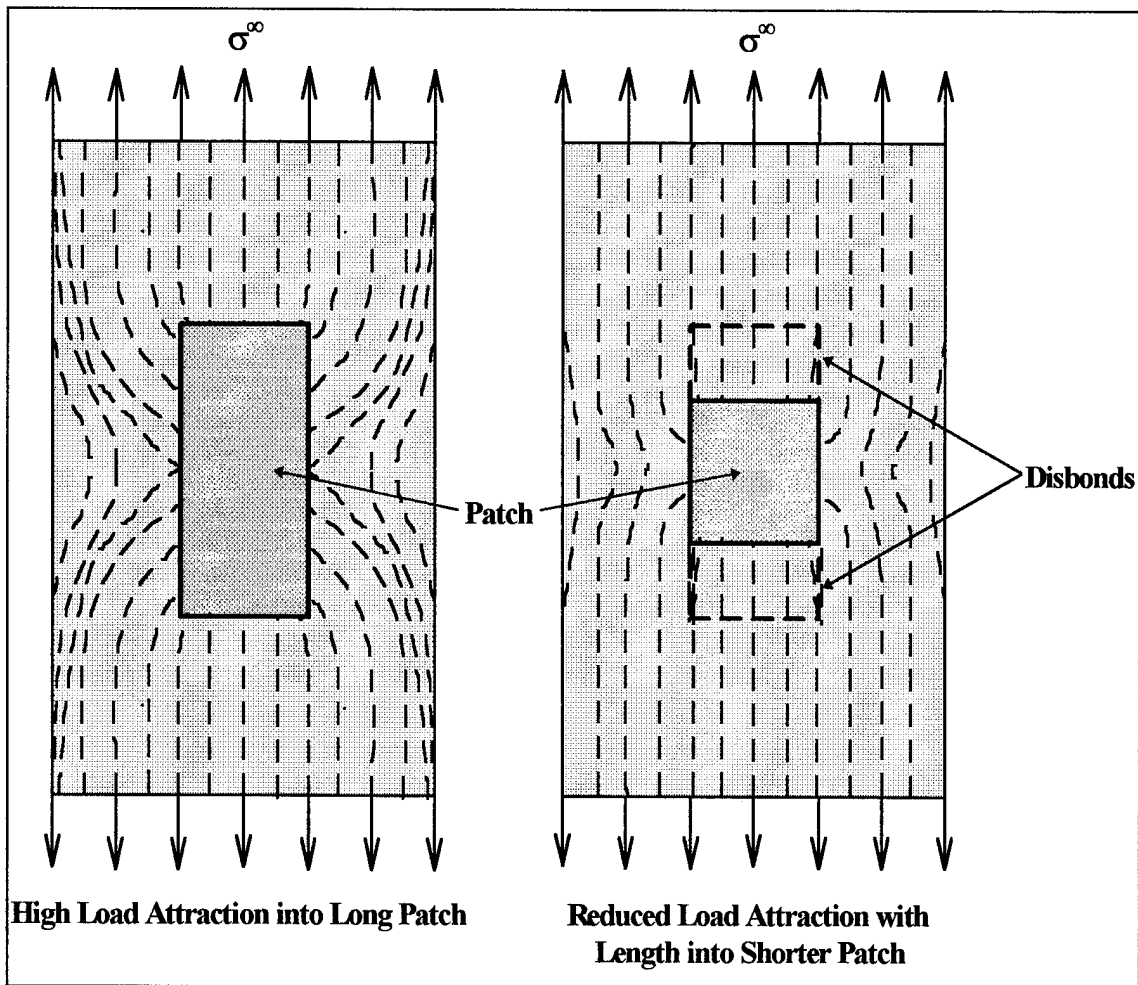
Figure 43. Reduced Load Attraction into a Shorter Repair

panel, protecting the integrity of the repair from bondline defects.

As with the all prior specimen configurations, the ED1 and ED2 configurations demonstrated no initial retardation as shown in Figure 44. Again, this was the result of using a high cure temperature adhesive.

Figure 45 shows the C-SCANs for the ED1 configuration (Specimen 8) and the ED2 configuration (Specimen 12). Specimen 9 (ED1 configuration) demonstrated similar behavior to Specimen 8. The three ED1 configuration C-SCANs are for 0, 72,013, and
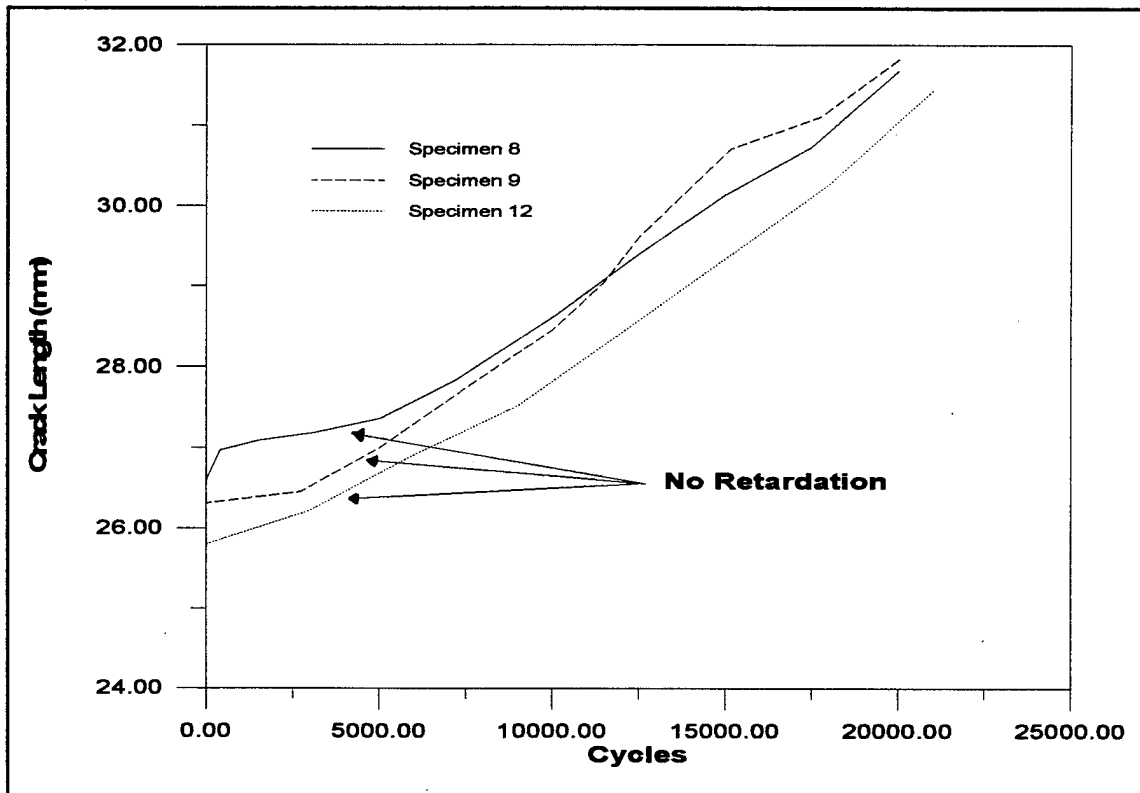
Figure 44. ED Retardation of Crack Growth

118,076 cycles which correspond to crack lengths of 26.597 mm (1.0471 inches), 49.996 mm (1.96835 inches), and 76.902 mm (3.02765 inches). The three ED2 configuration C-SCANs are for 0, 73,504, 118,004 cycles which correspond to crack lengths of 25.799 mm (1.0157 inches), 50.225 mm (1.97855 inches), and 76.789 mm (3.0232 inches). The Specimen 8 and 12, 0 cycle C-SCANs show the ED1 and ED2 configurations with the dimensions shown in Figure 40. At 72,013 cycles, the ED1 configuration showed no disbond growth and little cyclic disbonding around the crack, however, at 118,076 cycles it showed significant cyclic disbonding, consistent with the CBP specimens, once the crack had extended beyond the patch. The ED2 configuration also demonstrated little cyclic

80

Specimen 8 (ED1)
0 Cycles

Specimen 12 (ED2)
0 Cycles

Specimen 8 (ED1)
72,013 Cycles

Specimen 12 (ED2)
73,504 Cycles

Specimen 8 (ED1)
118,076 Cycles

Specimen 12 (ED2)
118,004 Cycles
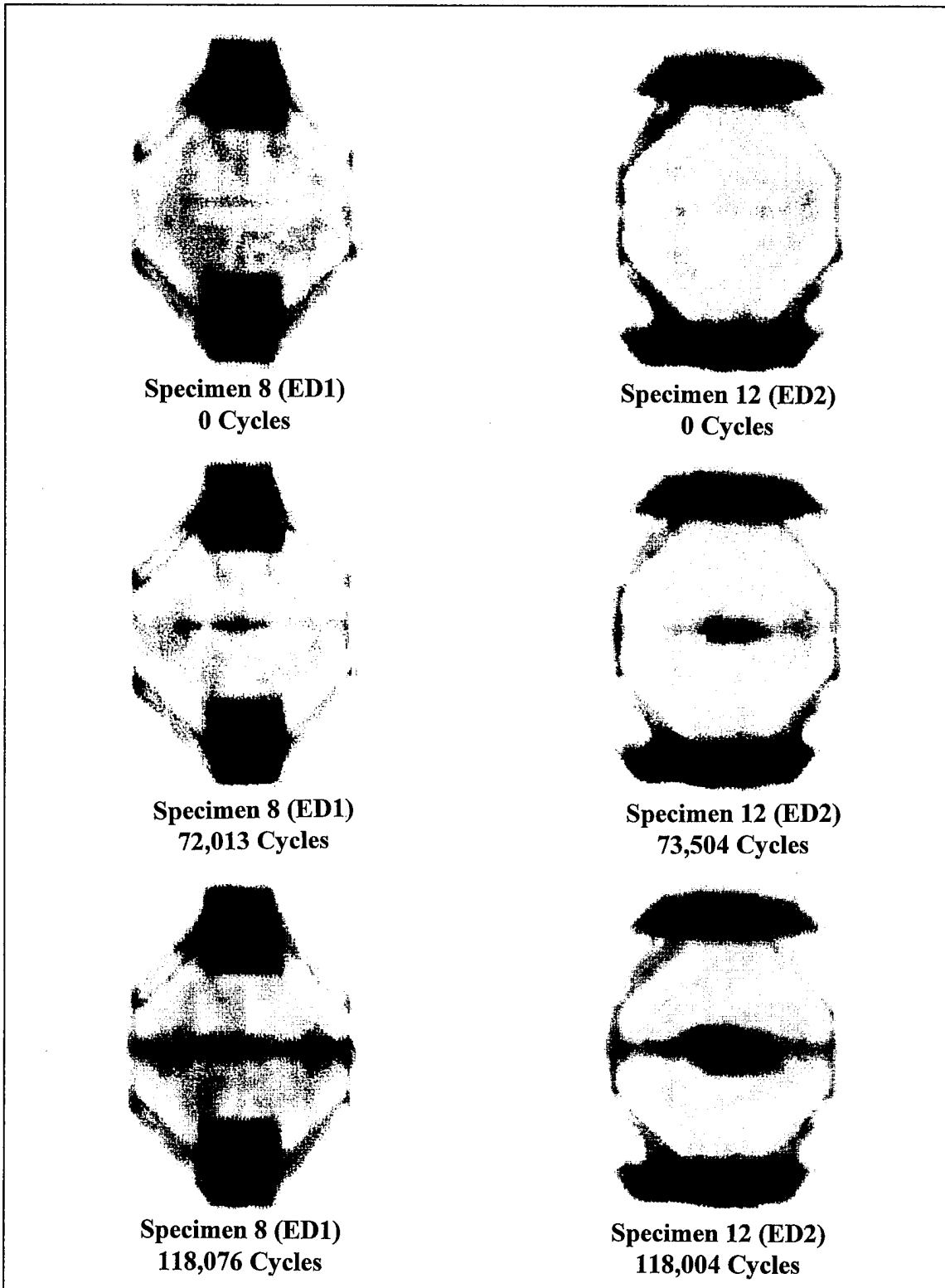
Figure 45. ED1 and ED2 C-SCANs

disbonding when the crack had reached the patch edges (73,504 cycle C-SCAN) with significant cyclic disbonding in the wake of the crack tips once they grew beyond the patch edges (118,004 cycle C-SCAN). In accordance with Hart-Smith's observations (22), the end disbonds did not show any growth, even at the ends of the patch where high stresses are prevalent, due to the strength of the bondline and the use of a thin repair. The use of a thin repair resulted in minimal neutral axis offset with minimal secondary bending and peel effects at the ends.

All three ED specimens failed by the patch failure mode as shown in Figure 28 and Appendix A.

Center Disbond. Specimen 16 with a CD is presented here to investigate the effect of location, but it contained a disbond approximately one-half the size of that presented thus far. The CD specimen dimensions are shown in Figure 46. The center disbond was 312 mm^2, equaling 11 % of the total bond area. It will be shown later that the effect of disbond size (between 10 % and 20 %) has far less effect than the location, and therefore, this center disbond case can be included here to investigate the effect of different locations. The fatigue life of the CD specimen, the baseline specimen and the two CBP specimens are shown in Table 14. The fatigue life of the specimen with a CD was 22.4 % less than the CBP average of 119,320 cycles. Even with this large reduction in patching efficiency as compared to the CBP specimens, the CD specimen still achieved 8.71 times life extension over the baseline specimen. As expected this fell between the average FWD specimen life extension of 7.96 times and the average CTD specimen life extension of 9.59 times. Explanation of this will follow.

Figure 47 shows the crack growth curves for the baseline specimen, the CD specimen and the two CBP specimens. The crack growth rate for the CD specimen was constant within the patch, once again indicating a constant repaired stress intensity factor range, ΔK_R. The crack growth rate remained constant until the crack tips had extended beyond the patch edges as shown in Figure 48. Figure 49 shows the crack growth of the CD specimen versus the two FWD specimens and the two CTD specimens. The CD specimen crack growth rate was less than the FWD specimens because the load transfer into the patch was more efficient. As the crack grew beyond the disbond and out to the patch edges the load transfer about the crack tip was not displaced as with a FWD specimen (Figure 32). The CTD specimen was more efficient than the CD specimen because the majority of the crack is perfectly bonded during crack growth within the patch
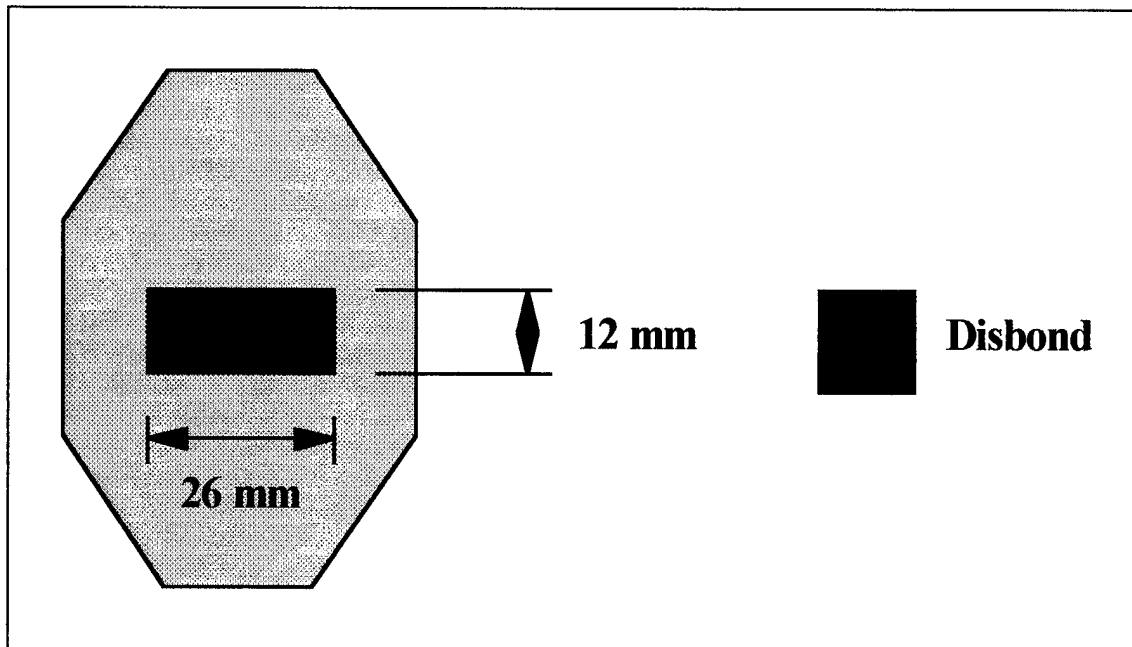
Figure 46. CD Dimensions

Table 14. CD vs. Baseline and CBP Fatigue Lives

Specimen	Configuration	Cycles to Failure
1	Baseline (No Patch)	10,633
16	CD	92,624
20	CBP	118,316
21	CBP	120,325
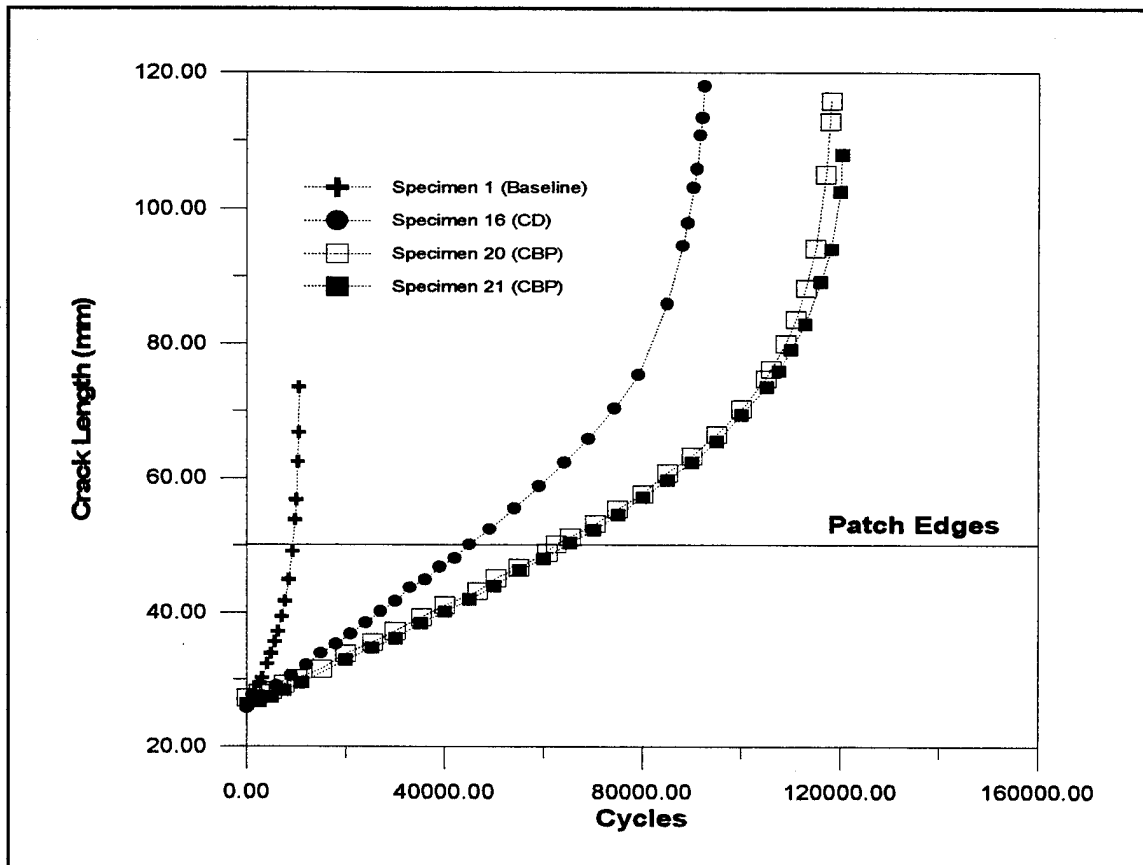
Figure 47. CD vs. Baseline and CBP Crack Growth
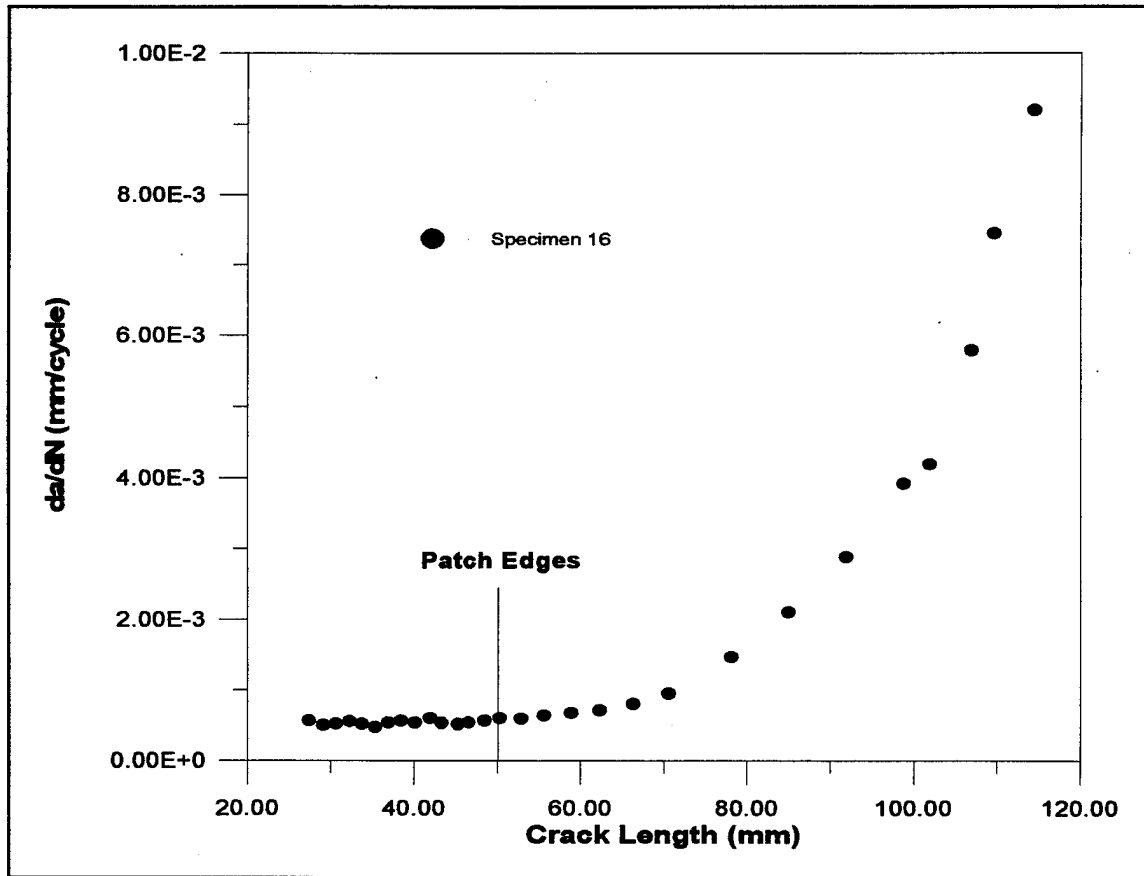
Figure 48. CD da/dN vs. Crack Length

repair, allowing more efficient load transfer into the repair around the crack. Essentially,

the larger the disbond covering the crack during crack growth within the patch the greater

the crack opening displacement and crack growth rate. The average crack growth rates

within the patch for the FWD, CTD and CD specimens are shown in Table 15 for

comparison purposes. These crack growth rates were computed by the least-squares

method (37). On average, the CD specimen crack growth rate was 0.89 times that of the

FWD specimens and 1.27 times that of the CTD specimens.

As with all the specimens discussed so far, the CD specimen does not experience
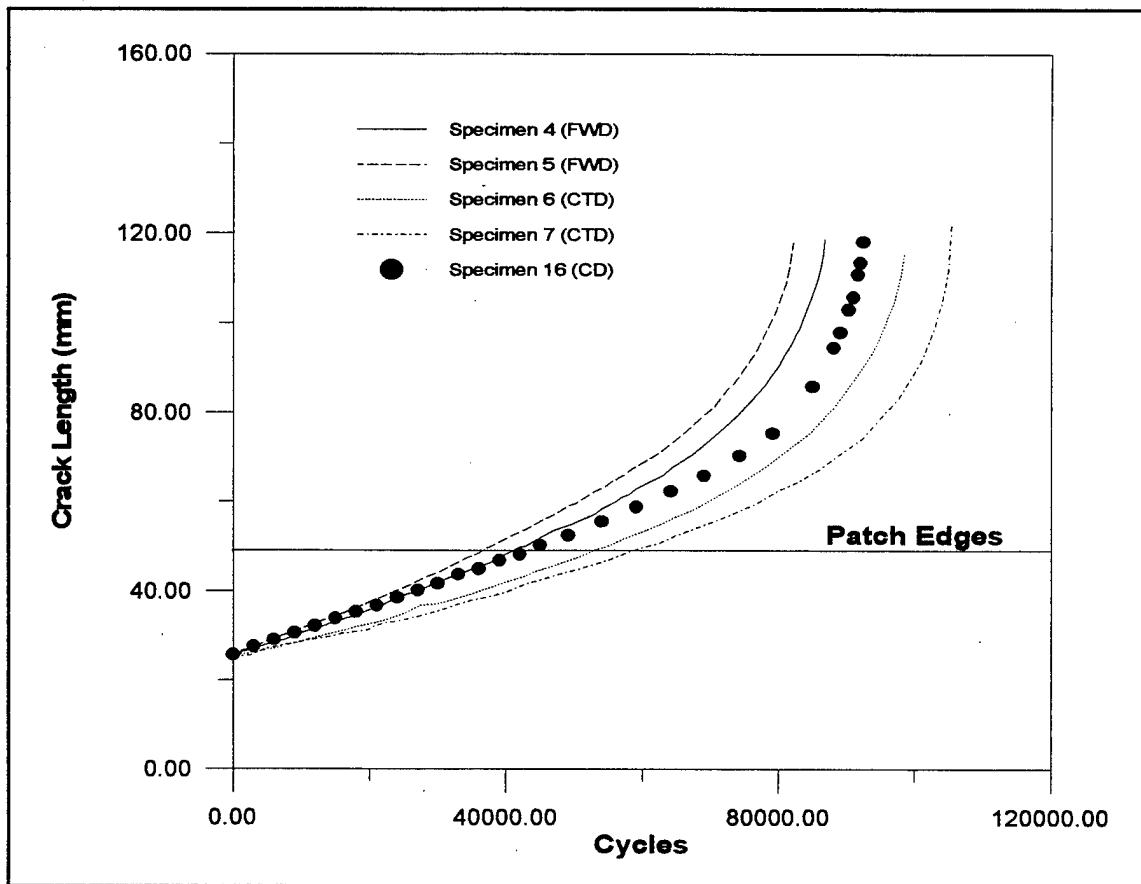
Figure 49. CD vs. FWD and CTD Crack Growth

any retardation in the earlier portion of crack growth as shown in Figure 50.

Figure 51 shows the Specimen 16 C-SCANs for 0, 45,010, and 79,188 cycles

corresponding to crack lengths of 25.723 mm (1.0127 inches), 50.198 mm (1.9763 inches)

and 75.396 mm (2.96835 inches). The 0 cycle C-SCAN shows the CD configuration with

dimensions shown in Figure 46. At 45,010 cycles, the intentional center disbond did not

show any growth, however, slight cyclic disbonding out to the patch edges was evident.

Again, cyclic disbonding up to this point had an insignificant effect on the crack growth

rate and repaired stress intensity factor. Not until the crack tips had extended well beyond

Table 15. da/dN for CD, FWD and CTD Specimens

Specimen	Configuration	da/dN (mm/cycle)
4	FWD	0.0005528
5	FWD	0.00064977
6	CTD	0.00043336
7	CTD	0.00041077
16	CD	0.000536089
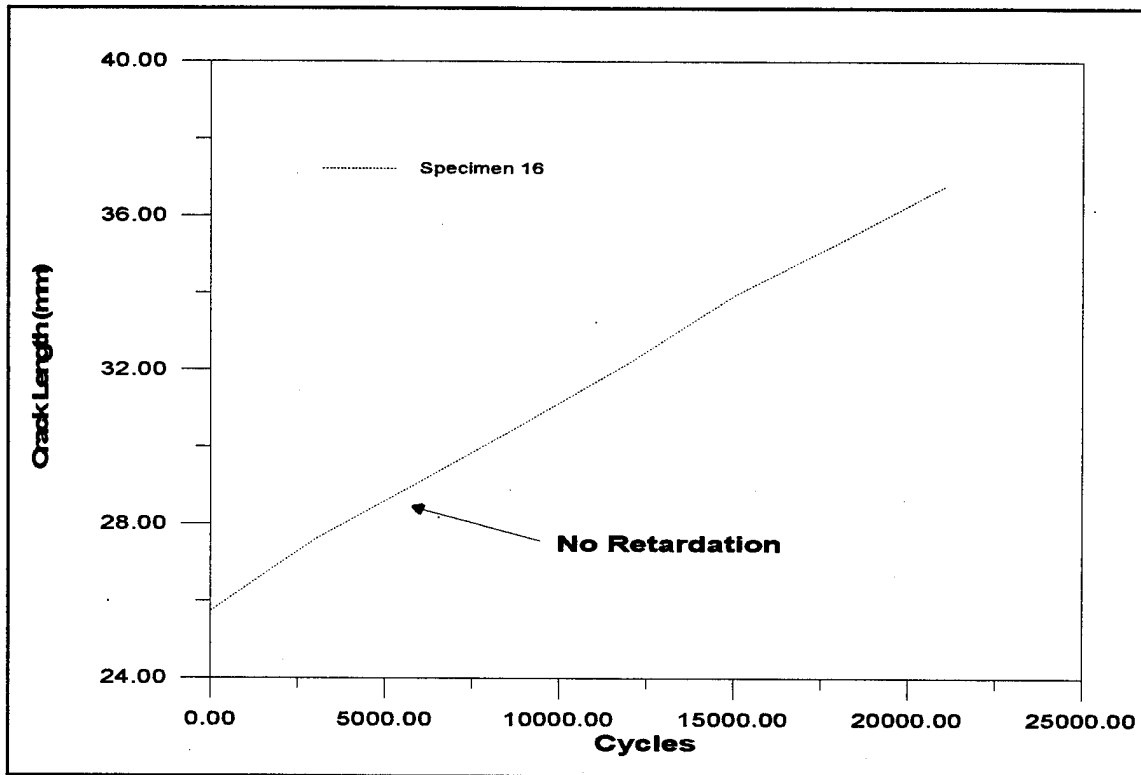
Figure 50. CD Retardation of Crack Growth

Specimen 16 (CD)
0 Cycles

Specimen 16 (CD)
45,010 Cycles

Specimen 16 (CD)
79,188 Cycles

Figure 51. CD C-SCANs

the patch edges did cyclic disbonding become more of a factor. Again, as with all the other previous disbond configurations, the bondline of the repair proved to be damage tolerant in accordance with Hart-Smith's (22) observations of thin metallic structures.

The CD specimen failed by the patch failure mode as shown in Figure 28 and Appendix A.

Effects of Disbond Size. This subsection is divided into two parts: (1) full width disbond (FWD) size effects; and (2) center disbond (CD) size effects. The size effects in these two parts differ by varying the disbond size relative to the x and y-directions as shown in Figure 52. FWD specimens demonstrate y-direction effects and CD specimens
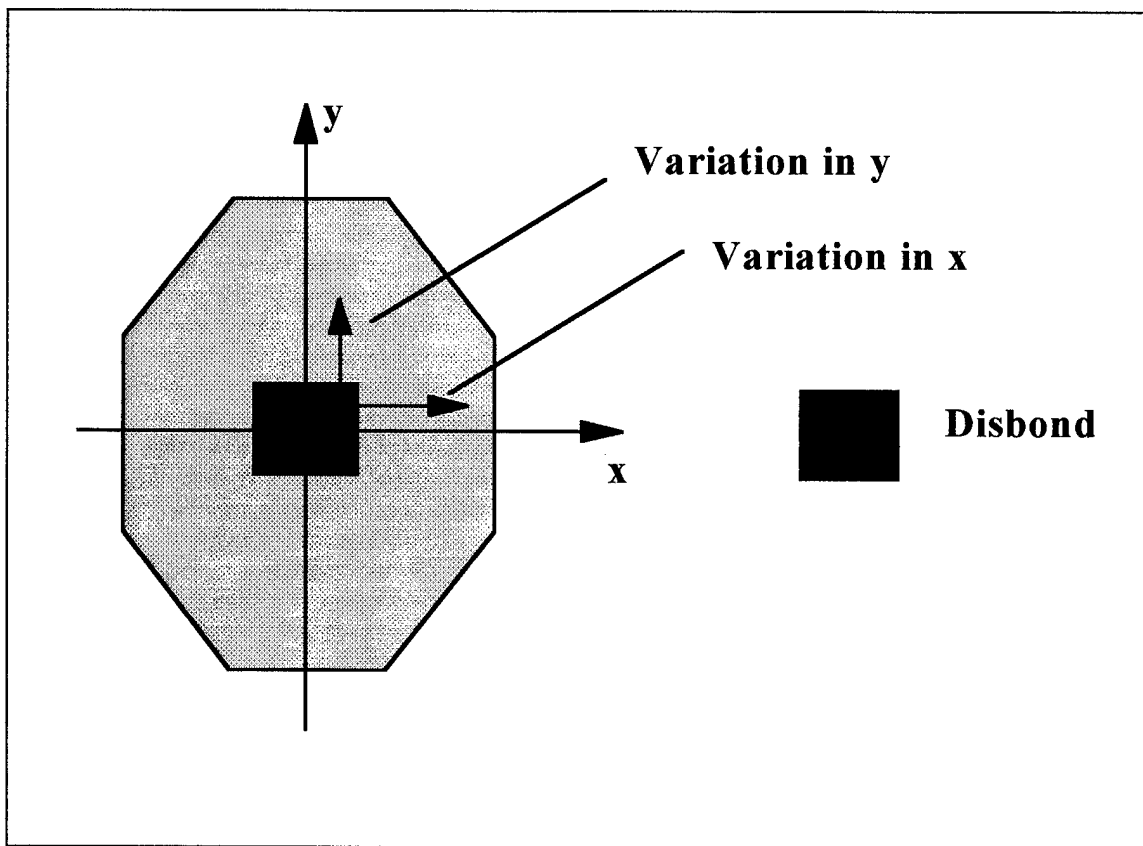
Figure 52. Disbond Size Variation

demonstrate x-direction effects.

Full Width Disbond Size Effects. Four FWD specimens, Specimens 4, 5, 11 and 14, were investigated for disbond size effects. The specimens and their disbond sizes with respect to the total bond area of 2822 mm^2 are shown in Table 16. The dimensions of the three variations of FWD size are shown in Figure 53. The fatigue lives of the FWD specimens are shown in Table 17 with the baseline and the two CBP specimens. The average fatigue life of Specimens 4 and 5 was 71 % of the CBP average of 119,320 cycles, a significant reduction in total life. Specimen 11 was 82 % of the CBP average life and Specimen 14 was 96 % of the CBP average life. This clearly shows that as the area of disbond increased in the y-direction (perpendicular to the crack), the fatigue life decreased.

Figure 54 shows the crack growth curves for the four FWD configurations and the two CBP specimens. The crack growth rates for all the FWD specimens were constant within the patch, indicating a constant repaired stress intensity factor range, ΔK_R. Outside of the patch, all the FWD specimens demonstrated similar parabolic trends, however, the CBP specimens exhibited a much more abrupt transition to parabolic growth as the crack grew further from the patch edges for similar crack lengths. This difference was due to the continuous cyclic disbonding that occurred about the crack within the CBP specimens that is shown in Figure 27, especially when the crack had grown outside the patch edges. As a result the repaired stress intensity factor range, ΔK_R, increased causing a greater change in crack growth. In comparison, the FWD specimens did not show an increase in the size of the intentional disbond, to be discussed later, which resulted in a more slowly

Table 16. FWD Sizes

Specimen	Configuration	Disbond Size (mm²)	Disbond % of Total Bond Area
4	FWD	600	21.3
5	FWD	600	21.3
11	FWD	300	10.6
14	FWD	150	5.3
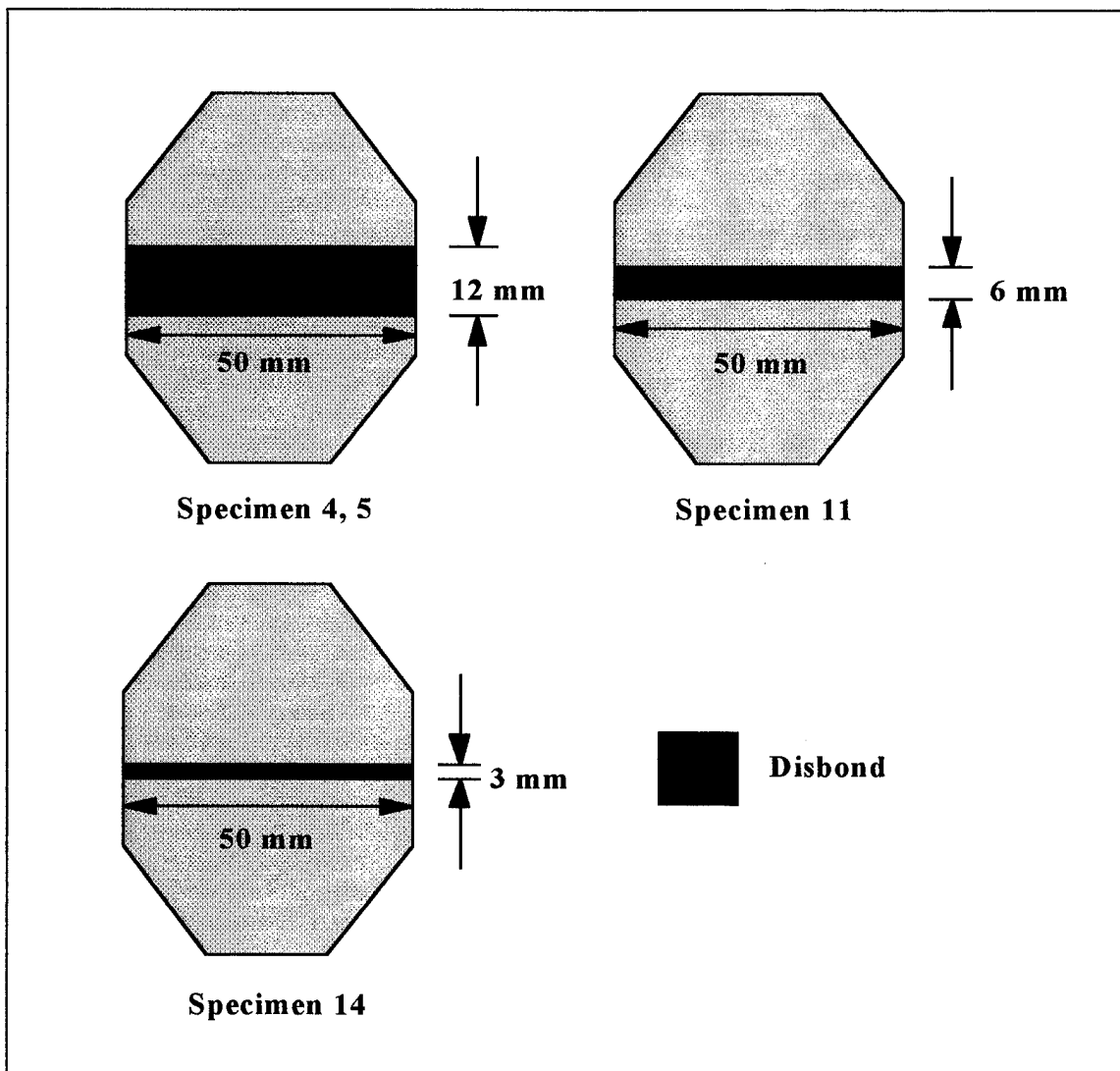
Figure 53. FWD Configuration Dimensions

Table 17. FWD Configuration Fatigue Lives

Specimen	Configuration	Cycles to Failure
1	Baseline (No Patch)	10,633
4	FWD	86,995
5	FWD	82,324
11	FWD	97,278
14	FWD	114,423
20	CBP	118,316
21	CBP	120,325
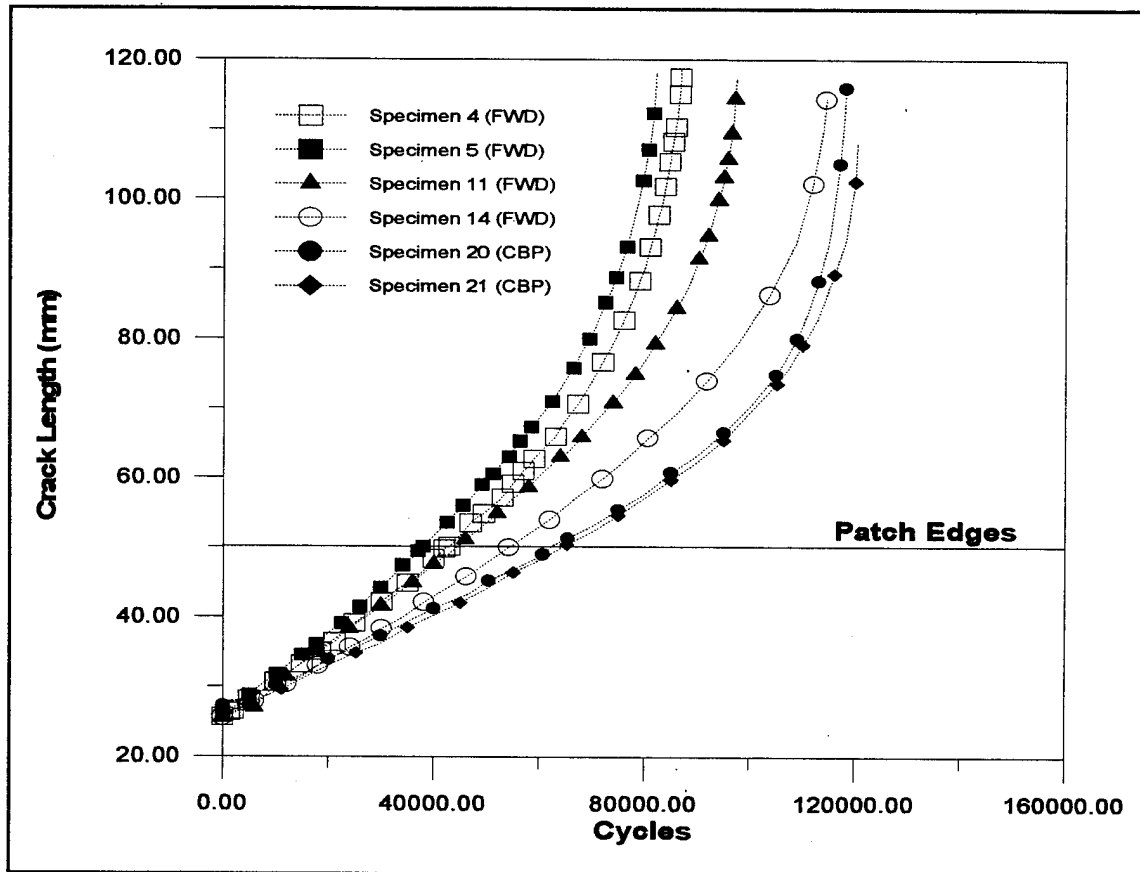
Figure 54. FWD vs. CBP Crack Growth

increasing repaired stress intensity factor range, ΔK_R, outside the patch. This led to the

less abrupt change in crack growth outside the patch edges. The average crack growth

rates within the patch for the three FWD size configurations and the CBP specimens are

shown in Table 18. The crack growth data in Table 18 was computed using the three-

point least squares method (37). Examining Table 18, it is evident that increasing the

disbond size perpendicular to the crack faces decreased the patch efficiency, i.e. the crack

Table 18. da/dN for FWD Configurations and CBP Specimens

Specimen	Configuration	da/dN (mm/cycle)
4	FWD	0.00055280
5	FWD	0.00064977
11	FWD	0.00056828
14	FWD	0.00044522
20	CBP	0.00036265
21	CBP	0.00036580

growth rate within the patch increased. This agrees with Baker's (6) studies of FWD

specimens. The average crack growth rate of Specimen 4 and 5, with a 21.3 % disbond,

was 1.65 times that for the CBP specimens. Specimen 11, with a 10.6 % disbond, had a

crack growth rate that was 1.56 times the CBP average and Specimen 14, with a 5.3 %

disbond, yielded a crack growth rate that was only 1.22 times that of the CBP specimens.

It is clear that displacing the point of load transfer further away from the crack , as in

Figure 32, reduced the amount of load that can be transferred out of the damaged

aluminum panel into the patch repair, thus reducing the patch efficiency. Also, crack

bridging is reduced.

Figure 55 shows the C-SCANs for Specimens 11 (with a 10.6 % area disbond) and

Specimen 11 (FWD)
0 Cycles

Specimen 14 (FWD)
0 Cycles

Specimen 11 (FWD)
40,004 Cycles

Specimen 14 (FWD)
54,224 Cycles

Specimen 11 (FWD)
78,201 Cycles

Specimen 14 (FWD)
75,600 Cycles
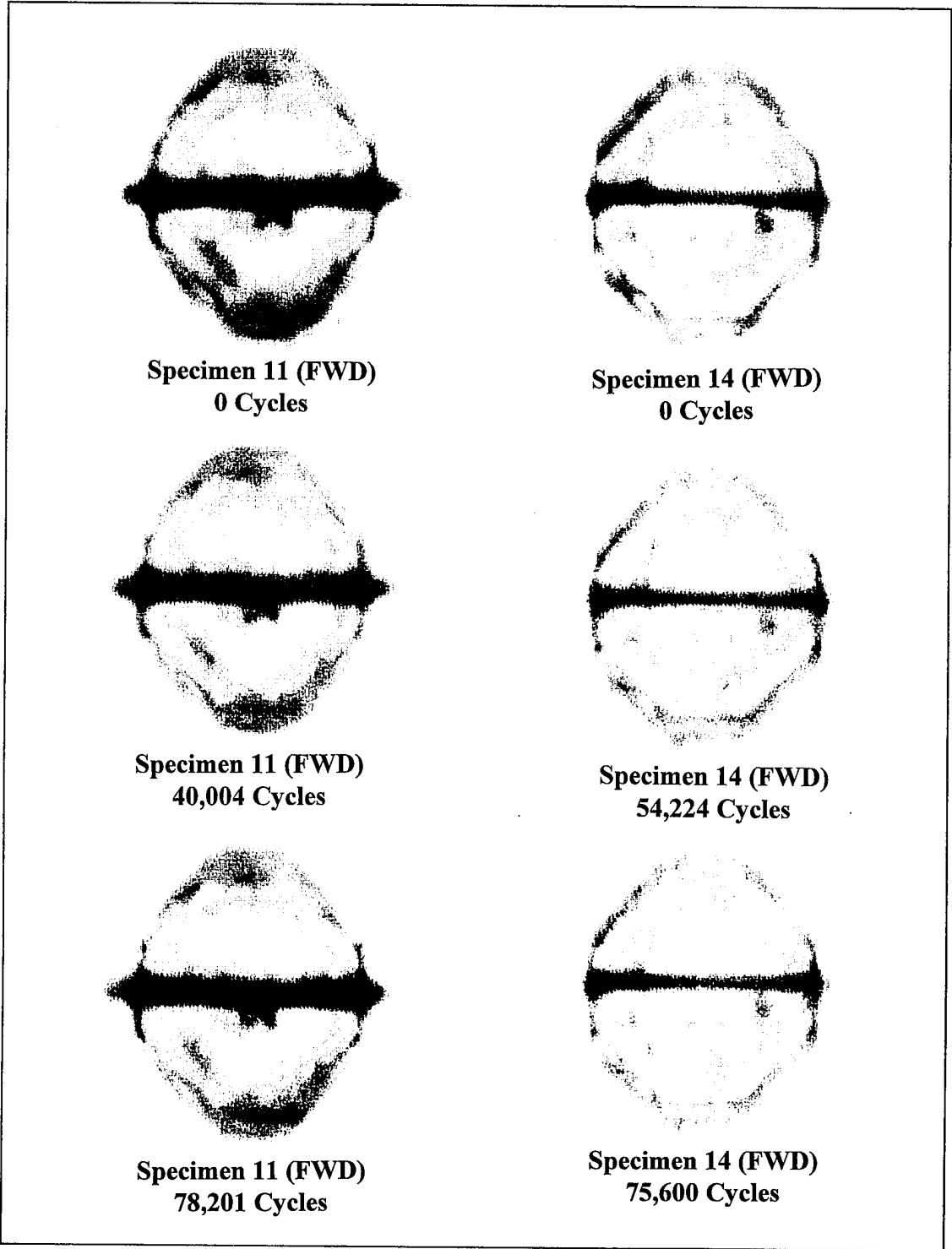
Figure 55. Specimen 11 and 14 C-SCANs

14 (with a 5.3 % area disbond). C-SCANs for Specimen 4 (with a 21.3 % area disbond), demonstrating similar behavior as of Specimen 5, are shown in Figure 34. The three C-SCANs of Specimen 11 are for 0, 40,004 and 78,201 cycles corresponding to crack lengths of 25.439 mm (1.00155 inches), 47.575 mm (1.87305 inches) and 74.88 mm (2.94803 inches). The three C-SCANs of Specimen 14 are for 0, 54,224 and 75,600 cycles corresponding to crack lengths of 25.588 mm (1.0074 inches), 49.957 mm (1.9668 inches) and 62.090 mm (2.4445 inches). No intentional disbond growth was evident in agreement with Baker's (6) results and Hart-Smith's (22) observations. The bondline was damage tolerant of the disbonds, however, they still had a noticeable effect on the crack growth.

As with all prior specimens, Specimens 11 and 14 showed no retardation and failed by the patch failure mode as shown in Figure 28 and Appendix A.

Center Disbond Size Effects. Three specimens, Specimens 2, 16 and 17, with a center disbond were investigated for disbond size effects. The specimens and their disbond sizes are shown in Table 19. Specimen 2 was the first specimen fabricated in this study which resulted in a disbond around the crack caused by trapped air in the bondline,

Table 19. CD Sizes

Specimen	Configuration	Disbond Size (mm^2)	Disbond % of Total Bond Area
2	CD	≈74	≈2.6
16	CD	312	11
17	CD	144	5.1

95

therefore, the disbond size shown in Table 19 is an estimate. This error was corrected for in the remaining specimens. The dimensions of the intentional disbonds along with the general shape and dimensions of the disbond in Specimen 2 are shown in Figure 56. The fatigue lives of these CD specimens along with the baseline and two CBP specimens are shown in Table 20. The fatigue life of Specimen 2 was 94 % of the CBP average of 119,320 cycles. Specimen 16 was 78 % of the CBP average and Specimen 17 was 98 %
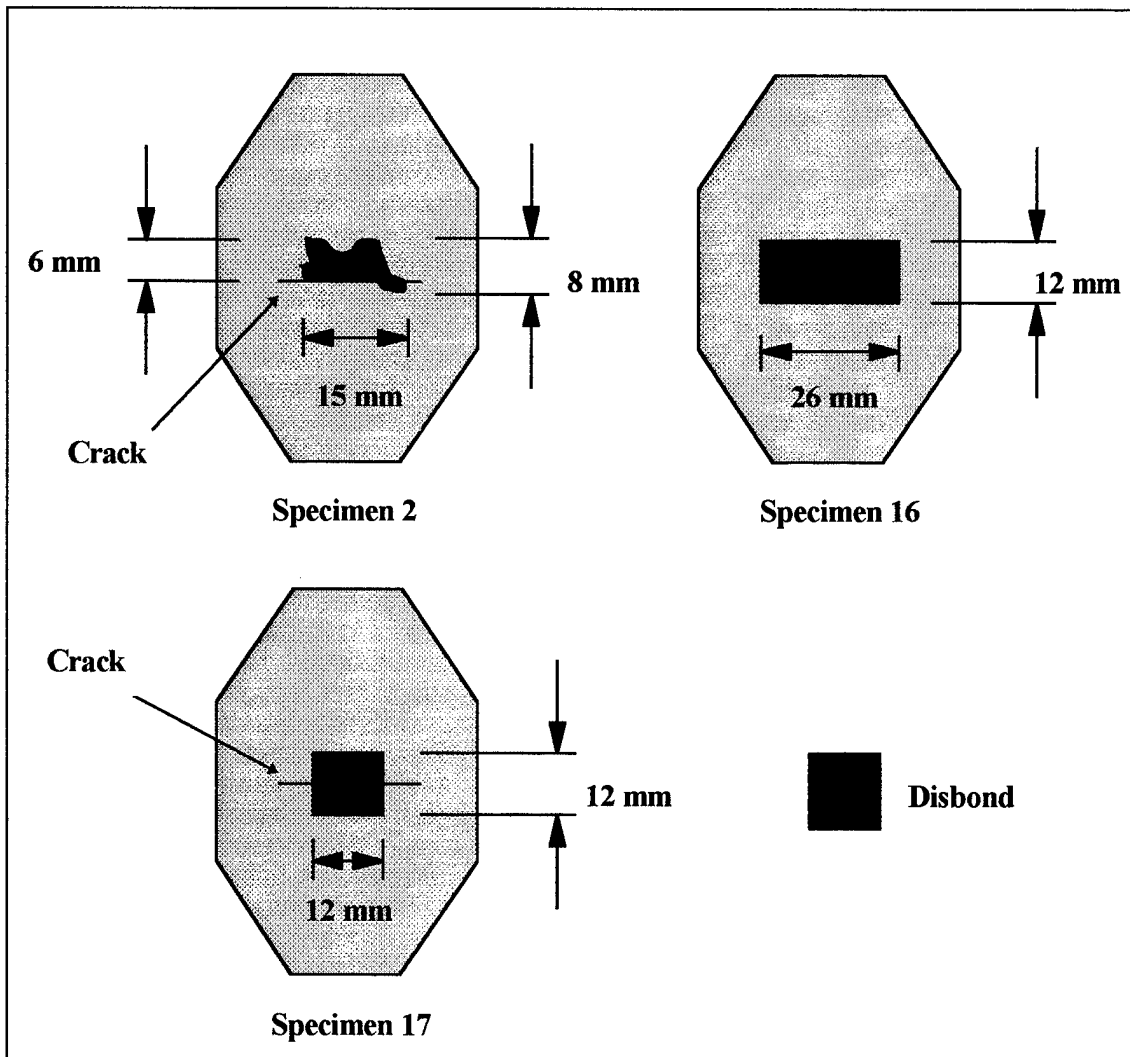
Figure 56. CD Configuration Dimensions

Table 20. CD Configuration Fatigue Lives

Specimen	Configuration	Cycles to Failure
1	Baseline (No Patch)	10,633
2	CD	112,613
16	CD	92,624
17	CD	116,817
20	CBP	118,316
21	CBP	120,325

of the average CBP life. This again shows that the fatigue life, in general, decreased with the size of center disbond.

Figure 57 shows the crack growth curves for the three CD configurations and the two CBP specimens. The crack growth rates were all constant within the patch repair. Crack growth outside the patch for the smaller CD cases, Specimen 2 and 17, followed a similar trend as the CBP specimens. This occurred because the majority of the crack was completely bonded and the cyclic disbonding had a greater opportunity to occur between the CD and the patch edges. The intentional center disbonds dominated the crack growth rate within the repair, however, outside the repair the crack growth rate was dominated by cyclic disbonding. The smaller disbonds allowed more cyclic disbonding around the crack faces during fatigue, that is why they possess the same parabolic trend as the CBP specimens outside the patch edges, i.e. the cyclic disbonding increased the repaired stress intensity factor range, ΔK_R, which resulted in an increasing crack growth rate outside the patch. This cyclic disbonding is shown later. The average crack growth rates within the patch, based on the three-point least squares method (37), for the three CD specimens and the two CBP specimens are compared in Table 21. The crack growth rate of Specimen 2,
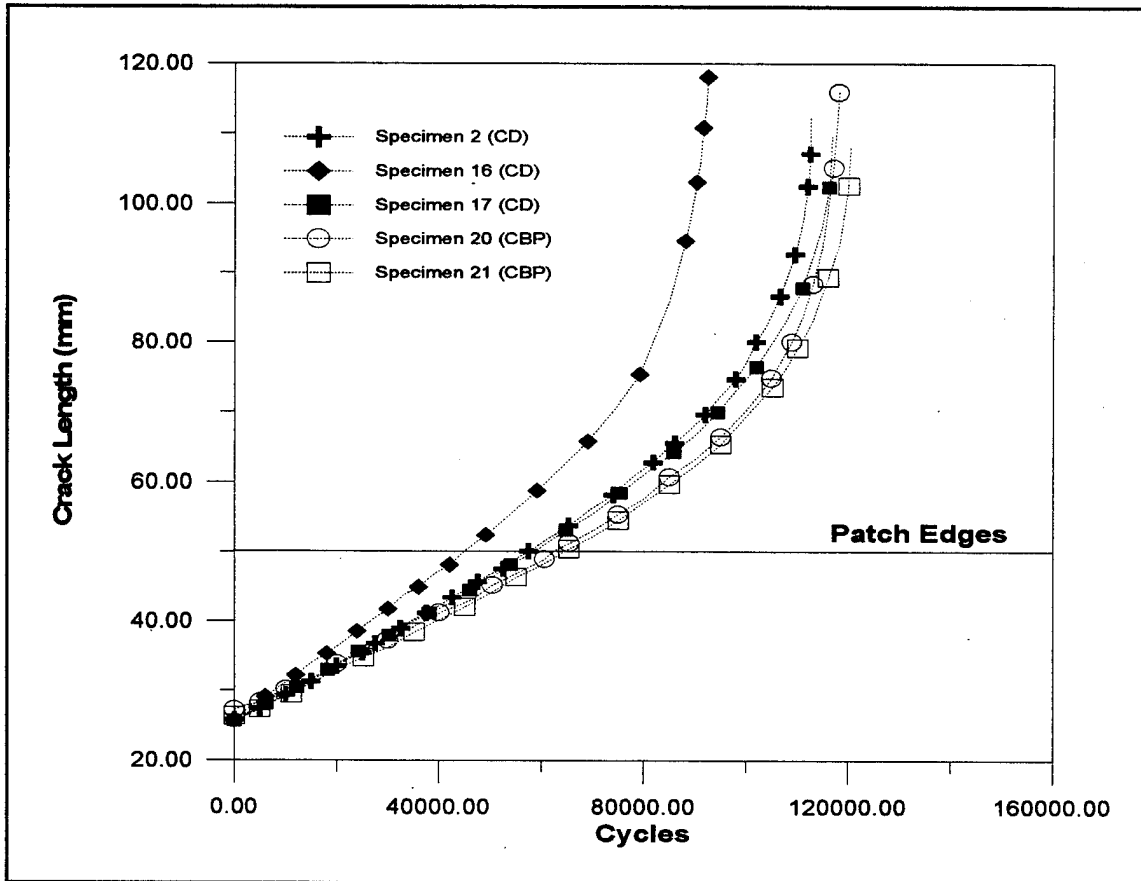
Figure 57. CD vs. CBP Crack Growth

Table 21. da/dN for CD Configurations and CBP Specimens

Specimen	Configuration	da/dN (mm/cycle)
2	CD	0.00043029
16	CD	0.00053609
17	CD	0.00041613
20	CBP	0.00036265
21	CBP	0.00036580

98

with a 2.6 % disbond, was 1.18 times the CBP average within the patch. Specimen 16, with a 11 % disbond, yielded a crack growth rate that was 1.47 times the CBP average and Specimen 17, with a 5.1 % disbond, had a crack growth rate that was 1.14 times the CBP average within the patch. Although Specimen 2 had a smaller disbond than Specimen 17, it yielded a slightly greater crack growth rate within the patch because it spanned a greater portion of the crack. Based on this single comparison, a disbond that covers a greater region in the x-direction as compared to the y-direction, as shown in Figure 52, will have more impact on the overall patching efficiency. This also helps to explain why cyclic disbonding about the crack, although not significant in the y-direction, had an impact on patching efficiency. Therefore, combining significant x-direction and y-direction disbonding, as with the FWD specimens, is a worst case scenario.

Figure 58 shows the C-SCANs for Specimens 2 (with ≈2.6 % area disbond) and 17 (with a 5.1 % area disbond). C-SCANs for Specimen 16 (with a 11 % area disbond) can be found in Figure 51. The three Specimen 2 C-SCANs are for 0, 57,522 and 99,739 cycles corresponding to crack lengths of 25.794 mm (1.0155 inches), 50.11 mm (1.97285 inches) and 76.878 mm (3.0267 inches). The Specimen 17 C-SCANs are for 0, 58,483 and 94,516 cycles corresponding to crack lengths of 25.690 mm (1.01145 inches), 49.985 mm (1.9679 inches) and 69.985 mm (2.7553 inches). No pre-existing disbond growth occurred, once again in agreement with Baker's (6) results and Hart-Smith's (22) findings, however, cyclic disbonding, especially for crack growth outside the patch, was evident.

As with all prior specimens, Specimens 2 and 17 exhibited no retardation and failed by the patch failure mode as shown in Figure 28 and Appendix A.

Specimen 2 (CD)
0 Cycles

Specimen 17 (CD)
0 Cycles

Specimen 2 (CD)
57,522 Cycles

Specimen 17 (CD)
58,483 Cycles

Specimen 2 (CD)
99,739 Cycles

Specimen 17 (CD)
94,516 Cycles
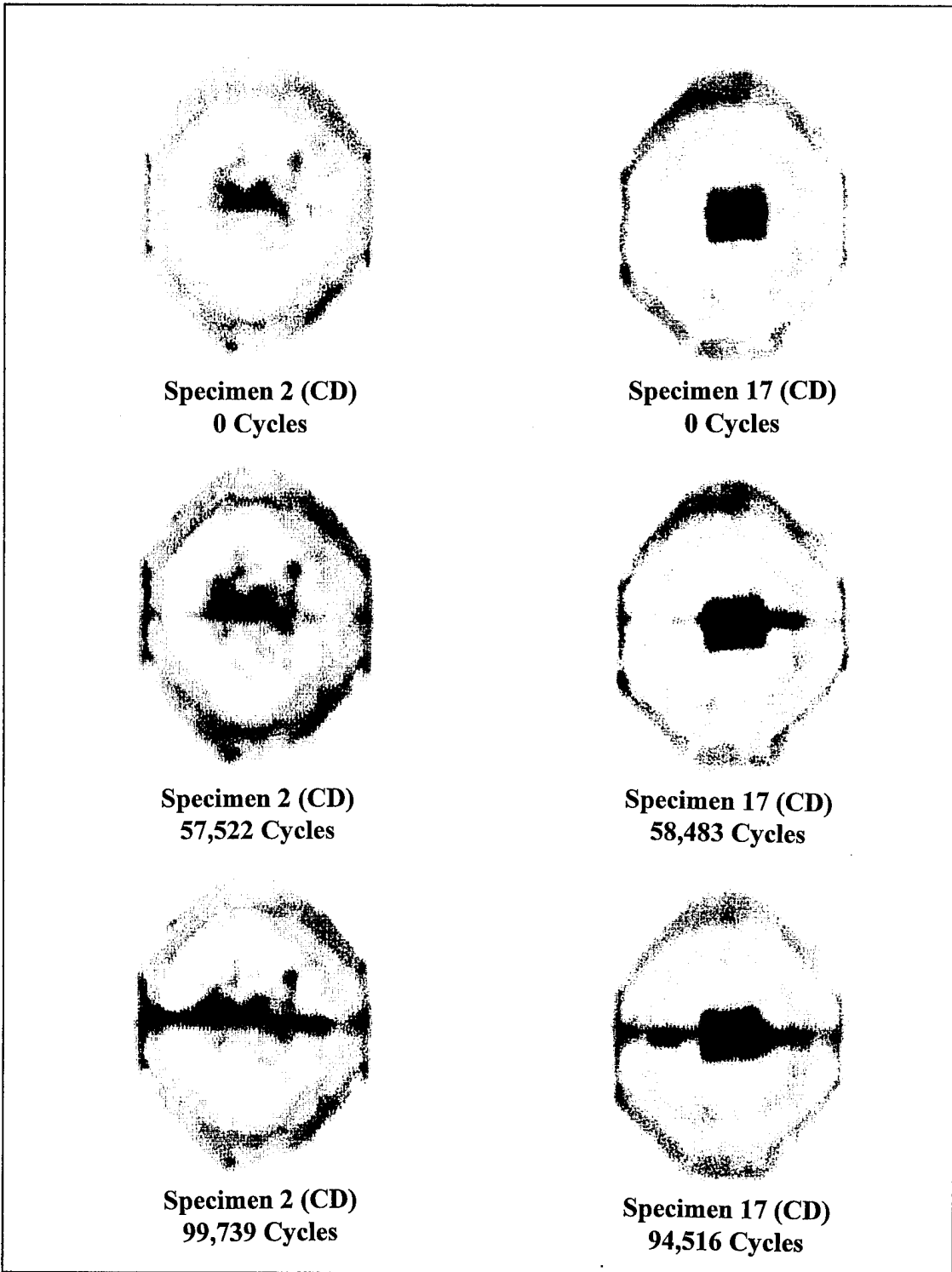
Figure 58. Specimen 2 and 17 C-SCANs

Effects of Stress Level

Three patch configurations, CBP, FWD and ED1, were investigated with peak stress levels of 100 MPa and 120 MPa. It is expected that a higher stress level will lead to a shorter fatigue life, however, the understanding of the damage mechanisms which cause the patch repair to fail sooner is more important. If the repair is overdesigned with a stiffness ratio, $E_R t_R / E_P t_P$, well above 1 and a very large bond area, increasing the peak stress from 100 MPa to 120 MPa may be insignificant to the performance of the repair. However, with a repair that is just within design practices, such as the one investigated in this effort, an extra 20 MPa of peak load may have a noticeable effect on crack and disbond growth. The summary of fatigue lives for the CBP, FWD and ED1 specimens along with the baseline specimens tested at stress levels of 100 MPa and 120 MPa are shown in Table 22. All disbonds were approximately 20 % of the total bond area.

Table 22. 100 vs. 120 MPa Fatigue Lives

Specimen	Configuration	Peak Stress (MPa)	Cycles to Failure
1	Baseline (No Patch)	120	10,633
18	Baseline (No Patch)	100	23,158
4	FWD	120	86,995
5	FWD	120	82,324
13	FWD	100	124,647
20	CBP	120	118,316
21	CBP	120	120,325
10	CBP	100	201,382
8	ED1	120	139,013
9	ED1	120	135,942
15	ED1	100	207,752
22	ED1	100	171,912

The crack length versus cycles curves for the CBP, FWD and ED1 specimens along with the baseline specimens ,with no patches, for both 100 and 120 MPa stress levels are shown in Figures 59, 60, and 61, respectively. Also, the corresponding crack growth rate versus crack length curves are shown in Figures 62, 63, and 64. It is evident from these figures that the crack growth rate was constant within the patch repair for all three configurations at both peak stress levels. Figure 62 shows that the 100 MPa CBP specimen crack growth rate remained constant long after the 120 MPa CBP specimen crack growth rates had shown an increasing trend. This behavior was the result of a lower repaired stress intensity factor in the 100 MPa CBP specimen, as well as, a resistance to cyclic disbonding caused by a smaller adhesive shear strain. The 100 MPa and 120 MPa FWD specimen crack growth rates exhibited similar trends at the same crack lengths as shown in Figure 63. In other words, the 100 MPa FWD crack growth rate did not remain constant beyond that of the 120 MPa FWD specimen because both stress level FWD specimens maintained the same pre-existing level of damage as compared to the CBP specimens which developed different levels of damage over time, resulting in different trends at the same crack length. As with the CBP specimens, the reduced crack growth rate of the 100 MPa ED1 specimens as compared to the 120 MPa ED1 specimens was the result of a lower repaired stress intensity factor and a resistance to cyclic disbonding. These characteristics will become clear upon evaluation of the C-SCANs.

The repaired stress intensity factor, K_R, the maximum adhesive shear strain, γ_A^{max}, and the crack growth rates within the patch are presented in Table 23. K_R and γ_A^{max} are based on the Rose model.
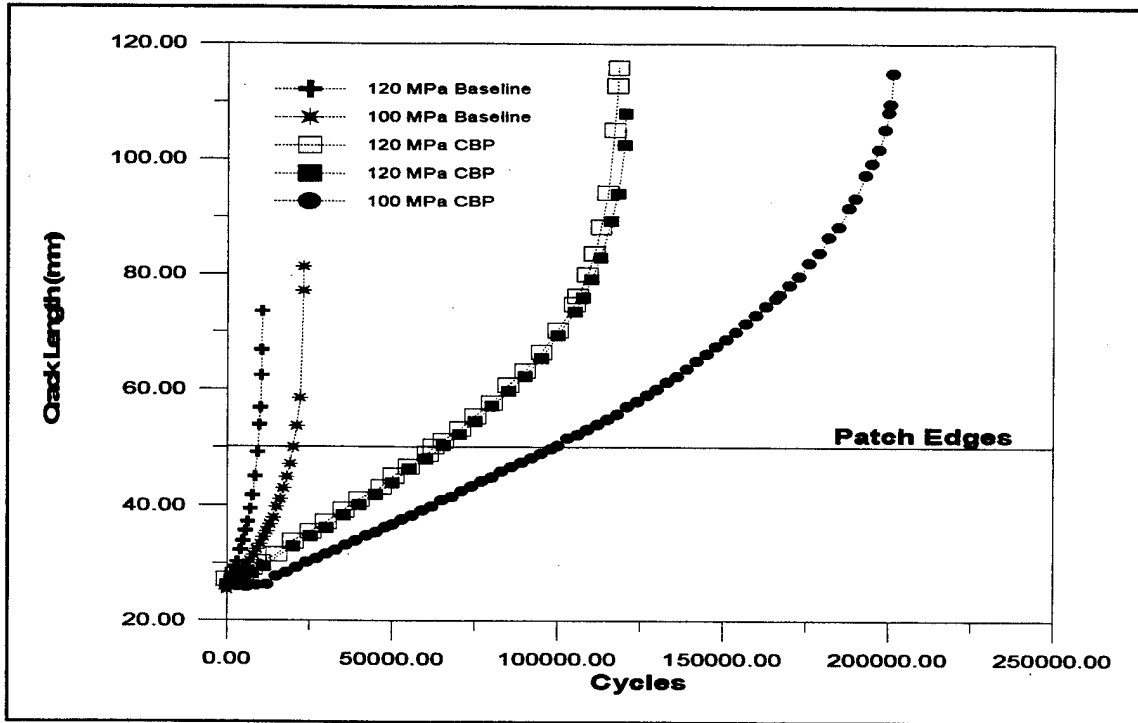
Figure 59. 100 vs. 120 MPa Baseline and CBP Crack Growth
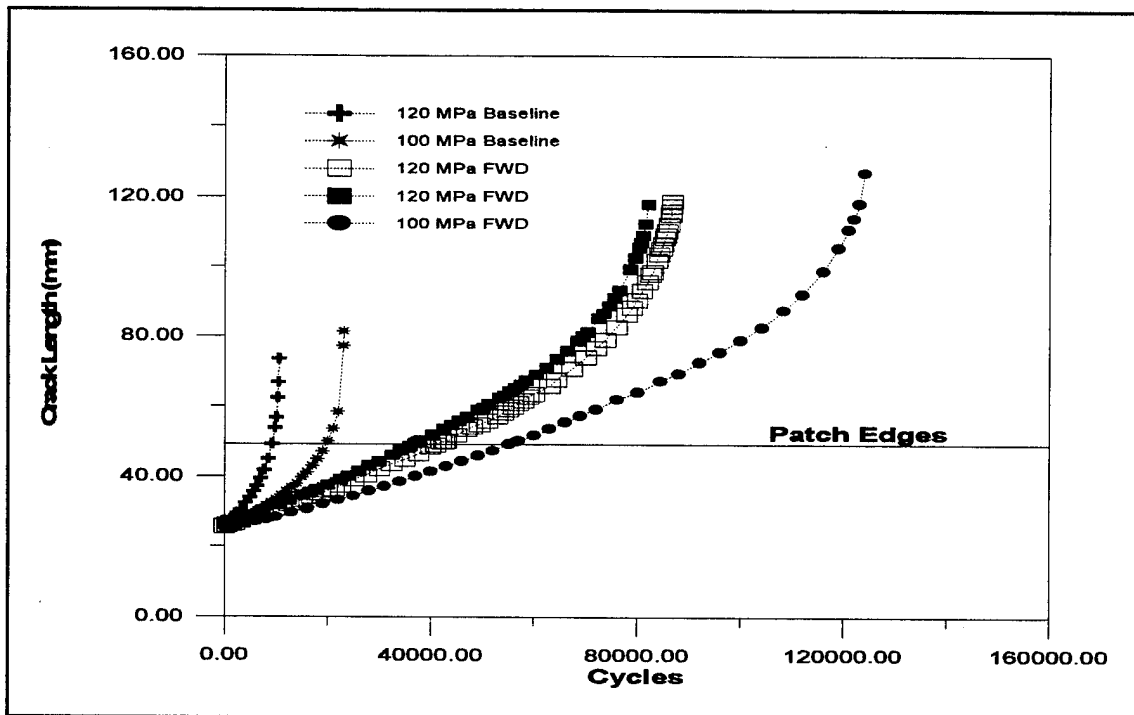
Figure 60. 100 vs. 120 MPa Baseline and FWD Crack Growth
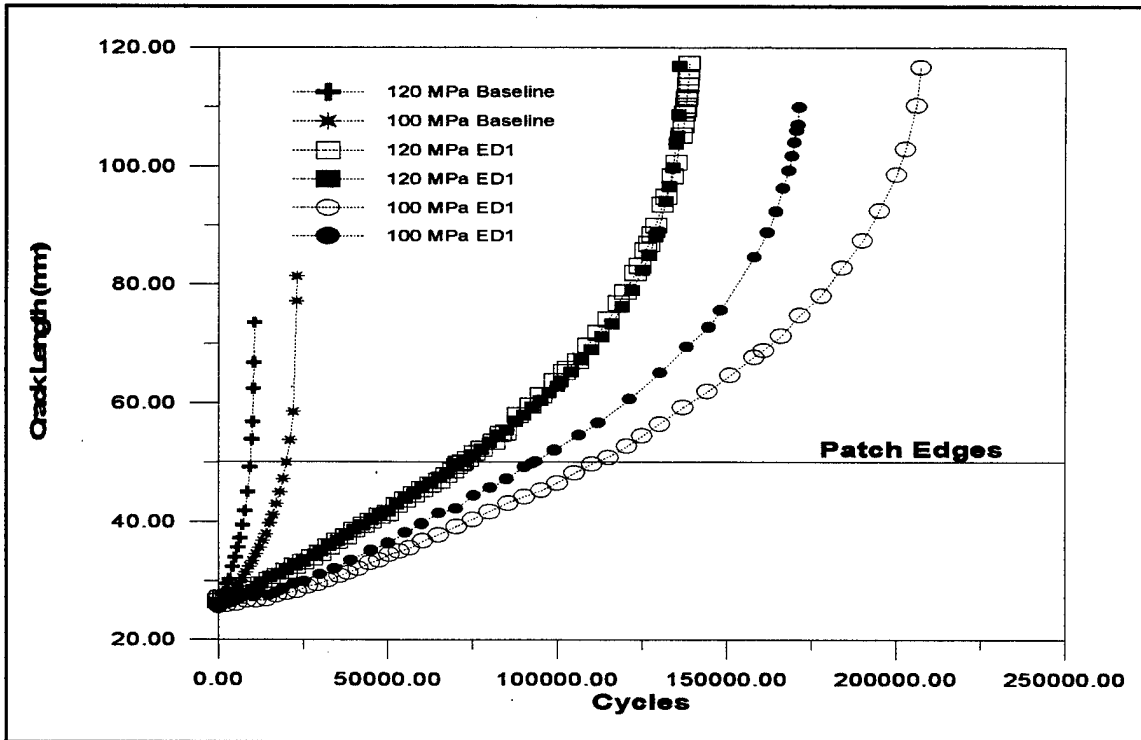
Figure 61. 100 vs. 120 Baseline and ED1 Crack Growth
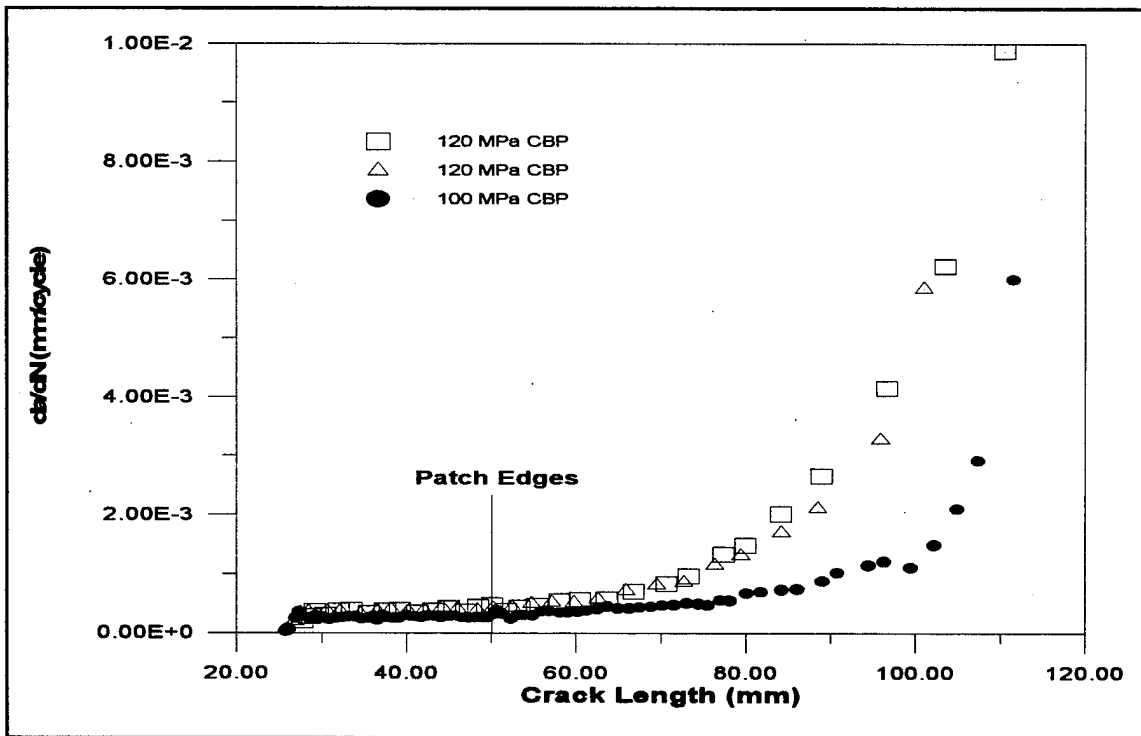
Figure 62. da/dN vs. Crack Length for 100 and 120 MPa CBP Specimens
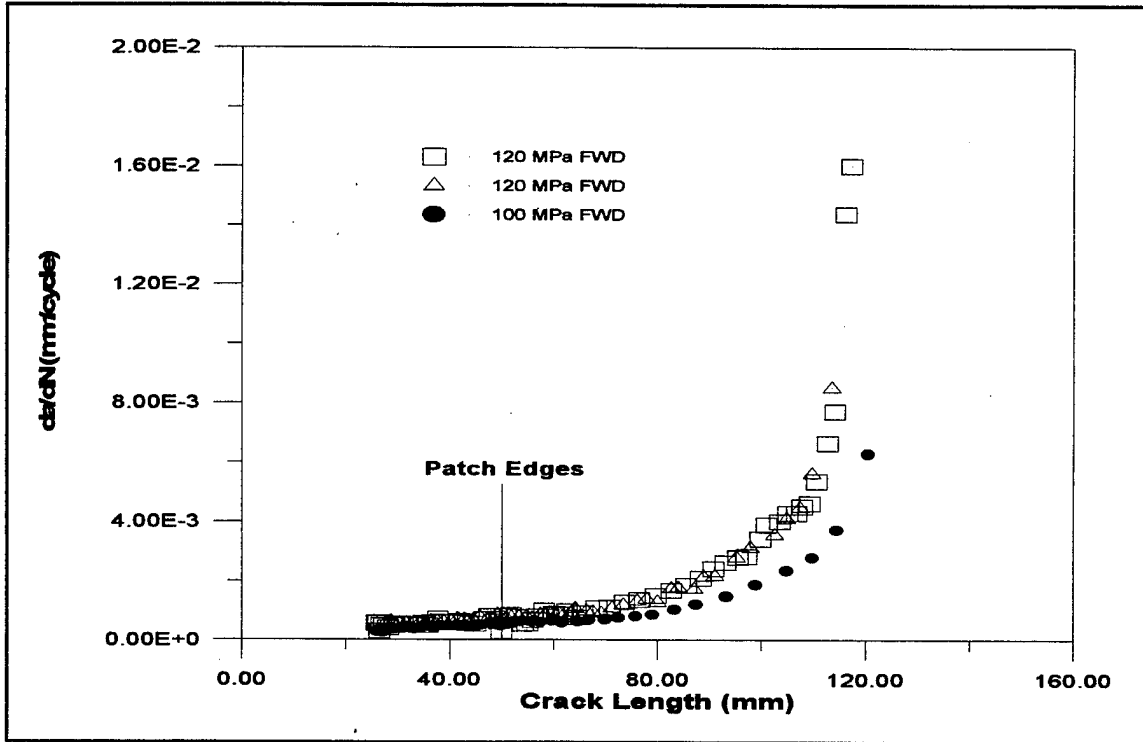
Figure 63. da/dN vs. Crack Length for 100 and 120 MPa FWD Specimens
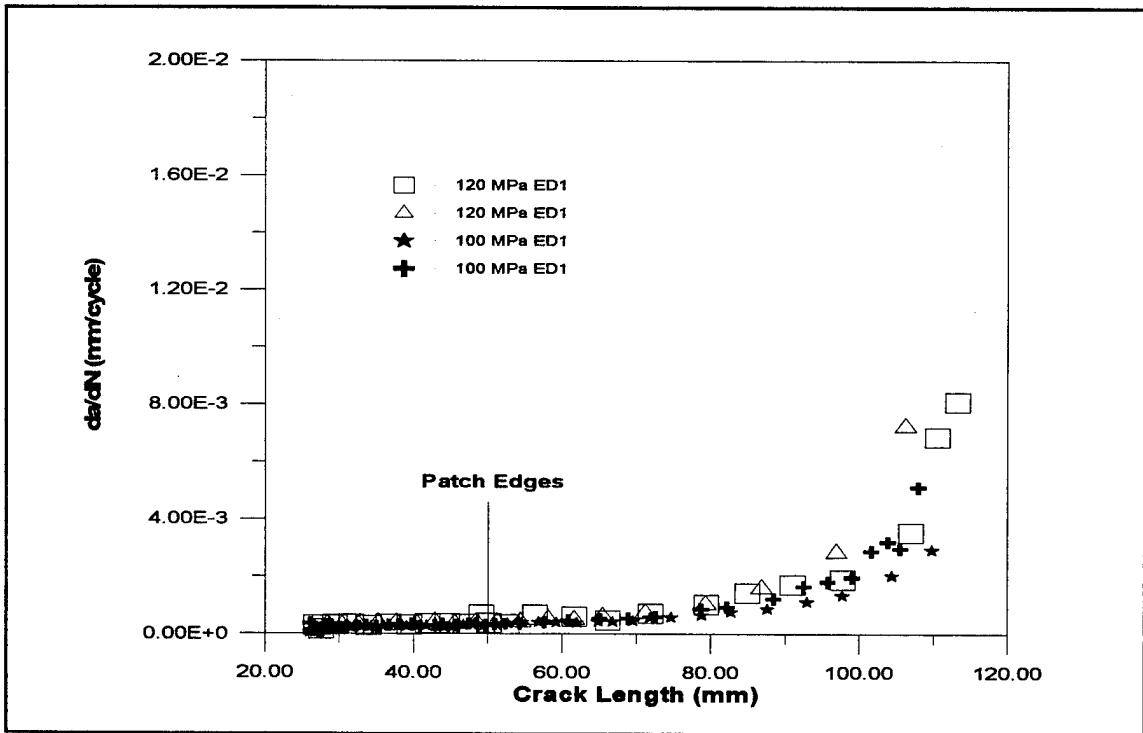
Figure 64. da/dN vs. Crack Length for 100 and 120 MPa ED1 Specimens

Table 23. 100 vs. 120 MPa K_R, γ_A^{max}, and da/dN

Specimen	Configuration	Peak Stress (MPa)	K_R (MPa√m)	γ_A^{max} (%)	da/dN (mm/cycle)
4	FWD	120	NA*	NA*	0.00055280
5	FWD	120	NA*	NA*	0.00064977
13	FWD	100	NA*	NA*	0.00043233
20	CBP	120	5.43	5.1	0.00036265
21	CBP	120	5.42	5.1	0.00036580
10	CBP	100	4.51	4.3	0.00024812
8	ED1	120	4.82	4.6	0.00032444
9	ED1	120	4.82	4.6	0.00033952
15	ED1	100	4.01	3.8	0.00020761
22	ED1	100	4.01	3.8	0.00026275

*Rose model does not apply to FWD

The crack growth equation

$$da/dN = C(\Delta K)^n \tag{16}$$

proposed by Paris (9), is associated with the linear portion of the log-log plot of da/dN versus ΔK, where C is a constant and n is the slope of the log-log plot. Assuming that this equation applies for both patched and unpatched specimens, it is possible to estimate the slope, n, for each case. The ratio of the 120 MPa tests to the 100 MPa tests, using the fact that $\Delta K \propto \Delta \sigma$, results in

$$\frac{(da/dN)_{120MPa}}{(da/dN)_{100MPa}} = \left(\frac{\Delta \sigma_{120MPa}}{\Delta \sigma_{100MPa}}\right)^n \tag{17}$$

Taking the logarithm of both sides of Equation (17) we can solve for n such that

$$n = \frac{\log\left[(da/dN)_{120MPa} / (da/dN)_{100MPa}\right]}{\log\left[\Delta \sigma_{120MPa} / \Delta \sigma_{100MPa}\right]} \tag{18}$$

The average da/dN ratios for each patch configuration along with the estimated average n values are listed in Table 24. On average, the n values for the patched specimens are

Table 24. Estimated n Values for the Paris Law

Configuration	$(da/dN)_{120\,MPa}$ / $(da/dN)_{100\,MPa}$	n
CBP	1.47	2.11
FWD	1.38	1.81
ED1	1.41	1.88

approximately 2 for the completely bonded patch and two configurations of disbonds. As expected this value is less than the average of 2.91 for the unpatched specimens. Looking at each specimen individually, for all three patch configurations, and not on an average basis, the values of n range from 1.16 to 2.7. This scatter suggests that more tests are required to obtain a better statistical estimate for n. However, Table 24 does suggest that the value of n is approximately the same for the patch, either with or without a disbond.

Figure 65 shows the representative C-SCANs for the CBP specimens, Specimen 10 (100 MPa) and Specimen 20 (120 MPa). The bondline behavior of Specimen 21 (120 MPa) mirrored that of Specimen 20. The C-SCANs of Specimen 10 are for 0, 100,003, 167,025 cycles which correspond to crack lengths of 25.7 mm (1.0122 inches), 50.271 mm (1.9792 inches) and 76.472 mm (3.0107 inches). The C-SCANs for Specimen 20 are for 0, 62,492, and 106,003 cycles which correspond to crack lengths of 27.238 mm (1.07235 inches), 50.221 mm (1.9772 inches) and 76.221 mm (3.00045 inches). The 0 cycle C-SCANs show no defects in either specimen. The second C-SCAN for each specimen corresponds to the point when the crack tips had reached the patch edges. At this point Specimen 10's bond is unaffected by the 100,003 cycles, however, Specimen 20

showed slight, but insignificant, cyclic disbonding. As a result, the crack growth rate, da/dN, was constant within the patch repair at both stress levels. The final C-SCAN corresponds to the point when the crack tips had exceeded the patch edges by approximately 12-13 mm on each side. At this point, Specimen 10 had just begun to show slight cyclic disbonding while Specimen 20 had suffered significant damage to its bondline, explaining the constant crack growth of Specimen 10 well beyond that of Specimen 20 outside the patch edges. The cyclic damage to Specimen 20's bondline increased the already greater repaired stress intensity factor resulting in the earlier increase in crack growth as compared to Specimen 10 for similar crack lengths as shown in Figure 62.

Figure 66 shows the C-SCANs for Specimen 4 and Specimen 13, tested at 120 MPa and 100 MPa, respectively. The bondline behavior of Specimen 5 (120 MPa) mirrored that of Specimen 4. The Specimen 4 C-SCANs are for 0, 43,018 and 72,030 cycles which correspond to crack lengths of 25.632 mm (1.00915 inches), 50.113 mm (1.97295 inches) and 76.68 mm (3.0189 inches). The Specimen 13 C-SCANs are for 0, 57,009 and 96,034 cycles which correspond to crack lengths of 25.796 mm (1.0156 inches), 50.219 mm (1.97715 inches) and 75.507 mm (2.9727 inches). As can be seen, none of the C-SCANs show growth of the original intentional disbond. This was consistent with Baker's (6) studies of intentional FWD specimens, as well as, the findings of Hart-Smith (22). This lack of disbond growth explains why the 100 MPa and 120 MPa specimen crack growth rates demonstrated similar trends at the same crack lengths, although not at the same rates.

Figure 67 shows the representative C-SCANs for Specimens 8, 15, and 22, tested

Specimen 10 (100 MPa)
0 Cycles

Specimen 20 (120 MPa)
0 Cycles

Specimen 10 (100 MPa)
100,003 Cycles

Specimen 20 (120 MPa)
62,492 Cycles

Specimen 10 (100 MPa)
167,025 Cycles

Specimen 20 (120 MPa)
106,003 Cycles
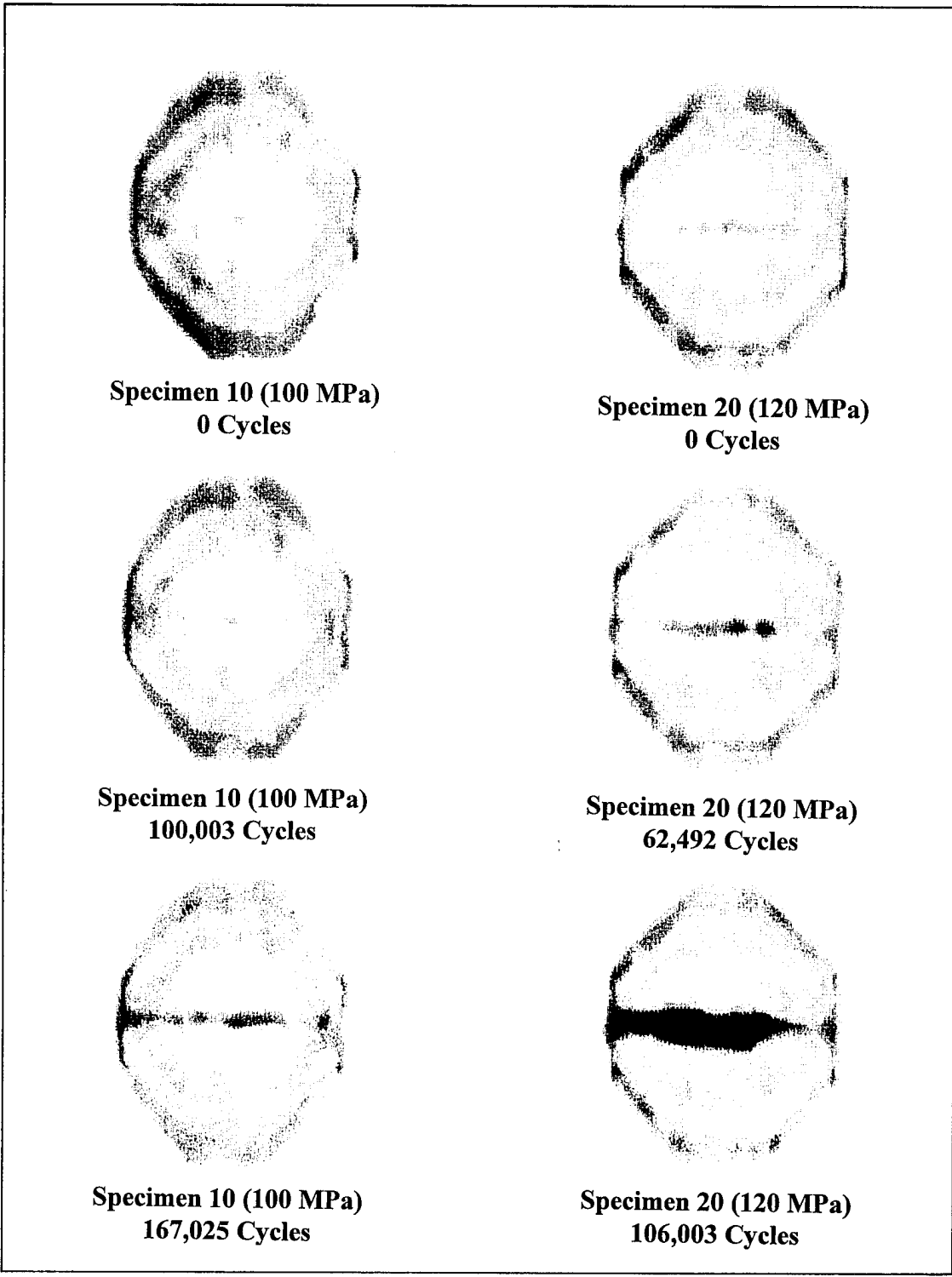
Figure 65. 100 vs. 120 MPa CBP C-SCANs

Specimen 4 (120 MPa)
0 Cycles

Specimen 13 (100 MPa)
0 Cycles

Specimen 4 (120 MPa)
43,018 Cycles

Specimen 13 (100 MPa)
57,009 Cycles

Specimen 4 (120 MPa)
72,030 Cycles

Specimen 13 (100 MPa)
96,034 Cycles
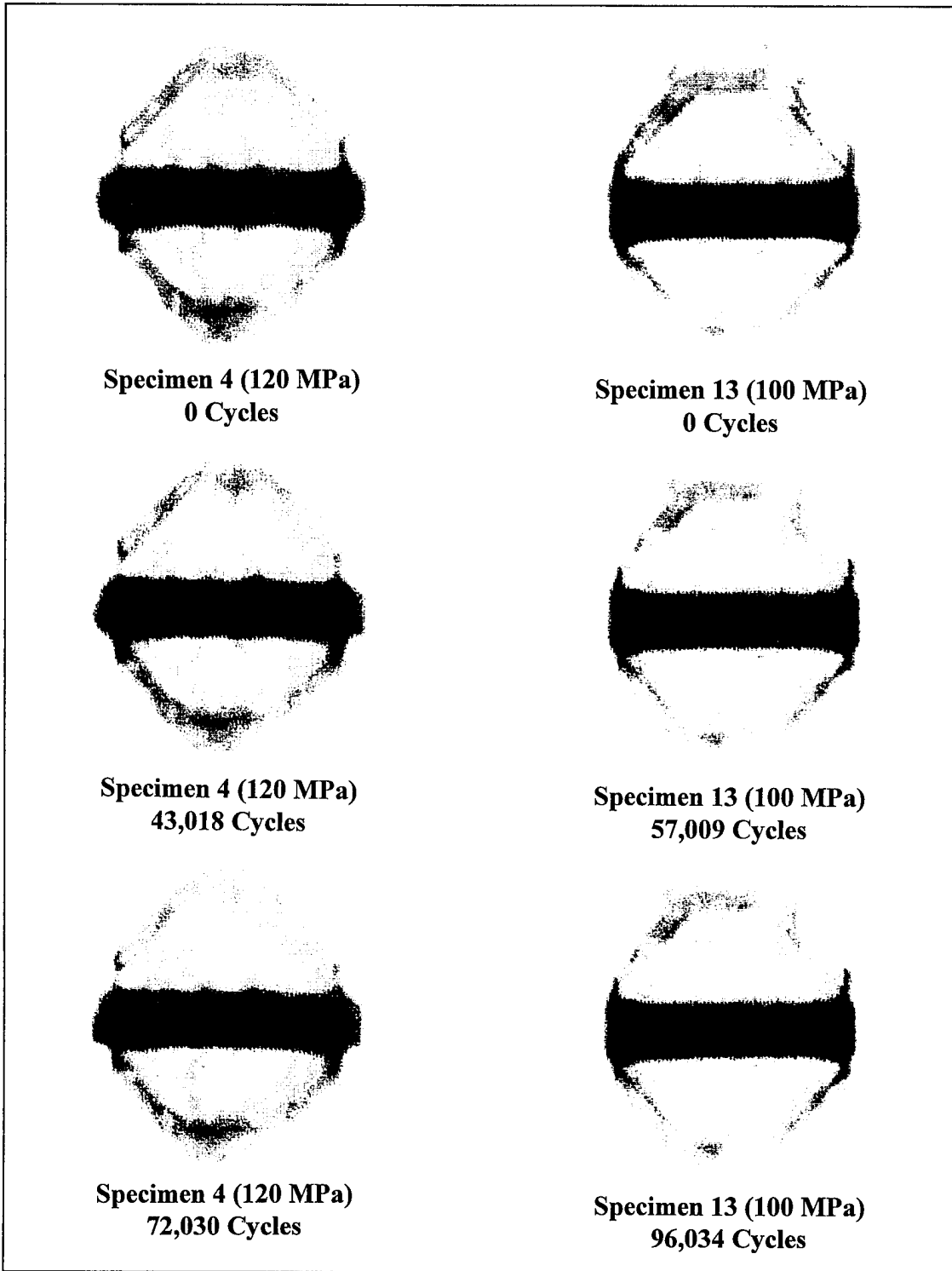
Figure 66. 100 vs. 120 MPa FWD C-SCANs

110

at 120 MPa, 100 MPa and 100 MPa, respectively. Specimen 9's (120 MPa) bondline behavior mirrored that of Specimen 8. The Specimen 8 C-SCANs are for 0, 72,013 and 118,076 cycles corresponding to crack lengths of 26.597 mm (1.0471 inches), 49.996 mm (1.96835 inches) and 76.902 mm (3.02 765 inches). The three Specimen 15 C-SCANs are for 0, 110,199, and 160,862 cycles corresponding to crack lengths of 25.917 mm (1.02035 inches), 49.691 mm (1.95635 inches) and 68.87 mm (2.7114 inches). The Specimen 22 C-SCANs are for 0, 92,520 and 148,127 cycles corresponding to 25.208 mm (0.99245 inch), 49.780 mm (1.95985 inches) and 75.671 mm (2.9792 inches). All initial C-SCANs are defect free except for the obvious end disbonds. The second C-SCAN for each specimen corresponds to the point when the crack tips had reached the patch edges. It is evident from these C-SCANs that Specimen 8, although slight, had experienced more cyclic disbonding than either of the 100 MPa specimens. The final C-SCANs correspond to points at which the crack tips are outside of the patch edges. As with the CBP specimen C-SCANs in Figure 65, the 120 ED1 MPa specimen had suffered significantly more cyclic disbonding than the two 100 MPa ED1 specimens as a result of a higher adhesive strain and stress concentration at the adhesive-patch interface. However, comparing the final C-SCANs of Specimens 15 and 22 showed that Specimen 22 had experienced more bondline damage than Specimen 15 at the same stress level. This additional damage, along with the usual scatter of fatigue tests, may explain why Specimen 22 had a greater crack growth rate and shorter fatigue life than Specimen 15. For example, there may have been small levels of porosity in the bondline of Specimen 22 that were undetectable by the ultrasonic C-SCAN apparatus, making it more susceptible to

111

Specimen 8 (120 MPa)
0 Cycles

Specimen 15 (100 MPa)
0 Cycles

Specimen 22 (100 MPa)
0 Cycles

Specimen 8 (120 MPa)
72,013 Cycles

Specimen 15 (100 MPa)
110,199 Cycles

Specimen 22 (100 MPa)
92,520 Cycles

Specimen 8 (120 MPa)
118,076 Cycles

Specimen 15 (100 MPa)
160,862 Cycles

Specimen 22 (100 MPa)
148,127 Cycles
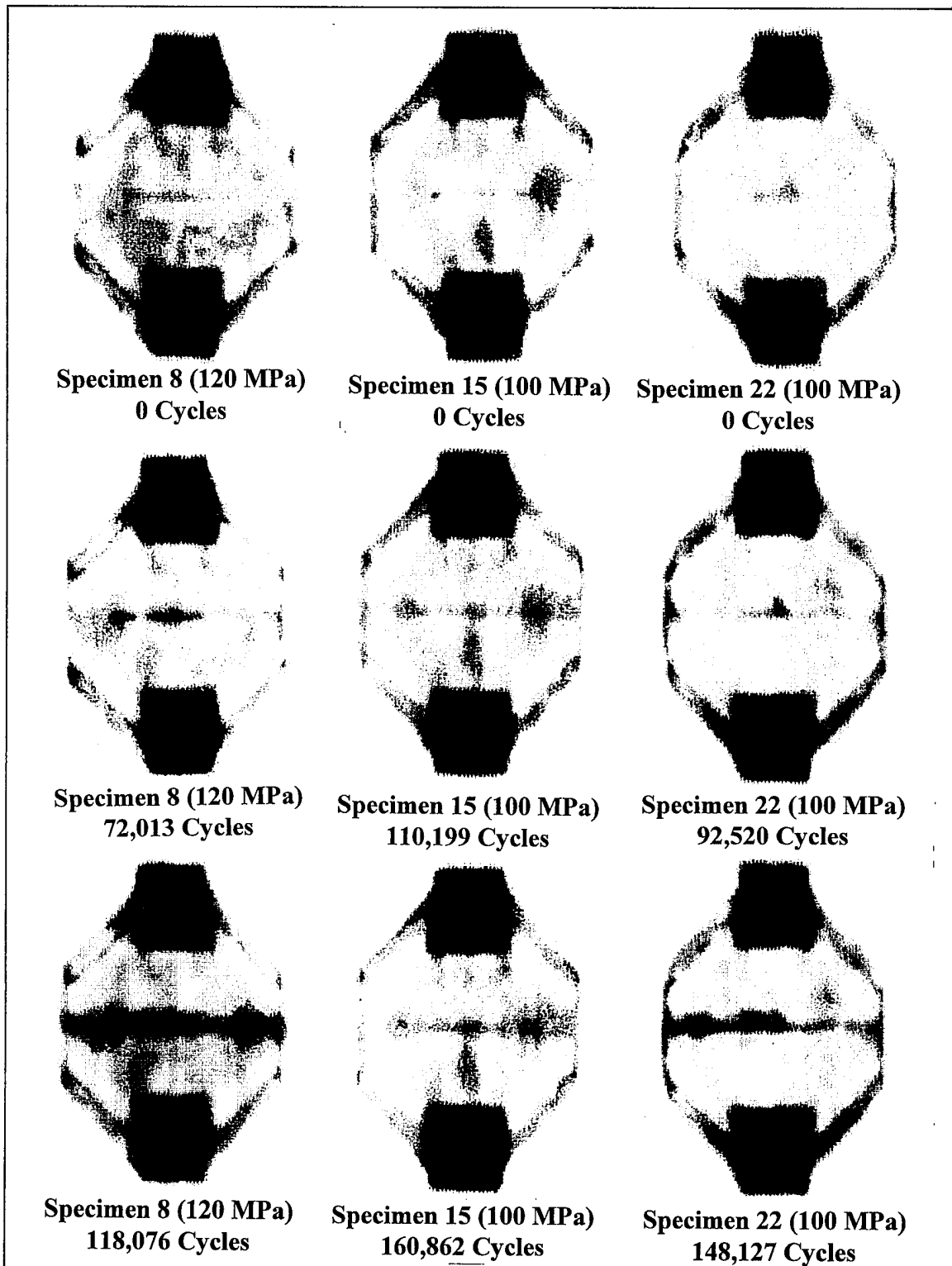
Figure 67. 100 vs. 120 MPa ED1 C-SCANs

cyclic disbonding.

All of the 100 MPa CBP, FWD and ED1 specimens experienced no retardation in the earlier part of crack growth and failed by the patch failure mode as shown in Figure 28 and Appendix A.

Stress Ratio Effects

One specimen, Specimen 3, was tested at $R = 0.15$ while all other specimens were tested at $R = 0.1$. The peak stress level for Specimen 3 was 120 MPa. The fatigue life of Specimen 3 along with the 120 MPa baseline and CBP specimens, at $R = 0.1$, are shown in Table 25. Specimen 3, tested at $R = 0.15$, yielded 15.00 times life extension over the

Table 25. R = 0.15 vs. R = 0.1 Fatigue Lives

Specimen	Configuration	Peak Stress Level (MPa)	$R = \sigma_{min}/\sigma_{max}$	Cycles to Failure
1	Baseline (No Patch)	120	0.1	10,633
3	CBP	120	0.15	159,526
20	CBP	120	0.1	118,316
21	CBP	120	0.1	120,325

baseline specimen and 1.34 times life extension over the CBP specimens tested at $R = 0.1$.

Figure 68 shows the crack length versus cycles curve for the $R = 0.15$ CBP specimen, Specimen 3, and the $R = 0.1$ baseline and CBP specimens. The crack growth rate for Specimen 3 was constant within the patch, once again indicating that the repaired stress intensity factor range, ΔK_R, was constant. The crack growth rate changed from linear only when the crack tips had extended beyond the patch. This behavior is also
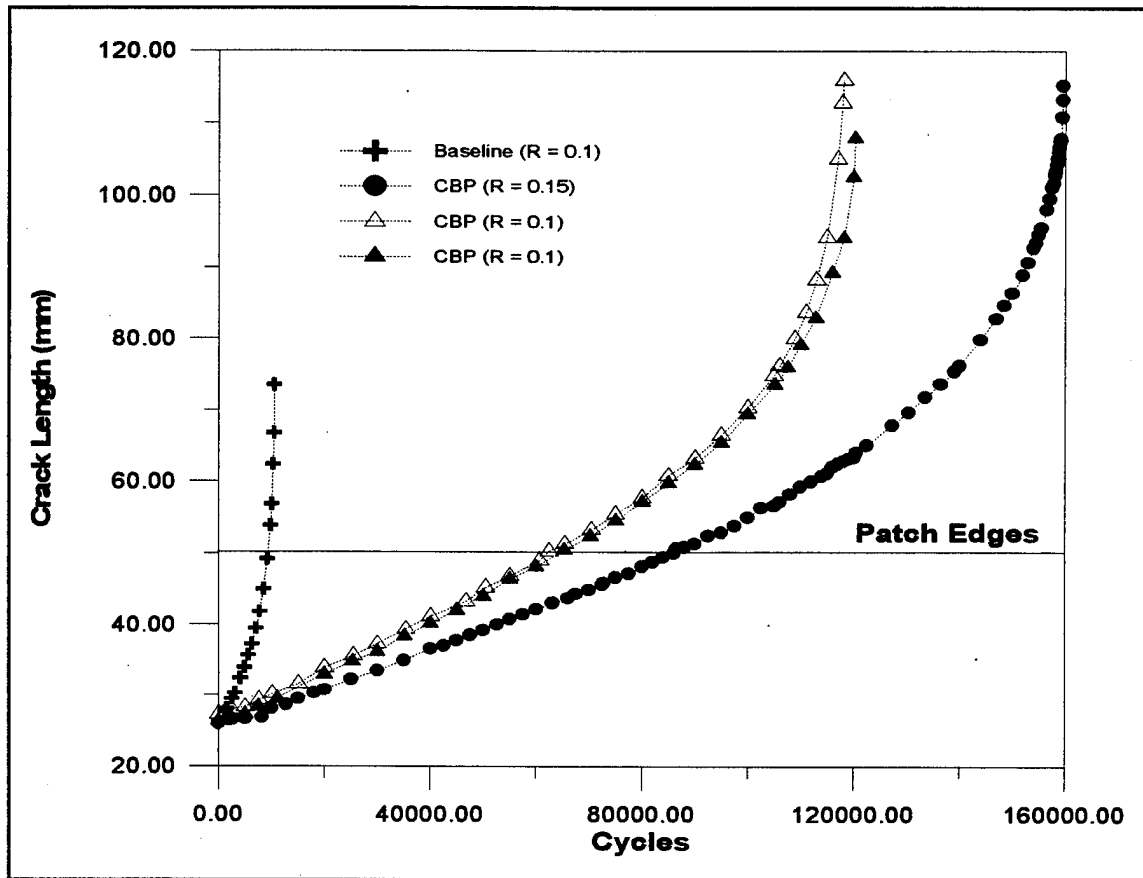
Figure 68. R = 0.15 vs. R = 0.1 Crack Growth

evident from Figure 69 using a three-point least squares method. For comparison

purposes, the average crack growth rates within the patch, the repaired stress intensity

factor range, ΔK_R, and the maximum adhesive shear strain, γ_A^{max}, are shown in Table 26.

ΔK_R and γ_A^{max} were calculated using the Rose model. The values shown were calculated

using the initial crack length of each specimen in Table 5. The repaired stress intensity

factor range, ΔK_R, for the R = 0.15 specimen was 6.2 % less than that for the R = 0.1

specimens. However, the maximum adhesive strain, γ_A^{max}, for both stress ratio cases was

the same because it is a function of the peak stress level and not R. On average, the crack
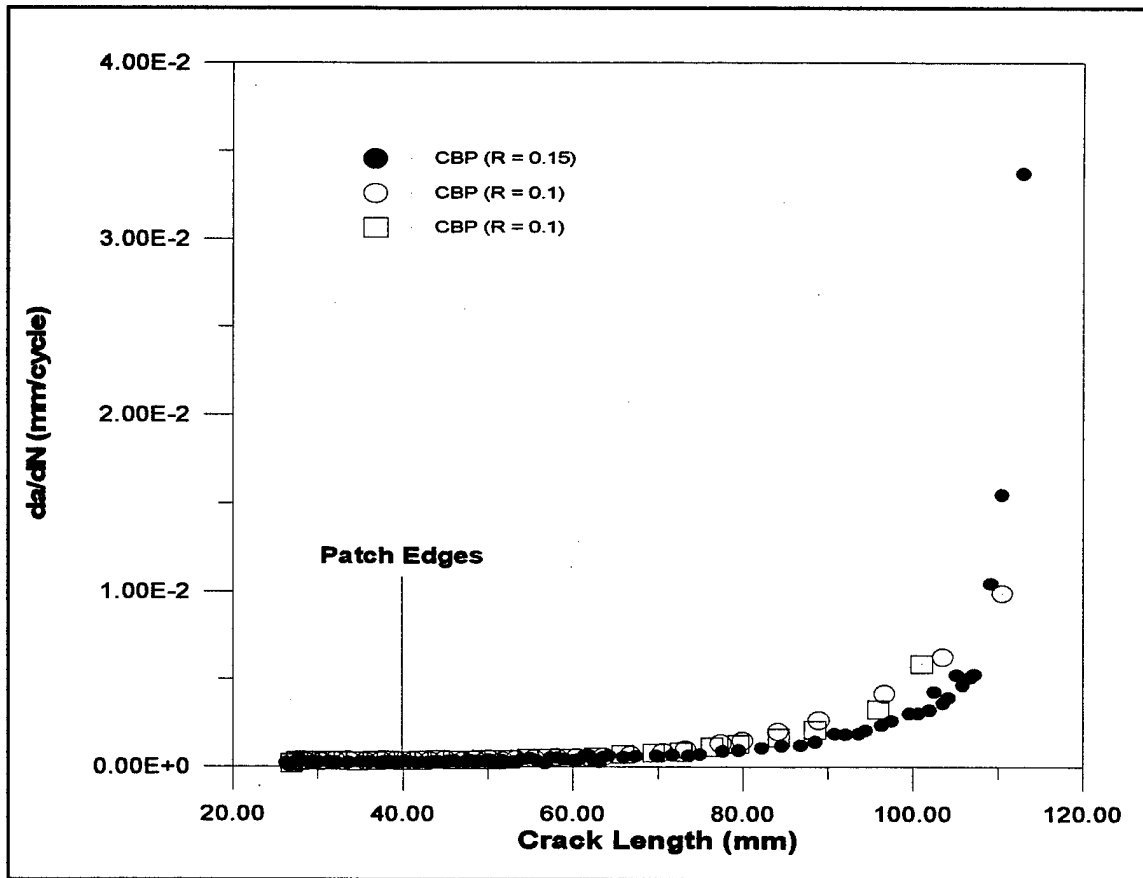
Figure 69. R = 0.15 da/dN vs. Crack Length

Table 26. R = 0.15 vs. R = 0.1 ΔK_R, γ_A^{max}, and da/dN

Specimen	Configuration	ΔK_R (MPa√m)	γ_A^{max} (%)	da/dN (mm/cycle)
3	CBP	4.60	5.1	0.00028160
20	CBP	4.89	5.1	0.00036265
21	CBP	4.88	5.1	0.00036580

growth rate of the R = 0.1 specimens was 1.29 times that of the R = 0.15 specimen. Again, this is consistent with the Paris Law, Equation (16), because da/dN α $\Delta\sigma$ where

$$\Delta\sigma = \sigma_{max} - \sigma_{min} = \sigma_{max} - R(\sigma_{max}) \qquad (19)$$

Figure 70 shows the C-SCANs for Specimens 3 and 20 with stress ratios of 0.15 and 0.1, respectively. Again, the bondline behavior of Specimen 21 (R = 0.1) mirrored that of Specimen 20. The Specimen 3 C-SCANs are for 0, 86,501 and 140,021 cycles corresponding to crack lengths of 25.988 mm (1.02318 inches), 50.634 mm (1.99345 inches) and 76.224 mm (3.00095 inches). The Specimen 20 C-SCANs are for 0, 62,492 and 106,003 cycles which correspond to crack lengths of 27.238 mm (1.07235 inches), 50.221 mm (1.9772 inches) and 76.221 mm (3.00045 inches). C-SCANs of both specimens look similar, both within and outside the patch. When the crack tips had reached the patch edges (second C-SCAN) slight cyclic disbonding was present, but not enough to cause a change in the crack growth rate. Significant disbonding was present when the crack tips had extended beyond the patch edges by approximately 12-13 mm on each side as shown in the third C-SCAN for each specimen. The similar behavior between the two specimens was due to the fact that both had the same peak stress level, and therefore, the same maximum adhesive shear strain. As a result, the repair-adhesive interface experienced the same peak load and strain conditions at both stress ratios, thus producing similar cyclic disbonding behavior.

As with all the R = 0.1 specimens, Specimen 3 (R = 0.15) experienced no retardation in the earlier portion of crack growth and failed by the patch failure mode as shown in Figure 28 and Appendix A.

Specimen 20 (R = 0.1)
0 Cycles

Specimen 3 (R = 0.15)
0 Cycles

Specimen 20 (R = 0.1)
62,492 Cycles

Specimen 3 (R = 0.15)
86,501 Cycles

Specimen 20 (R = 0.1)
106,003 Cycles

Specimen 3 (R = 0.15)
140,021 Cycles
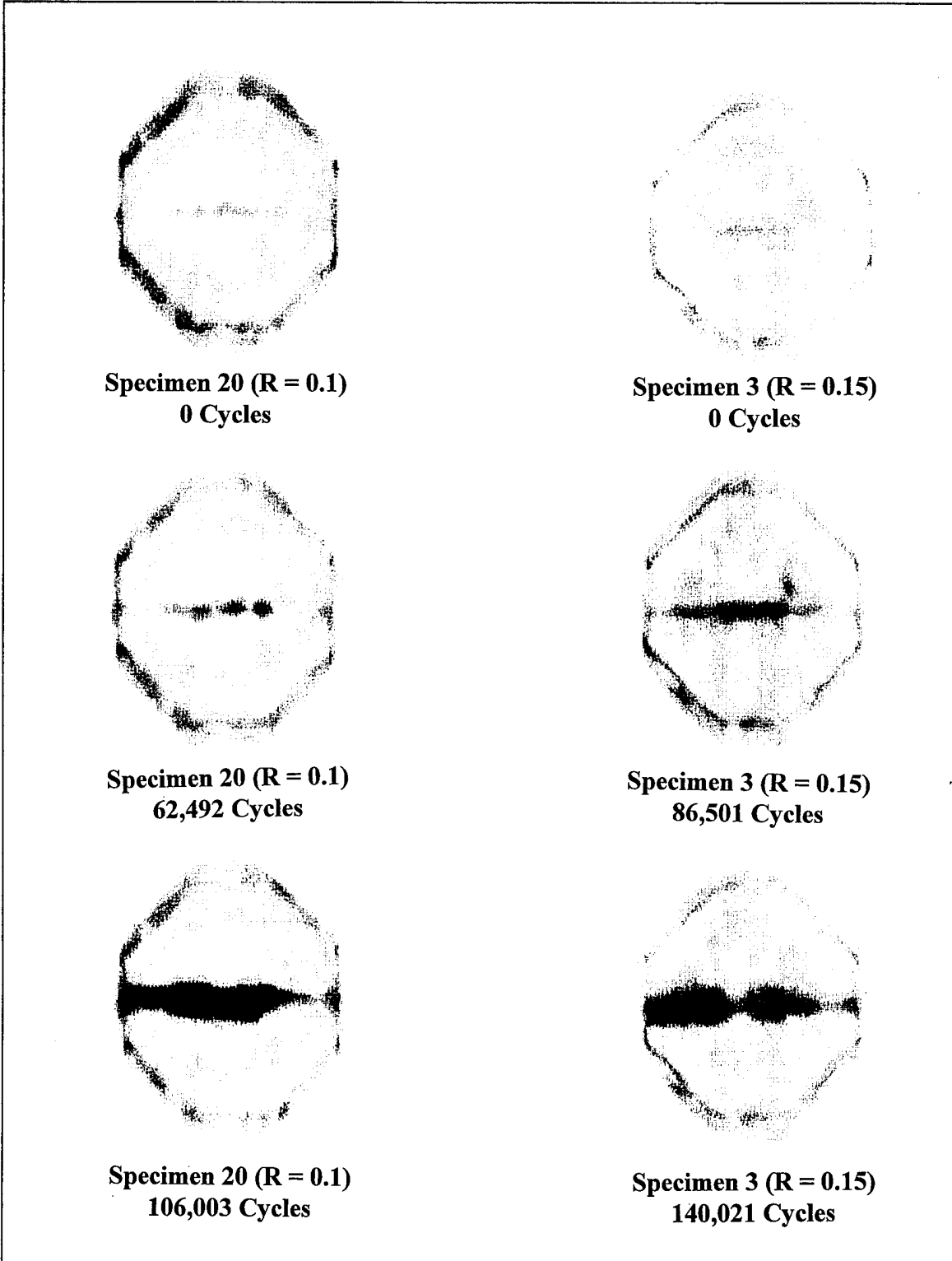
Figure 70. R = 0.15 vs. R = 0.1 C-SCANs

High versus Low Modulus Adhesive

As presented in Chapter 2, paste adhesives are available in one or two-part form and are applied by a spatula or other spreading equipment. A two-part paste adhesive was investigated in this effort consisting of a liquid epoxy resin and a cross-linking agent. A comparison of the two adhesives, two-part paste and film, employed in this effort is shown in Table 27. As can be seen from Table 27, EA-9394 has a shear modulus that is 3.6 times that of AF-163-2 and a yield strain that is only 18 % of the yield strain of AF-163-2.

Table 27. EA-9394 vs. AF-163-2 Adhesives

Adhesive	Form	Supplier	G_A (MPa)	γ_{yieldA} (%)	Cure Temp (°C)
EA-9394	Paste	Hysol	1461	1.66	93
AF-163-2	Film	3M	405.8	≈ 9	121

Paste adhesives have the advantage of room or temperature cure, however, a one-hour cure at 93 °C (200 °F) was employed in this effort. Two specimens, 25 and 26, were tested using EA-9394 at a peak stress of 120 MPa, a stress ratio of 0.1 and a CBP configuration. The fatigue lives of the EA-9394 CBP specimens along with the 120 MPa baseline and AF-163-2 CBP specimens are shown in Table 28. Specimen 25 yielded 8.50

Table 28. EA-9394 vs. AF-163-2 Fatigue Lives

Specimen	Configuration	Adhesive	Cycles to Failure
1	Baseline (No Patch)	NA	10,633
20	CBP	AF-163-2	118,316
21	CBP	AF-163-2	120,325
25	CBP	EA-9394	90,376
26	CBP	EA-9394	77,967

times life extension over the baseline specimen while Specimen 26 yielded 7.33 times life extension. As compared to the film adhesive CBP specimen average of 119,320 cycles to failure, Specimen 25 yielded 0.76 times life extension while Specimen 26 only managed a 0.65 times life extension.

Fredell (15:124) states that "a stiffer adhesive exhibits less strain than a flexible (toughened) adhesive. However, the stiffer adhesive also reaches its yield point at a much lower adherend normal stress." In other words, a stiffer adhesive is better in reducing the repaired stress intensity factor, K_R, with the added risk of approaching its yield strain around the crack, resulting in greater delamination as compared to a toughened adhesive. With this in mind, the Rose model, with the initial crack length of each specimen, was used to calculate the repaired stress intensity factor, K_R, and the maximum adhesive shear strain, γ_A^{max}, around the crack. The results are shown in Table 29, along with the average

Table 29. EA-9394 vs. AF-163-2 K_R, γ_A^{max}, and da/dN

Specimen	Adhesive	K_R (MPa√m)	γ_A^{max} (%)	da/dN (mm/cycle)
20	AF-163-2	5.43	5.16	0.00036265
21	AF-163-2	5.42	5.16	0.00036580
25	EA-9394	4.06	2.72	0.00044365
26	EA-9394	4.03	2.72	0.00052491

crack growth rate based on a three-point least squares method. On average the higher modulus paste adhesive yielded an additional 34.1 % reduction in K_R over the toughened film adhesive with lower modulus. However, the maximum shear strain of the paste adhesive exceeded its yield strain by 64 %, indicating probable delamination around the

crack. This will be addressed again through C-SCAN evaluation. Finally, the crack growth rate of Specimen 25 was 1.22 times the AF-163-2 CBP specimen average and Specimen 26 was 1.44 times this average, a significant reduction in patching efficiency.

Figure 71 shows the crack length versus cycles curve for the Baseline and the EA-9394 and AF-163-2 CBP specimens. As already presented, the two AF-163-2 specimens demonstrated constant crack growth within the patch repair, however, the EA-9394 specimens demonstrated a slight parabolic trend in crack growth within the patch. This indicated an increase in the repaired stress intensity factor range, ΔK_R, with crack length. This decrease in patching efficiency was the result of significant cyclic disbonding during crack growth which is also evident by the increasing da/dN trend within the patch as shown in Figure 72. The increased level of inconsistency between the two EA-9394 specimens as compared to the two AF-163-2 specimens in Figure 71, may be due to inadequate mixing of the adhesive before application, more porosity in the bondline of one EA-9394 specimen as compared to the other, or nonuniformity of the bondline thickness.

Figure 73 shows the C-SCANs for Specimens 20 (AF-163-2) and 26 (EA-9394). The Specimen 20 C-SCANs are for 0, 62,492 and 106,003 cycles corresponding to crack lengths of 27.238 mm (1.07235 inches), 50.221 mm (1.9772 inches) and 76.221 mm (3.00045 inches). The Specimen 26 C-SCANs are for 0, 28,005, 47,609 and 70,450 cycles corresponding to crack lengths of 25.277 mm (0.99515 inches), 38.073 mm (1.49895 inches), 50.074 mm (1.9714 inches) and 70.793 mm (2.78715 inches). The most important feature of the EA-9394 C-SCANs, that was not present in any of the prior AF-163-2 specimen C-SCANs, is the significant amount of disbonding that occurred for
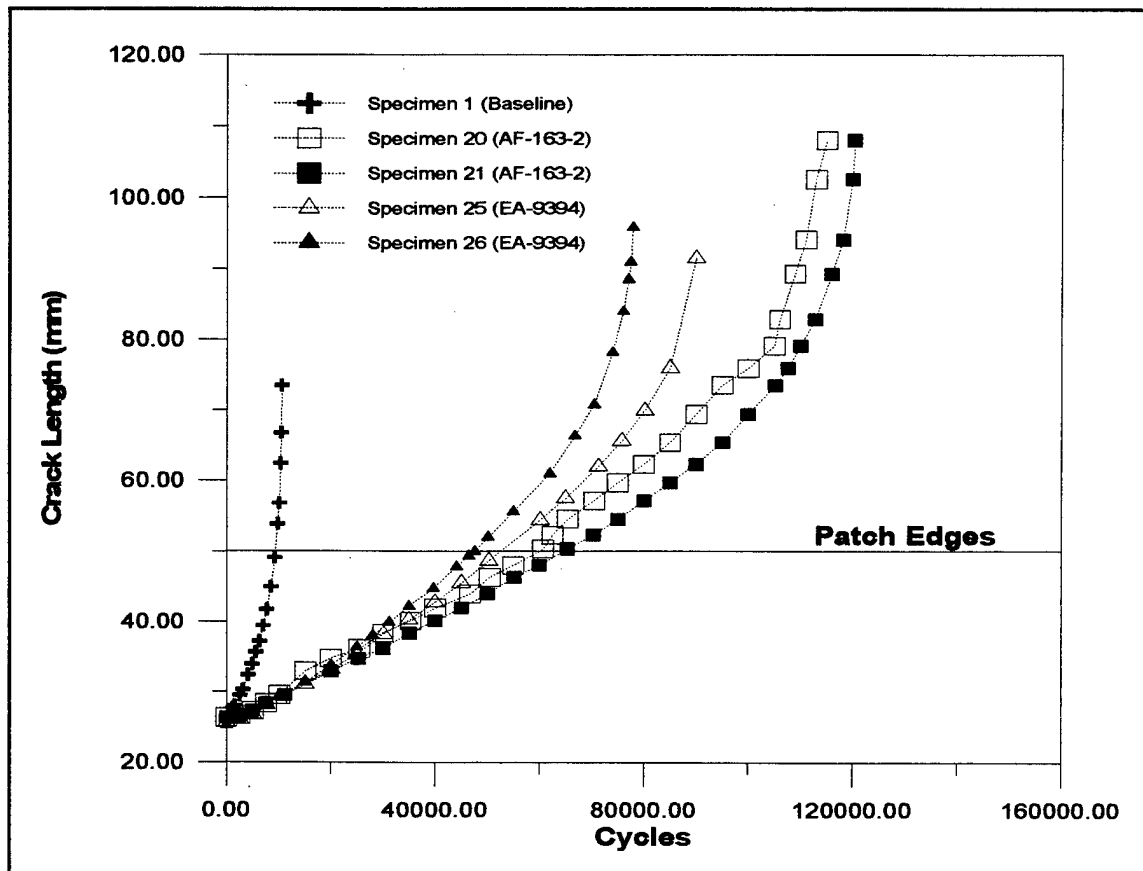
Figure 71. EA-9394 vs. AF-163-2 Crack Growth

crack growth within the patch. This is evident from the 28,005 cycle C-SCAN and was

due primarily to the adhesive maximum shear strain, γ_A^{max}, exceeding its yield value around

the crack. Disbond progression is evident for crack growth out to the patch edges

(47,609 cycle C-SCAN), explaining the reduction in patching efficiency for crack growth

within the repair. As with the AF-163-2 specimens, disbonding was more prevalent for

crack growth outside the repair (70,450 cycle C-SCAN), however, the level of disbonding

for the EA-9394 adhesive far exceeded that of any specimen employing the toughened

AF-163-2 film adhesive. Again this was due to the adhesive exceeding its yield strain.
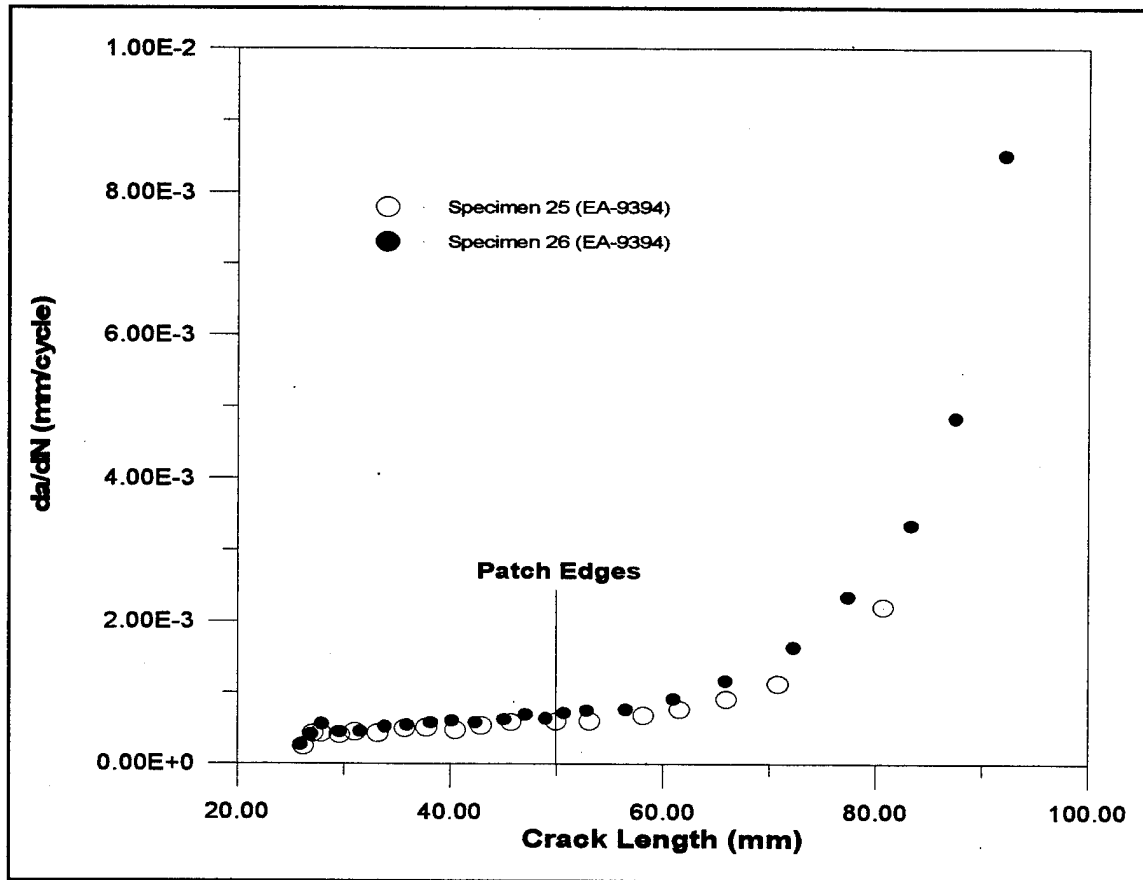
Figure 72. EA-9394 da/dN vs. Crack Length

Similar to the AF-163-2 specimens, the EA-9394 specimens did not demonstrate any retardation of crack growth before re-initiation as shown in Figure 74. Again, this was the result of using a high cure temperature, 93 °C, during the bonding process which annealed out the beneficial compressive stresses in the crack tip plastic zone. This agrees with Baker's (8) findings for cure temperatures above 80 °C. If a room temperature cure had been employed, retardation may have been present.

Finally, both Specimens 25 and 26 failed by the patch failure mode shown in Figure 28 and Appendix A.

Specimen 20 (AF-163-2)
0 Cycles

Specimen 26 (EA-9394)
0 Cycles

Specimen 26 (EA-9394)
70,450 Cycles

Specimen 20 (AF-163-2)
62,492 Cycles

Specimen 26 (EA-9394)
28,005 Cycles

Specimen 20 (AF-163-2)
106,003 Cycles

Specimen 26 (EA-9394)
47,609 Cycles
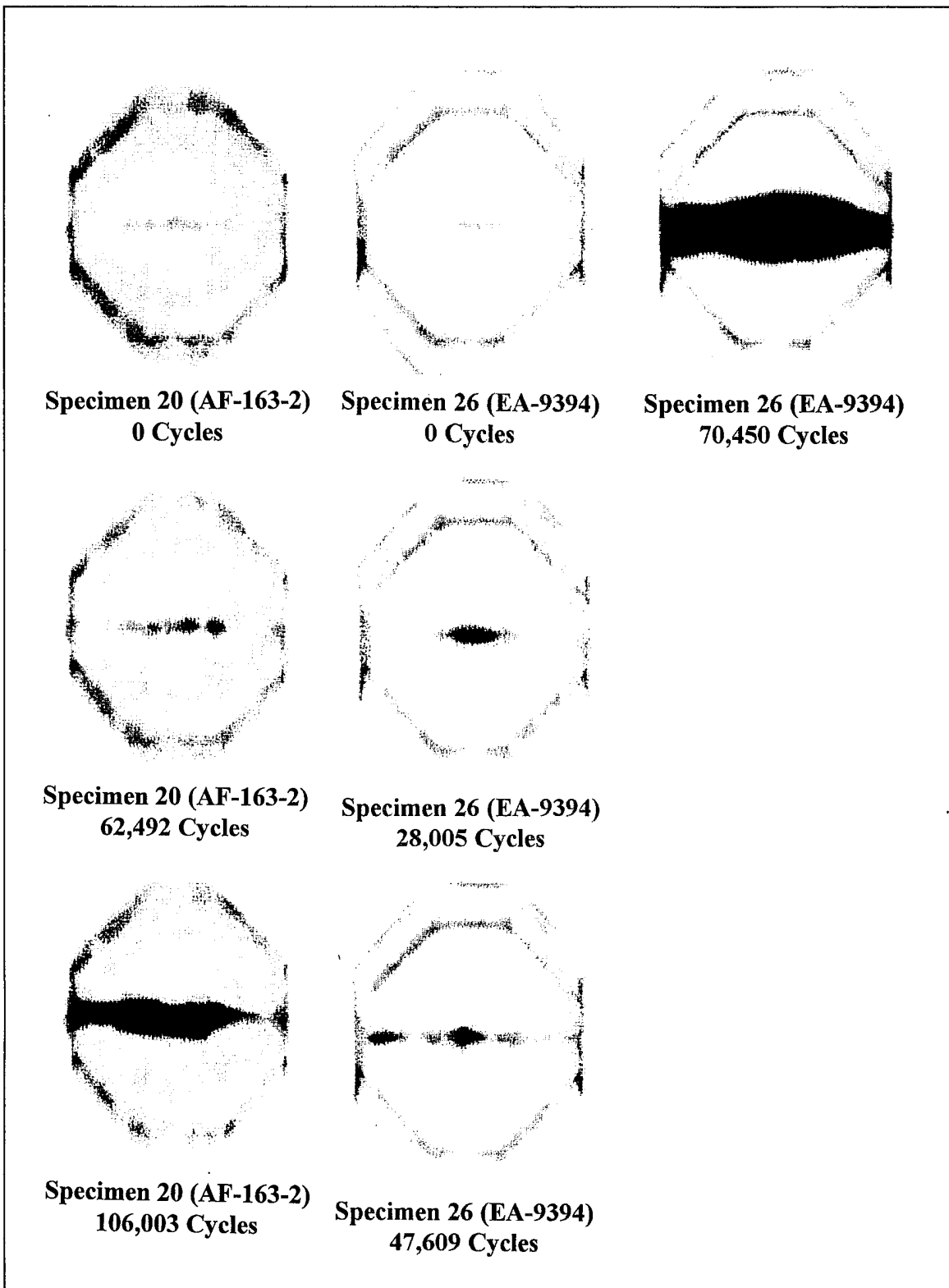
Figure 73. EA-9394 vs. AF-163-2 C-SCANs
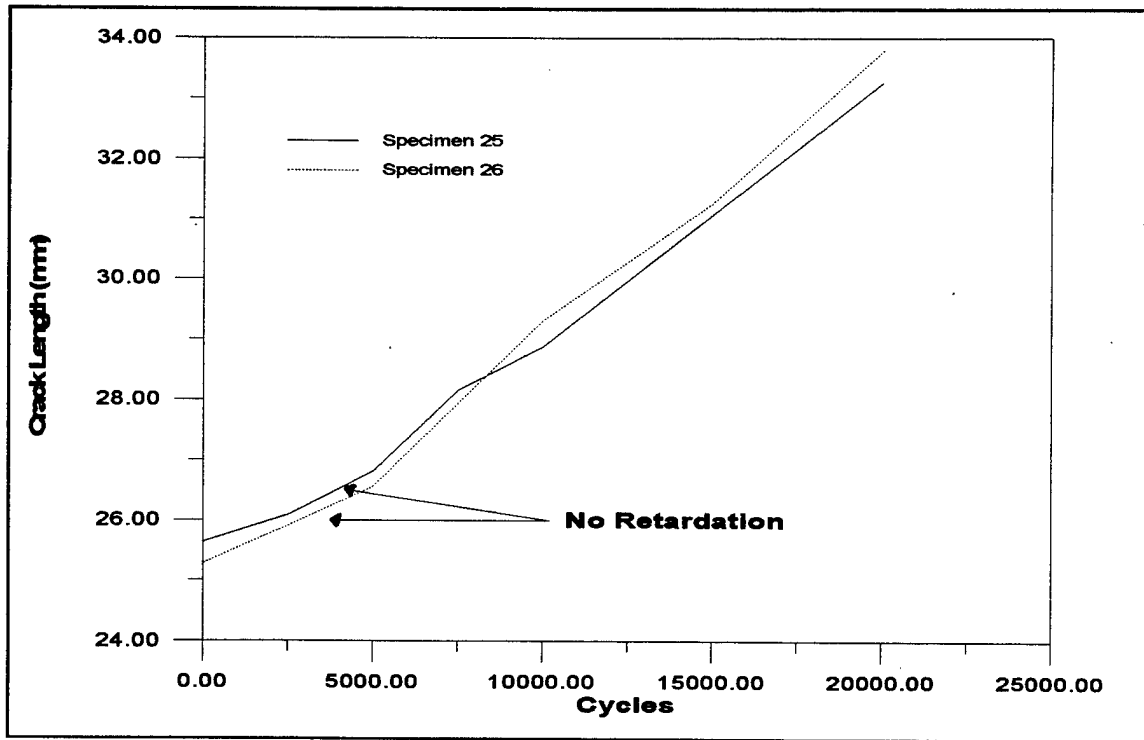
Figure 74. EA-9394 Retardation of Crack Growth

Effectiveness of Electric Potential Difference

A DC electric potential difference (EPD) system was investigated as a possible means for automated crack measurement. The system is shown schematically in Figure 19 with the voltage lead attachments to the specimen shown in Figure 23. The system employed a 5 A electric current to produce a two-dimensional electric field which was constant through the specimen thickness at all points. The formation of an oxide layer on the fresh fracture surface insulated the two halves of the specimen during fatigue testing. This progression of insulation resulted in a increasing voltage drop across the crack plane allowing the progressive determination of crack length. A closed form solution to

compute the crack length from this method has been developed

$$a = \frac{W}{\pi} Cos^{-1} \left\{ Cosh\left[\frac{\pi Y_0}{W}\right] \middle/ Cosh\left[\frac{V}{V_r} Cosh^{-1}\left(Cosh\left(\frac{\pi Y_0}{W}\right) \middle/ Cos\left(\frac{\pi a_r}{W}\right)\right)\right] \right\} \quad (15)$$

for $0 \le 2a/W \le 1$,

where a is the crack length, a_r is the reference crack length determined by another method (optical was used in this effort), W is the specimen width, V is the measured EPD voltage, V_r is the reference voltage corresponding to a_r, and Y_0 is the voltage lead distance from the crack plane (5: 695-698).

Before implementation of the EPD system with patched specimens, a series of tests were conducted to evaluate the accuracy of the system. As can be seen from Figure 75, the EPD prediction of crack growth, for unpatched panels, were in agreement with the optical measurements using a traveling microscope. Unfortunately, EPD was not successful with the patched panels investigated in this effort. Figures 76, 77, and 78 show EPD versus optical crack measurements for the first 30,000 - 40,000 cycles of Specimens 5, 7 and 9. All these figures demonstrate the same trend. The EPD system was measuring an increase in crack length, however, at a significantly reduced rate. The reference crack length, a_r, was updated at each optical measurement to see if the same trend occurred at different crack lengths. The repeated trend is evident in Figures 76, 77, and 78. The only possible explanation for this repeated growth trend at different crack lengths was due to contact of the fracture surface which caused a shortening of the electric voltage. In other words, a slightly greater crack opening displacement occurred on the unpatched side of
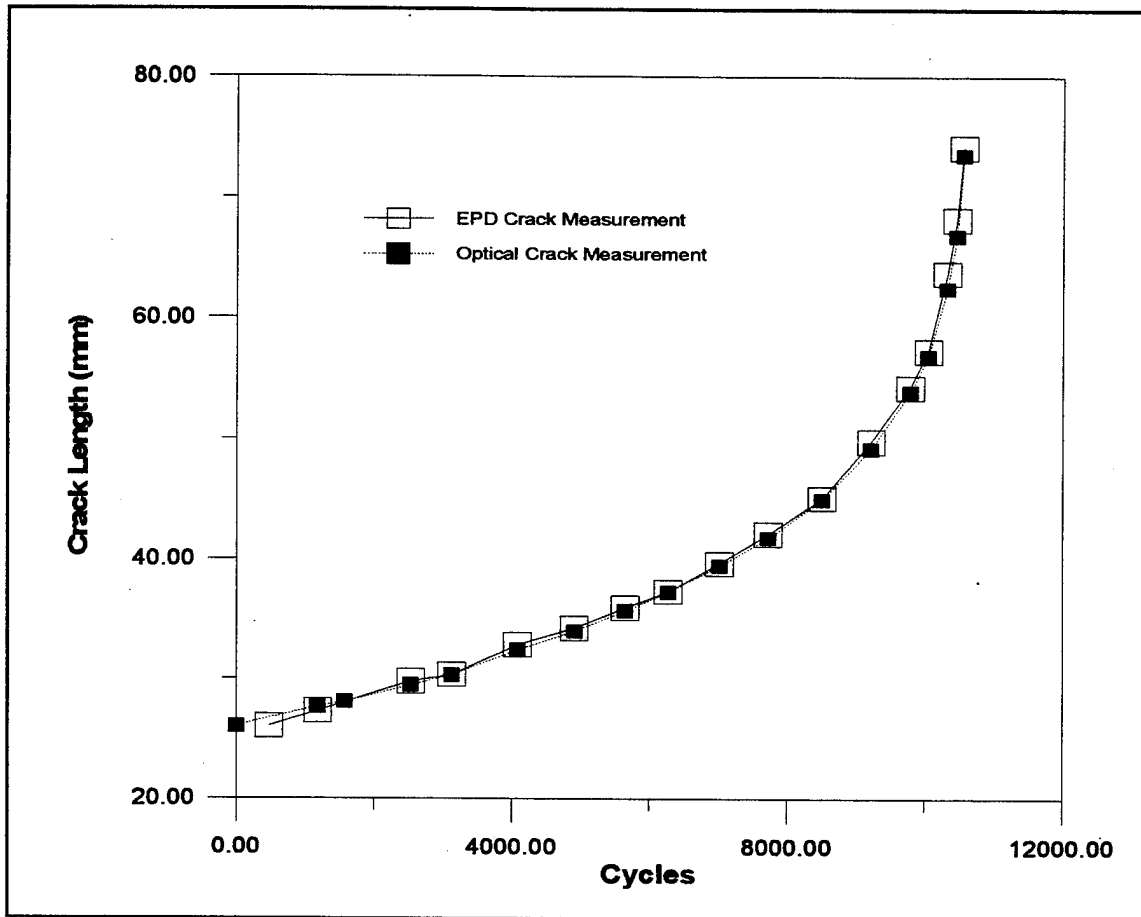
Figure 75. Unpatched EPD vs. Optical Crack Measurements

the aluminum panel, with the patched side possessing enough of a closure force to disallow the adequate formation of the insulating oxide film. As a result, an electrical short was created giving a under-estimation of the physical fatigue crack size. This phenomenon is illustrated in Figure 79. As a result, patched panel crack growth measurement was accomplished optically using the traveling microscope.
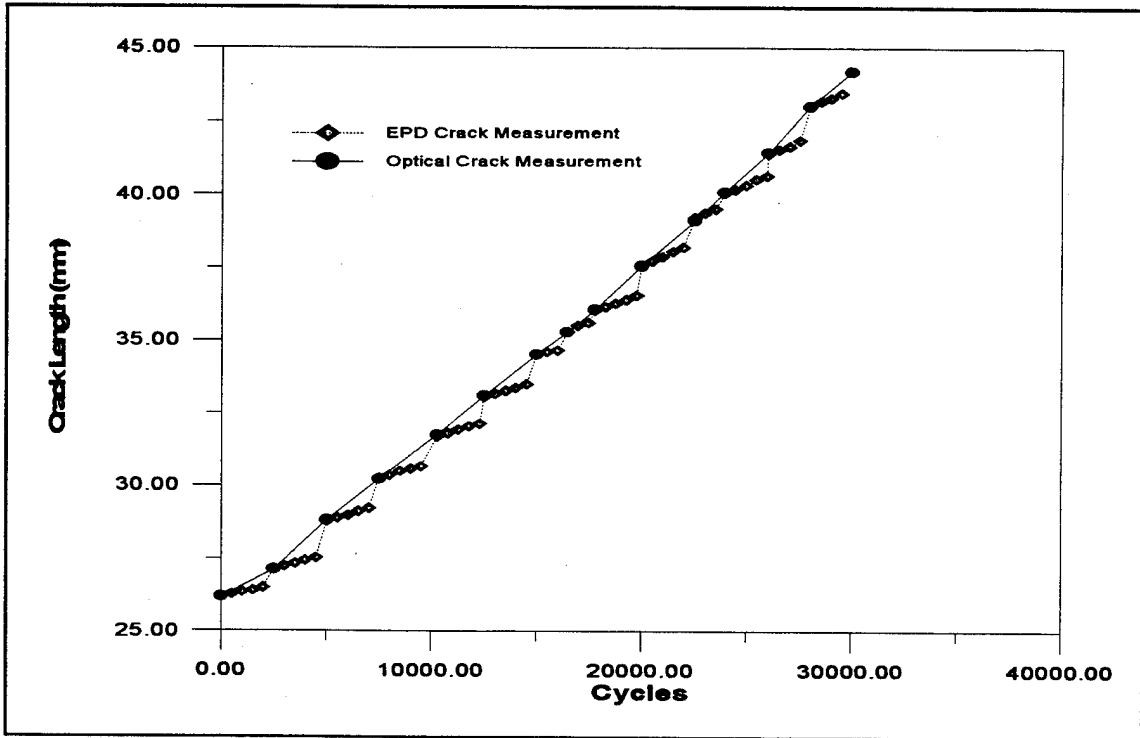
Figure 76. Patched EPD vs. Optical Crack Measurements
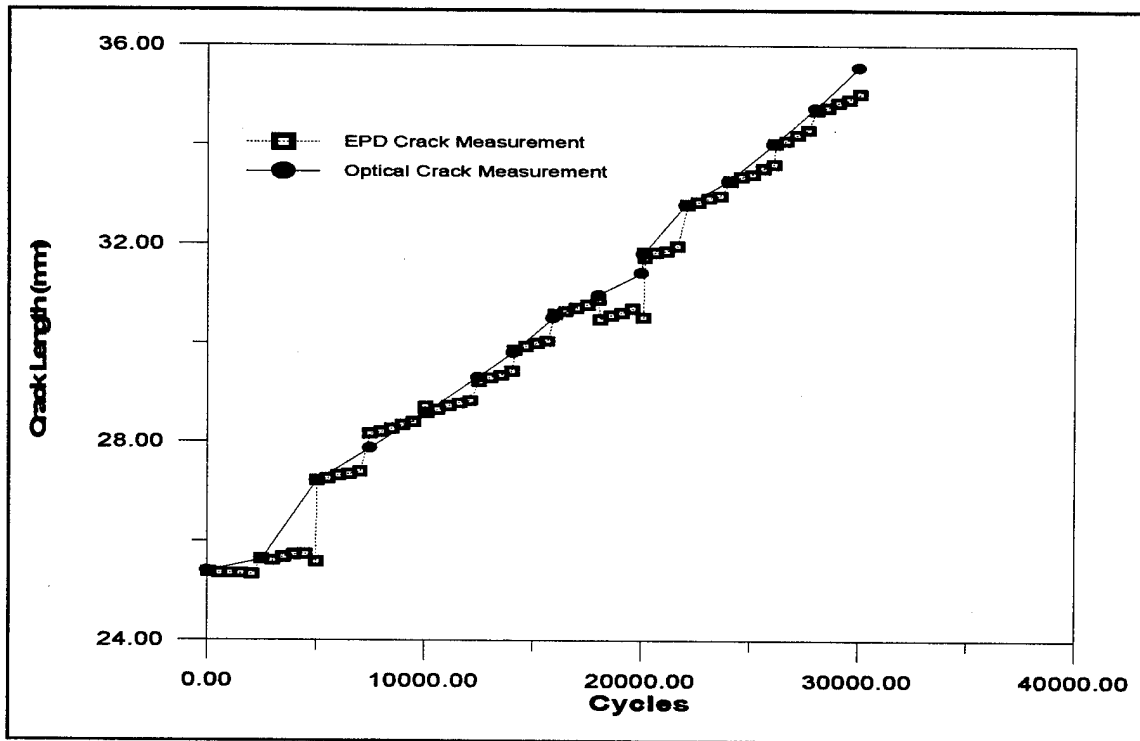
Figure 77. Patched EPD vs. Optical Crack Measurements

127
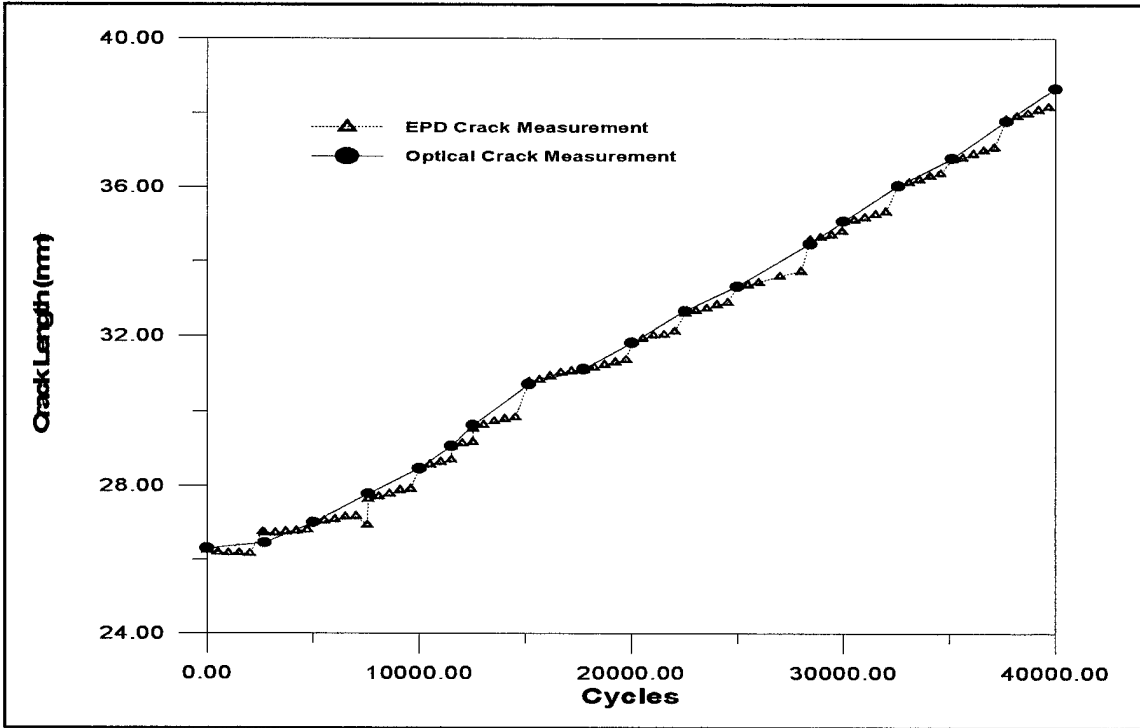
Figure 78. Patched EPD vs. Optical Crack Measurements
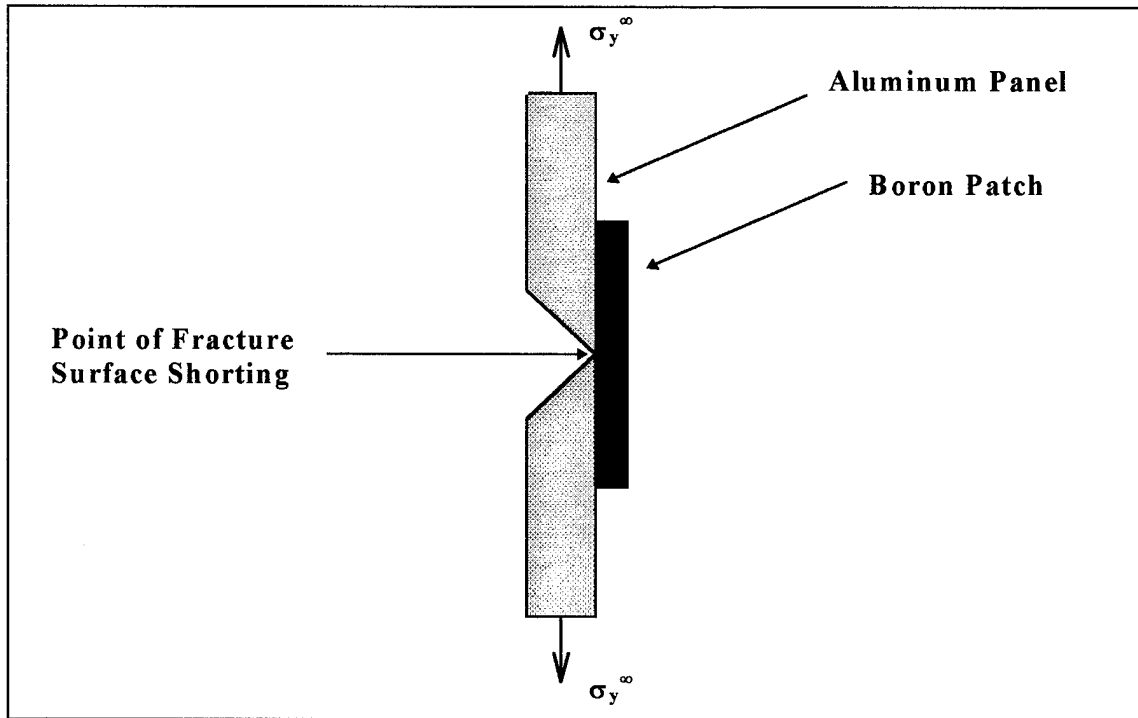
Figure 79. EPD Shorting

128

Summary

As shown above, patching efficiency is definitely dependent on disbond location, disbond size, peak stress level, stress ratio, and the adhesive. Figure 80 shows the comparison of typical crack growth curves for the five general disbond configurations
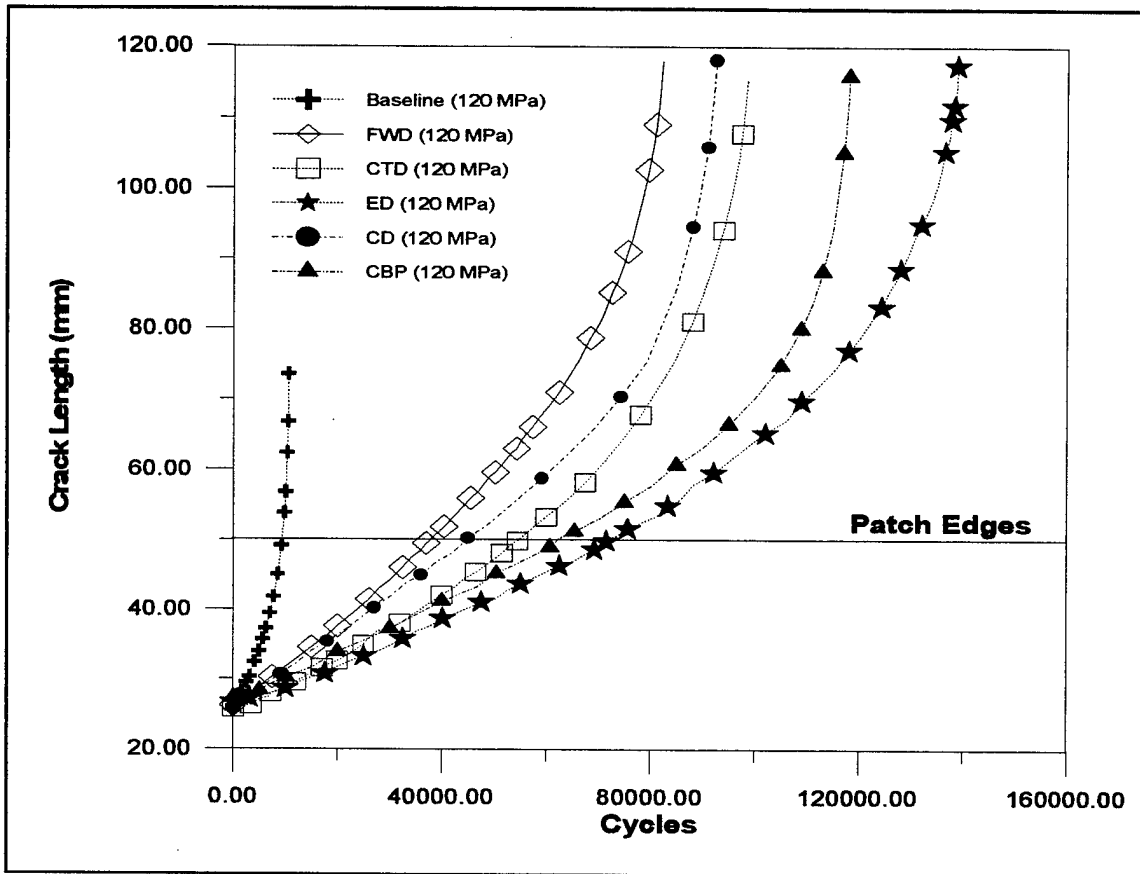
Figure 80. Summary of Disbond Location Effects

(Figure 3) investigated in this study. All these crack growth curves are at a maximum stress level of 120 MPa. The baseline configuration without a patch only has a life of 10,633 cycles. As previously discussed, a disbond covering the crack during the crack

growth within the patch (FWD, CD and CTD) resulted in a reduction of patching efficiency as compared to a completely bonded patch (CBP). Again, the full width disbond (FWD) configuration which displaced the point of load transfer from the plate to the patch away from the crack faces (Figure 32) as well as completely covering the crack with a disbond during crack growth was the worst case studied among all disbond cases, resulting in a crack growth rate within the patch that was 1.65 times that of a completely bonded patch. The crack tip disbond (CTD) and center disbond (CD) configurations, although not as severe as the FWD configuration, also had disbonds over portions of the crack that displaced the point of load transfer. The CTD and CD configurations produced crack growth rates that were 1.16 and 1.47 times that of the completely bonded patch. The CD configuration was less efficient than the CTD configuration because a larger portion of the crack was covered by a disbond during crack growth within the patch.

The end disbond (ED) configurations actually improved patching efficiency over the CBP configuration by making the patch shorter which attracted less parasitic load. However, with a thicker and higher stressed patch and panel, end disbond growth may occur due to greater peel forces as a result of secondary bending. This may cause disbond growth leading to a corresponding reduction in patching efficiency. Also, varying disbond size around the crack in both the x and y-directions (Figure 52), although not as noticeable effect as varying disbond location, resulted in a reduced patching efficiency with increased disbond size (Figure 54 and 56). For example, increasing the disbond size for both the FWD and CD configurations from only 5 % to 10 % of the total bond area resulted in an additional 28 % increase in the crack growth rate. Finally, the pre-existing disbonds in the

130

bondline of the repair did have a noticeable effect on the crack growth rate and the total life of each specimen. However, in all disbond locations and sizes investigated, the bondline proved to be relatively damage tolerant of pre-existing flaws.

Based on the Paris Law, Equation (16), increasing the peak stress level increases ΔK, thus increasing the crack growth rate within the patch as well as increasing the amount of cyclic disbonding. Conversely, increasing the stress ratio reduces ΔK, and thus, increases the fatigue life of the specimen. However, different stress ratios have no effect on the amount of cyclic disbonding because the maximum adhesive shear strain is a function of the peak stress level. Finally, adhesives with higher modulus, although effective in reducing the repaired stress intensity factor, are more susceptible to cyclic disbonding due to a reduced adhesive yield strain capability.

V. Analysis

The purpose of this chapter is to present a simple damage tolerance approach to account for the effect of disbond location and size. Using weighting factors for disbond location (λ) and size (η), it is possible to modify the empirical crack growth equation

$$da/dN = C(\Delta K)^n \qquad (16)$$

proposed by Paris (9) to

$$(da/dN)_{eff} = C(\Delta K_{eff})^n = C(\eta\lambda\Delta K_{CBP})^n \qquad (20)$$

where ΔK_{CBP} is the repaired stress intensity range for a completely bonded patch (CBP), C and n are material constants, λ and η are the disbond location and size weighting factors, respectively applied to ΔK_{CBP} to yield an effective stress intensity factor range, $\Delta K_{eff} = \eta\lambda\Delta K_{CBP}$, to account for the given disbond configuration.

Determination of C and n

The parameters, C and n, are obtained from a $\log(da/dN)$ versus $\log(\Delta K_{CBP})$ plot from the crack growth data within a completely bonded patch. Specimen 19 (CBP) fatigued at 90, 110, 130, and 140 MPa, Specimen 10 (CBP) fatigued at 100 MPa, and Specimen 20 (CBP) and 21 (CBP) fatigued at 120 MPa produced the $\log(da/dN)$ versus $\log(\Delta K_{CBP})$ relationship as shown in Figure 81. From a linear curve fit of the 100, 110, 120, 130, and 140 MPa data points, C and n, for a completely bonded patch, are 3.31×10^{-5} and 1.48. This value of n is within the range (1.16-2.7) presented in Chapter 4. The 90
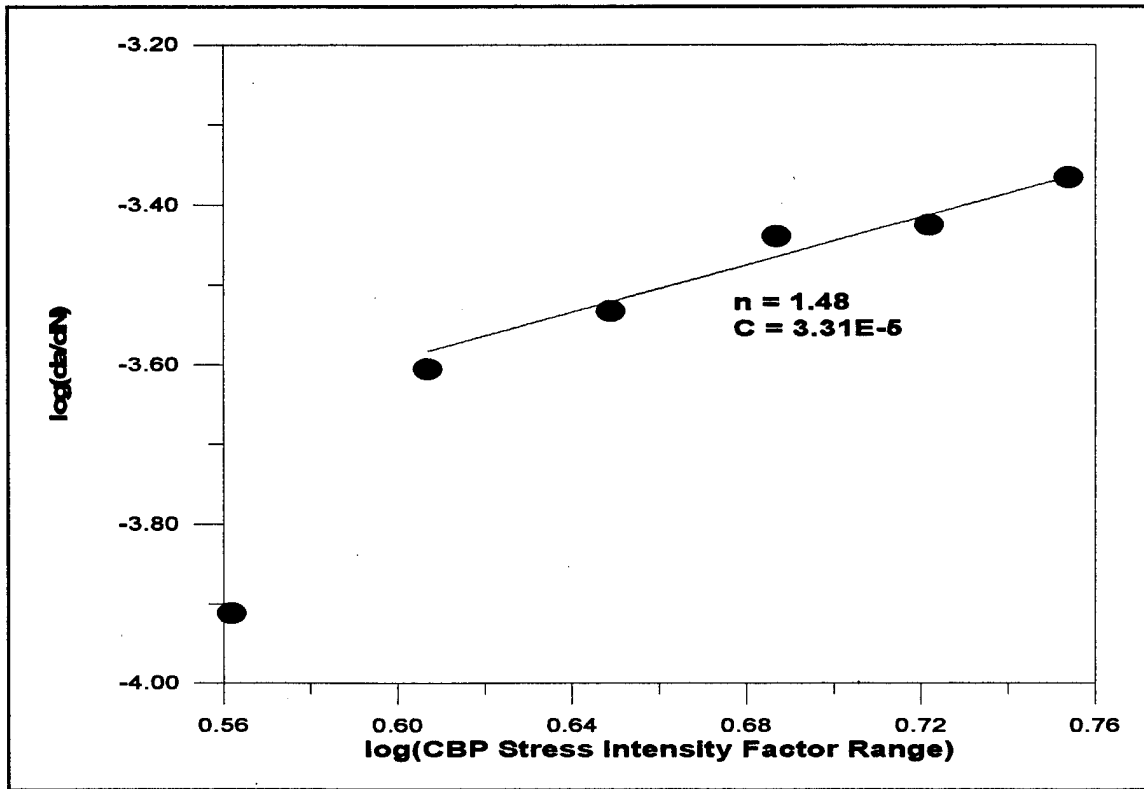
Figure 81. Log(da/dN) versus Log(ΔK_{CBP})

MPa data point in Figure 81 was not used to determine the parameters C and n because it was not in agreement with the other data points, probably due to scatter or due to the 90 MPa point being on the lower end of the sigmoidal log(da/dN) versus log(ΔK_{CBP}) curve.

Estimation of the Location Weighting Factor

Using the experimental crack growth rate for each disbond configuration for a given area of disbond, (da/dN)$_{eff}$, the location weighting factor can be determined by

$$\lambda = \left\{ \frac{\left(da/dN\right)_{eff}}{C\left(\Delta K_{CBP}\right)^{n}} \right\}^{\frac{1}{n}} \qquad (21)$$

133

Using the average crack growth rate for several disbond configurations with a 20 % area disbond, the location weighting factors and the effective stress intensity ranges were calculated as presented in Table 30. A ΔK_{CBP} of 4.86 MPa√m, based on a nominal crack

Table 30. Disbond Location Weighting Factors

Configuration[*]	Disbond Size (≈ % of Total Bond Area)	Location Weighting Factor, λ	ΔK_{eff} (MPa√m)	ΔK_{Rose} (MPa√m)
CBP	0	1.00	4.86	4.86
FWD[♠]	20	1.46	7.10	NA
CTD[♠]	20	1.15	5.56	NA
ED1	20	0.97	4.71	4.33

[*]See Figure 3.
[♠]Rose model does not apply for these configurations.

length of 25.4 mm (1.0 inch), was used in this determination of λ. Two features may be noted from these calculations. The first one is that disbonds covering the crack are more damaging than disbonds in front of (CTD) or away from the crack (ED1). The second one is that the reduction in ΔK_{CBP} for the ED1 configuration is only 3 % (i.e. 4.86 MPa√m to 4.71 MPa√m) as compared to the 11 % reduction (4.86 MPa√m to 4.33 MPa√m) as calculated using the Rose model. This difference is due to the Rose model's assumption of an elliptical patch. The end disbonds of the ED1 configuration (Figure 40) are 18 mm long, thus, forcing the patch away from an elliptical shape as used in the Rose model. As a result, an additional 8 % error in the Rose model stress intensity range, ΔK_{Rose}, is seen.

Estimation of the Size Weighting Factor

Now, given the location weighting factors in Table 30 based on a 20 % area

disbond, it is possible to determine the disbond size weighting factors as

$$\eta = \left\{ \frac{(da/dN)_{\mathit{eff}}}{C(\lambda \Delta K_{CBP})^n} \right\}^{\frac{1}{n}} \qquad (22)$$

Only full width disbond (FWD) configurations are investigated here for size effects (Figure

53). The computed disbond size weighting factors are shown in Table 31. The FWD

Table 31. Disbond Size Weighting Factors for FWD Configuration

Configuration	Disbond Size (≈ % of Total Bond Area)	Size Weighting Factor, η
FWD*	20	1.00
FWD*	10	0.96
FWD*	5	0.82

*η normalized to 20 % FWD configuration.

configuration size weighting factors are normalized to the 20 % disbond size because the

20 % FWD was used in determining the location weighting factor, λ. As can be seen from

Table 31, the larger the disbond, the greater the reduction in patching efficiency. Again,

for a FWD configuration, the increase in crack growth rate with disbond size was the

result of displacing the point of load transfer between the plate and the patch away from

the crack faces as shown in Figure 32.

Verification of Approach

With the availability of an approach to account for the disbond location and size effect on the patching efficiency, an attempt will be made to determine the patching efficiency for the disbond configurations ED2 (Figure 40) and CD (Figure 46). First, the ED2 configuration with a 20 % area disbond and a CD configuration with a 10 % area disbond will be investigated. A CD configuration, with only a 10 % area disbond, can be used to estimate the location effect because varying the area in the y-direction (as defined in Figure 52) from 20 % to 10 % disbond area around the crack has minimal effect on efficiency as demonstrated for the FWD configuration in Table 31 and as discussed in Chapter 4. Finally, size effects on a CD configuration in going from a 10 % to a 5 % area disbond will be estimated.

Location Effects. The ED2 configuration, with end disbonds as shown in Figure 40, is expected to provide a comparable patching efficiency as the ED1 configuration, i.e. similar ΔK_{eff} values. Table 32 compares these two end disbond configurations. Based on

Table 32. ΔK_{eff} for ED1 vs. ED2

Configuration	Disbond Size ($\approx$ % of Total Bond Area)	Location Weighting Factor, λ	ΔK_{eff} (MPa$\sqrt{m}$)	ΔK_{Rose} (MPa$\sqrt{m}$)
ED1	20	0.97	4.71	4.33
ED2	20	0.95	4.62	4.61

the average crack growth rate within the patch, $(da/dN)_{eff}$, Equation (21) predicts a ED2 configuration location weighting factor of 0.95 and a ΔK_{eff} of 4.62 MPa$\sqrt{m}$. The ΔK_{eff} for

the ED2 configuration is only 2 % below that of the ED1 configuration, i.e. similar

patching efficiency as expected with similar disbond location. Also of interest is the

comparison of the effective stress intensity range, ΔK_{eff}, of the ED2 configuration to that

predicted by the Rose model, ΔK_{Rose}, using an effective shorter patch as discussed in

Chapter 4. In comparison to the ED1 configuration presented earlier, the ED2

configuration ΔK_{eff} is in better agreement with ΔK_{Rose}. This is because the ED2

configuration (Figure 40), with only a 9 mm long end disbond, manages to maintain an

approximate elliptical shape, a major assumption of the Rose model. Both ΔK_{eff} and

ΔK_{Rose} for the ED2 configuration result in a 5 % reduction on ΔK_{CBP}.

The CD configuration, with a center disbond as shown in Figure 46, is expected to

provide an effective stress intensity range, ΔK_{eff}, between that of the full width disbond

(FWD) and the crack tip disbond (CTD) configurations. The CD configuration only

results in a 26 mm long disbond over the crack during crack growth within the patch while

the FWD configuration covers the entire patch width, therefore, ΔK_{eff}, for the CD

configuration is expected to be lower than that for the FWD configuration. In

comparison, the CD configuration disbond covers a greater portion of the crack as

compared to the CTD configuration during crack growth within the patch, therefore, the

ΔK_{eff} of the CD configuration is expected to be higher than that of the CTD configuration.

Averaging the ΔK_{eff} data presented in Table 30 for the FWD and the CTD configurations,

a rough estimate of 6.33 MPa$\sqrt{m}$ is obtained for the CD configuration. The actual ΔK_{eff}

for the CD configuration is presented in Table 33 along with the FWD and CTD

configurations. As can be seen from Table 33, ΔK_{eff} of the CD configuration, based on

Table 33. ΔK_{eff} for CD vs. FWD and CTD

Configuration	Disbond Size (≈ % of Total bond Area)	Location Weighting Factor, λ	ΔK_{eff} (MPa√m)
FWD	20	1.46	7.10
CD	10	1.35	6.56
CTD	20	1.15	5.56

the empirical approach, does fall between the FWD and CTD configuration as expected. This ΔK_{eff} is also only 3 % greater than the rough estimate of 6.33 MPa√m obtained from averaging the ΔK_{eff} values for the FWD and CTD configurations. Therefore, it can be concluded that when a greater portion of the crack is covered by a disbond during crack growth within the patch, the patching efficiency is lowered.

Size Effects. Based purely on disbond size, and not on disbond variation in the y-direction versus x-direction as shown in Figure 52, decreasing the center disbond of a CD configuration from 10 % to 5 % (Figure 56) is expected to exhibit similar behavior as decreasing a full width disbond of a FWD configuration from 10 % to 5 % as shown in Table 31. The weighting factors for the 10 % and 5 % disbond size for the CD configurations are presented in Table 34. As can be seen from Table 34, the size weighting factor, η, decreases by 26 % when the center disbond size is decreased from

Table 34. Disbond Size Weighting Factors for CD Configuration

Configuration	Disbond Size (≈ % of Total Bond Area)	Size Weighting Factor, η
CD	10	1.00
CD	5	0.84

10 % to 5 %. This is comparable to the 28 % decrease in η for the FWD configuration as shown in Table 31. Therefore, the proposed approach is reasonably appropriate.

Combining Disbond Location and Size Effects

Combining location and size effects results in the combined weighting factor, $\eta\lambda$, and ΔK_{eff} shown in Table 35. As presented in Chapter 4, the worst case disbond is the largest disbond around the crack (20 % FWD) while the disbond away from the crack

Table 35. Combined Location and Size Effects

Configuration[*]	Disbond Size (≈ % of Total Disbond Area)	Combined Weighting Factor, $\eta\lambda$	ΔK_{eff} (MPa√m)
CBP	0	1.00	4.86
FWD	20	1.46	7.10
FWD	10	1.40	6.80
FWD	5	1.20	5.83
CTD[♥]	20	1.15	5.60
ED1[♥]	20	0.97	4.71
ED2[♥]	20	0.95	4.62
CD	10	1.35	6.56
CD	5	1.13	5.49

[*]See Figure 3.
[♥]Assume $\eta = 1.0$ for these cases since only 20 % disbond size tested.

(ED1 and ED2) have no reduction in patching efficiency, assuming the end disbonds do not grow catastrophically.

The present approach can also be modified, if desired, using an additional weighting factor, γ, defined as

139

$$\gamma = \frac{\Delta K_{CBP}}{\Delta K_{Baseline}} \tag{23}$$

to relate the effects of disbond location and size back to the baseline panel without a patch.

The approach presented is one method of the several possible methods for quantifying the effect of disbond location and size on patching efficiency. This approach can be used for any given patch design to create tables of weighting factors based on disbond location and size. These tables would aid the aircraft repair designer and technician to make reasonable estimates of the reduction in patching efficiency due to disbonds in the bondline. This would allow a more accurate determination of inspection intervals as well as eliminating unnecessary repair and replacement of partially bonded patches that may damage the parent metallic structure or reduce the life of the patch through contamination of the bondline, etc.

VI. Conclusions and Recommendations

The purpose of this study was to investigate the effects of disbonds on the fatigue response of cracked aluminum panels repaired with bonded composite patches. For this purpose, the constant amplitude fatigue testing of precracked aluminum panels with partially bonded boron/epoxy composite patches was performed. Bondline defects/disbonds seen in real life applications due to service conditions or manufacturing errors were successfully simulated using teflon inserts.

The effects of disbond location and size were compared to a completely bonded patch and a cracked panel without a patch. It was found that a disbond around the crack resulted in greater crack growth rate and shorter life as compared to a disbond away from the crack and to a completely bonded patch. The level of patch efficiency reduction was a function of how much of the crack was covered by the disbond during crack growth inside the patch as well as the size of the disbond perpendicular to the crack. For a disbond spanning the full width of the patch, the crack growth rate within the patch was 1.65 times that of a completely bonded patch which resulted in a 30 % reduction in the overall fatigue life of the patched specimen. This increase in crack growth rate for a patch with a disbond around the crack is the result of displacing the point of load transfer between the plate and the patch away from the crack faces. In other words, for a completely bonded patch, the adhesive adjacent to the crack faces is loaded through shear resulting in load transfer away from the plate and a reduced crack opening displacement. When this point of load transfer is moved away from the crack in the presence of a disbond, more of the metallic structure

is free to be strained causing a greater crack opening displacement, and thus, a greater crack growth rate, i.e. a reduced patch efficiency. In comparison, a disbond away from the crack did not reduce patching efficiency, in fact, a disbond located at the longitudinal edge of the patch improved the repair efficiency by reducing the amount of parasitic load attraction into a shorter patch. No growth of the intentional disbonds was observed in any of the configurations tested. Only cyclic disbonding in the wake of the crack tip was seen, with most of the cyclic disbonding occurring after the crack tips had grown beyond the patch edges.

In addition, it was found that increasing the peak stress level resulted in an increased adhesive shear strain causing greater levels of cyclic disbonding about the crack faces and reduced specimen life. A higher stress ratio, R, reduced the repaired stress intensity factor range and increased patch efficiency, however, cyclic disbonding was similar for the same peak stress level because the adhesive shear strain is a function of the peak stress level. Modulus of adhesives demonstrated significant differences in bond durability. The higher modulus adhesive resulted in a greater reduction in the stress intensity factor, however, it exceeded the shear strain capability of the adhesive while the toughened lower modulus adhesive did not. This resulted in an increased level of cyclic disbonding and a reduced patch efficiency.

Ultrasonic C-SCANs proved to be very useful in evaluating the progression of the disbond during cycling, while thermal imaging using infrared equipment provided adequate real time disbond characterization. Unfortunately, the electric potential difference (EPD)

method was unsuccessful as an automated crack measurement tool due to electric shortening of the fracture surface in single-sided patched panels.

Although this work has made significant contributions to the understanding of the effects of disbond size and location on patching efficiency, much more work is required to obtain a more complete picture of disbond effects on the fatigue characteristics of cracked metallic structures repaired with bonded composite patches. For instance, to completely characterize disbond effects on patch repairs, partially bonded repairs to thicker, more highly loaded, panels such as wing panels is required. In addition a better understanding of the effect of adhesive modulus on disbond growth is required so that the optimum choice of adhesive can be made in varying repair situations. Finally, the effects of cure temperature on patch repairs should be fully characterized with varying the cure temperature, patch materials and adhesives employed to minimize thermal effects. These and many other questions must be answered before the complete adoption of "Crack Patching" as a viable repair technique can be achieved.

Appendix A: Fractured Specimens

This appendix includes photographs of the fractured specimens. The specimens are shown in sequential order starting with Specimen 2. All the patches failed by the patch failure mode as shown in Figure 28. Disbond locations as well as the teflon inserts are evident in some of the photographs. For clarification, Table 36 summarizes these specimens in regards to disbond location and size.

Table 36. Summary of Disbond Location and Size

Specimen	Configuration[*]	Disbond Size (% Total Bond Area)
2	CD	≈2.6
3	CBP	0
4	FWD	20
5	FWD	20
6	CTD	20
7	CTD	20
8	ED1	20
9	ED1	20
10	CBP	0
11	FWD	10
12	ED2	20
13	FWD	20
14	FWD	5
15	ED1	20
16	CD	10
17	CD	5
20	CBP	0
21	CBP	0
22	ED1	20
23	CBP	0
24	CBP	0
25	CBP	0
26	CBP	0

[*]See Figure 3.

144
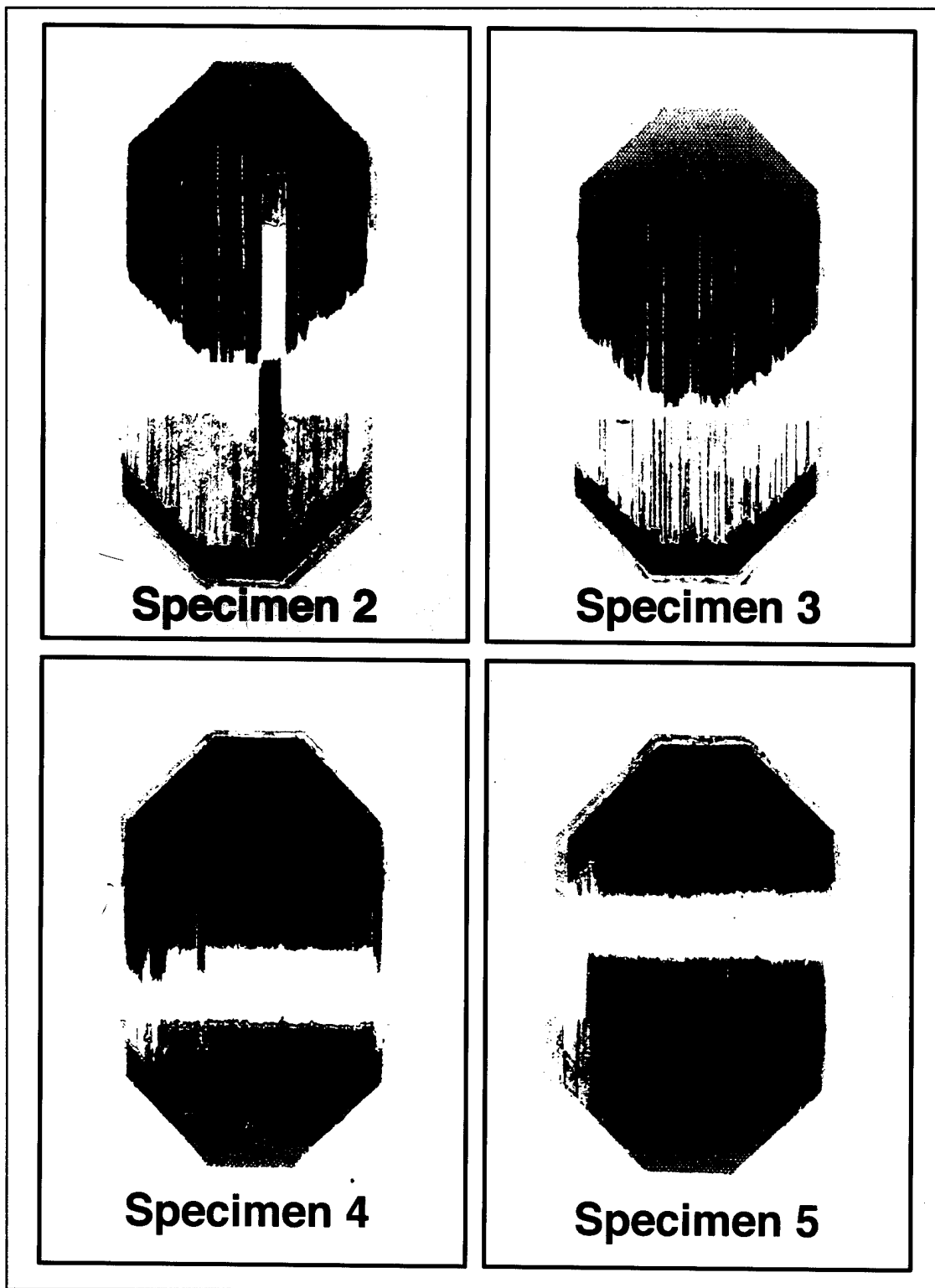
Figure 82. Specimens 2, 3, 4 and 5

145
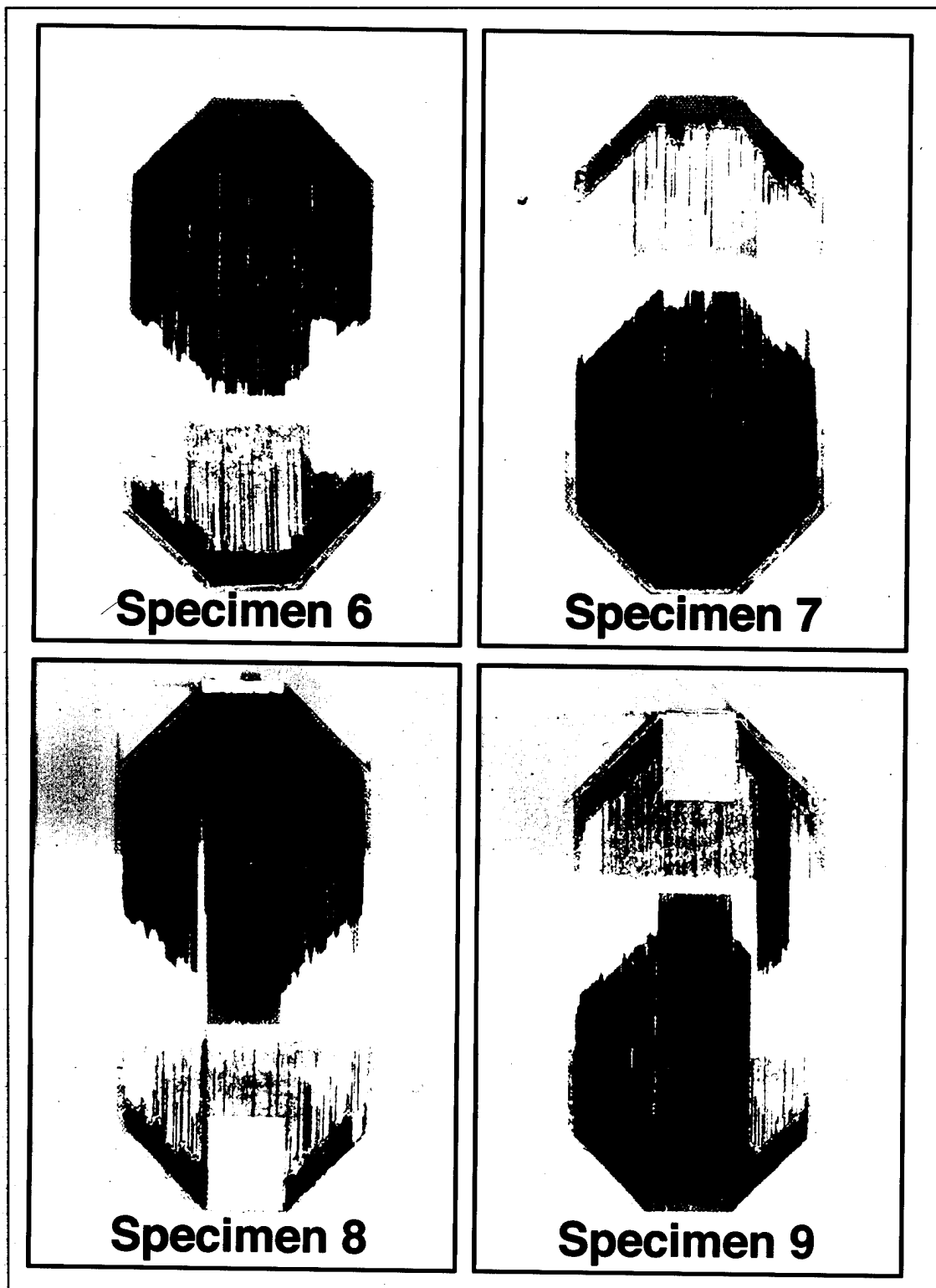
Figure 83. Specimens 6, 7, 8 and 9

146

Specimen 10

Specimen 11

Specimen 12
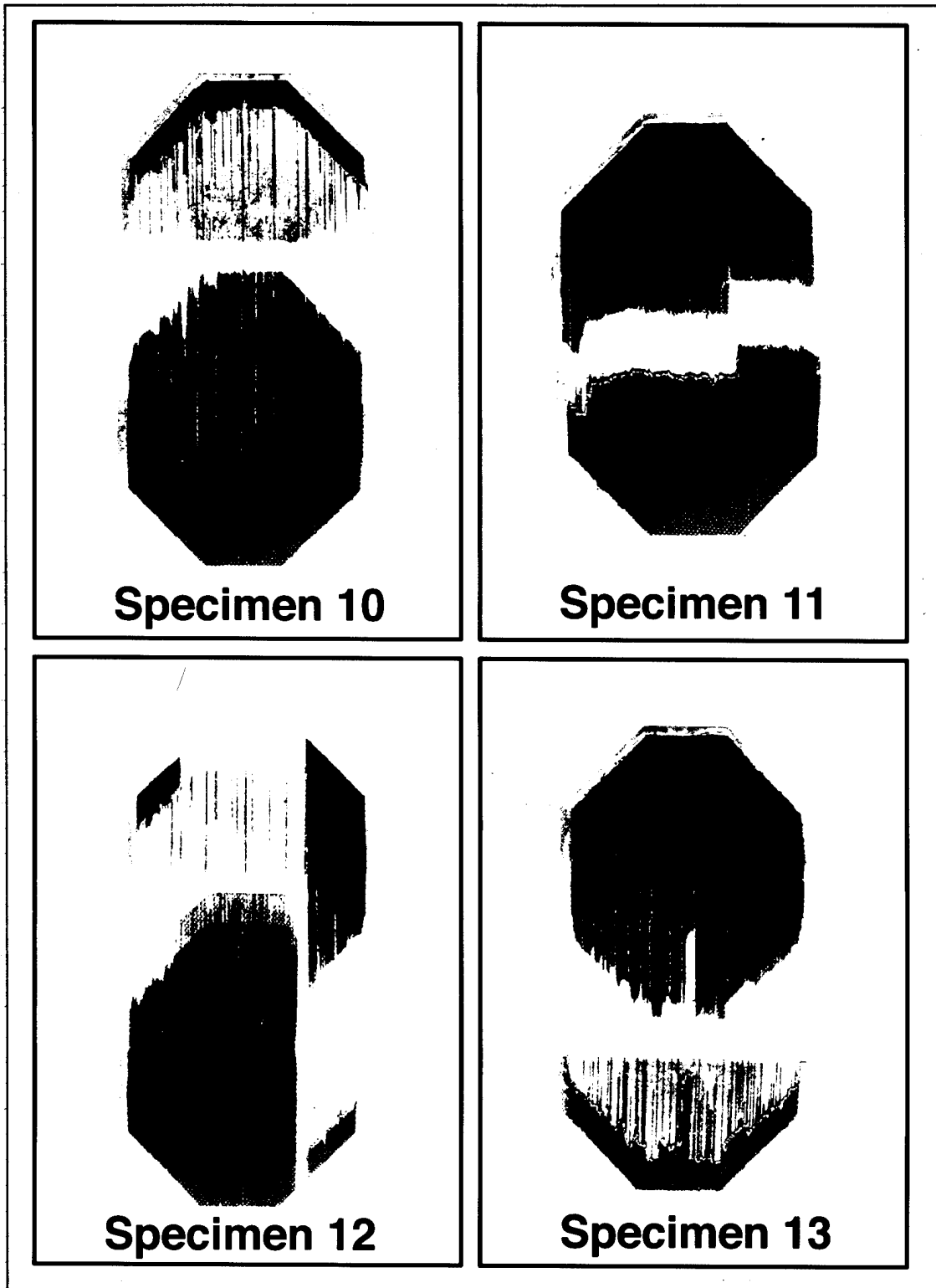
Specimen 13

Figure 84. Specimens 10, 11, 12 and 13

Specimen 14

Specimen 15

Specimen 16
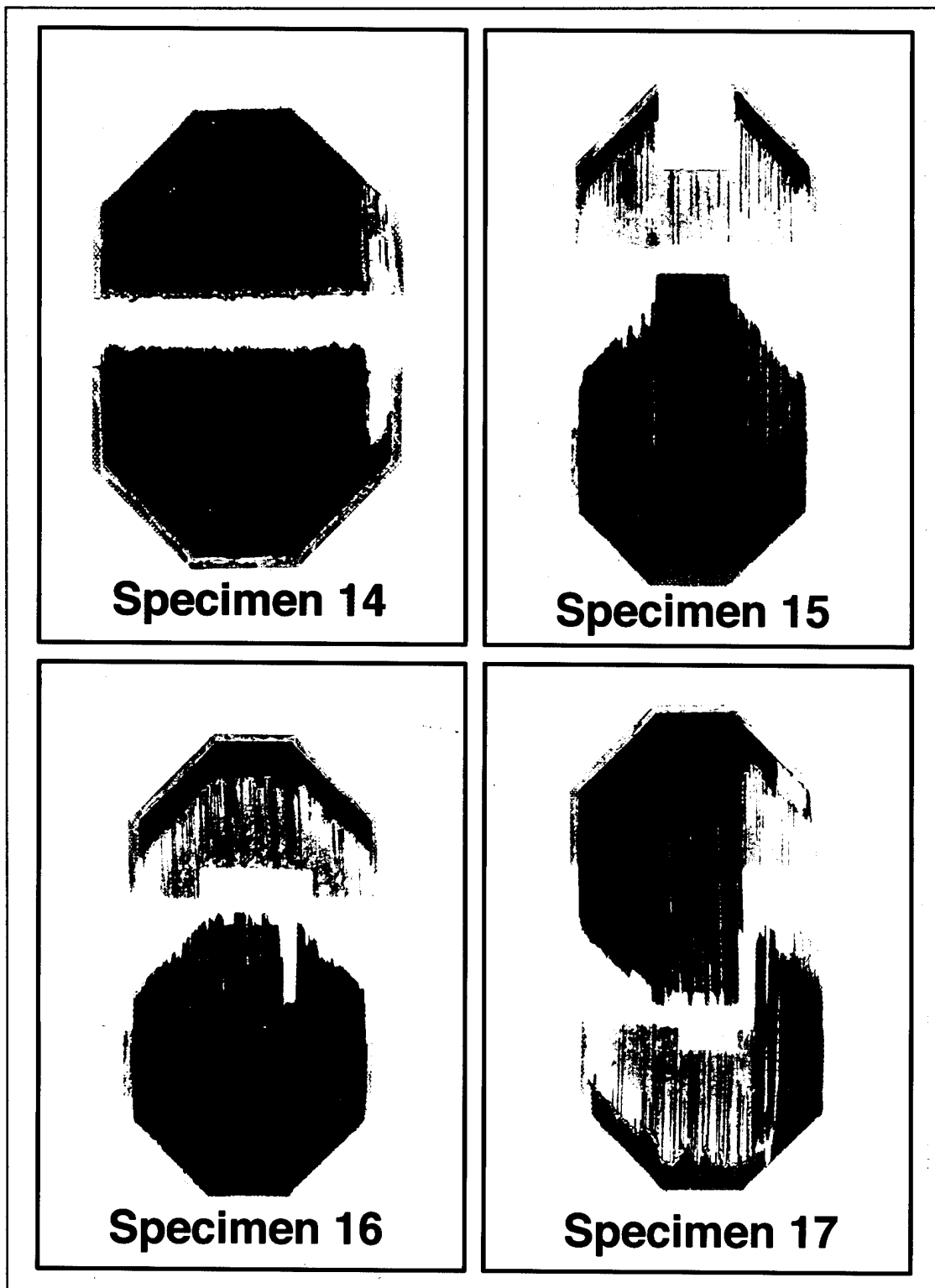
Specimen 17

Figure 85. Specimens 14, 15, 16 and 17

148

Specimen 20

Specimen 21

Specimen 22

Specimen 23

Figure 86. Specimens 20, 21, 22 and 23

149

Specimen 24

Specimen 25

Specimen 26

Figure 87. Specimens 24, 25 and 26

150

Appendix B: Crack Length Effects

This appendix briefly discusses the effects of repairing two different crack lengths with a completely bonded patch (CBP). According to Baker (8), the degree of crack growth retardation/reduction is a function of the relative decrease in the stress intensity factor from the unpatched case, $\Delta K = \Delta\sigma[\pi a]^{1/2}$, to the patched/repaired case, ΔK_R. From this and the assumption that the maximum repaired stress intensity factor range, ΔK_∞ (Figure 12), is independent of crack length, one can easily conclude, based on simple fracture mechanics theory, that the larger the pre-existing crack before repair the larger the reduction in the stress intensity factor after the repair. In other words, comparing the stress intensity f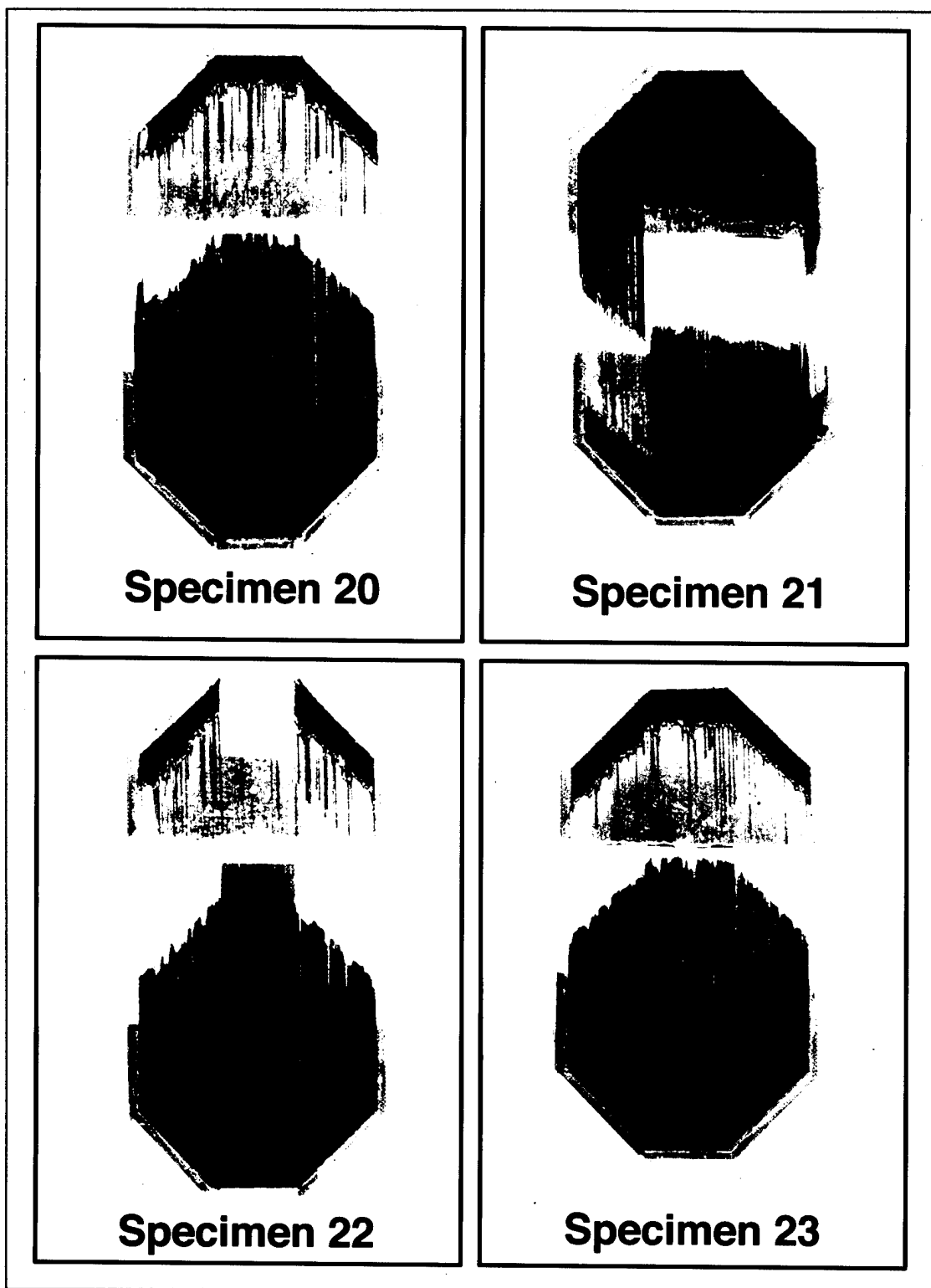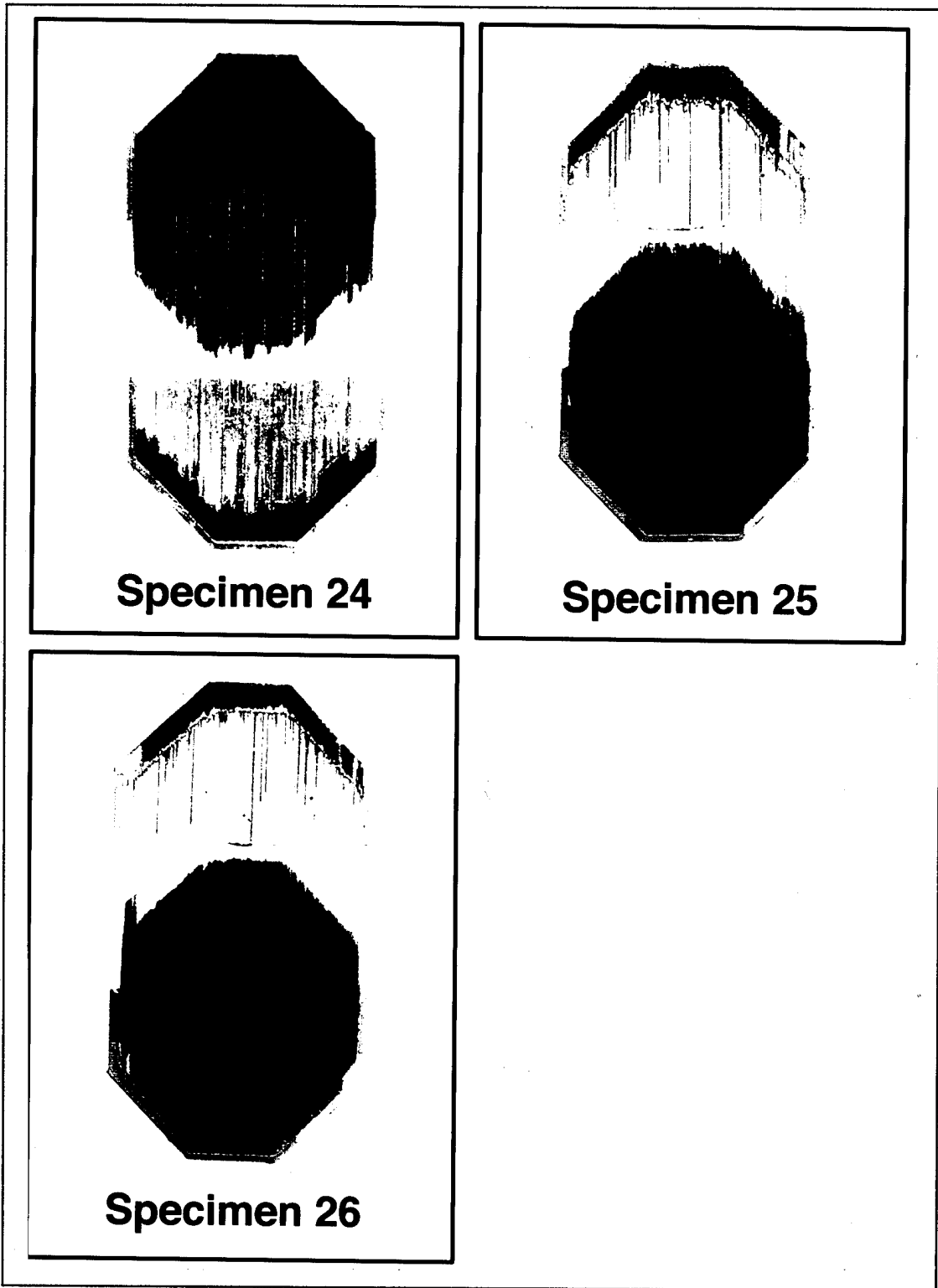actor range and the crack growth rates before and after repair would reveal a greater relative reduction for the longer crack length. Also, the crack growth rates after repair for both initial crack lengths should be approximately the same (6, 8, 33).

Four specimens, Specimens 23, 24, 27 and 28, were tested with crack lengths approximately one-half the length presented thus far. Two peak stress levels were also used with a baseline and CBP specimen fatigued at each stress level. The four specimens along with similar configurations with longer initial crack lengths are presented in Table 37. Also shown in Table 37 are the stress intensity factor ranges for the patched and unpatched cases as well as the crack growth rate data. In agreement with Baker (8), patching of the larger cracks resulted in a 77 % reduction in the stress intensity factor range while the shorter cracks resulted in a slightly lower than 70 % reduction. This was the case at both stress levels. Additionally, for each stress level, the repaired stress

Table 37. ΔK, ΔK$_R$ and da/dN for Different Initial Crack Lengths

Specimen	Configuration	Peak Stress (MPa)	Initial Crack Length (mm)	ΔK or ΔK$_R$ (MPa√m)	da/dN (mm/cycle)
1	Baseline	120	26.032	21.84	0.00136329
20	CBP	120	27.238	4.89*	0.00036265
21	CBP	120	26.355	4.88*	0.00036580
23	CBP	120	12.865	4.56*	0.00035319
27	Baseline	120	12.868	15.35	0.00080447
10	CBP	100	25.71	4.06*	0.00024812
18	Baseline	100	25.4	17.98	0.00068036
24	CBP	100	12.659	3.79*	0.00022194
28	Baseline	100	12.871	12.72	0.00034406

*ΔK$_R$ based on Rose model and initial crack length from Table 5.

intensity factor range, ΔK$_R$, was almost equal for the different crack lengths (6, 8, 33) while the unpatched stress intensity factor range, ΔK, was significantly different as expected from simple fracture mechanics theory. At both stress levels, the difference in ΔK$_R$ for the two crack lengths was approximately 7 % while the difference in ΔK was approximately 70 %. Therefore, the repaired stress intensity factor range, ΔK$_R$, was relatively constant for different crack lengths as proposed by Baker (6, 8) and Rose (33).

Figures 88 and 89 show the crack length versus cycles curves for the 120 MPa and 100 MPa tests for the varying initial crack lengths. As can be seen from these figures, the repaired crack growth rates for both initial crack lengths were similar within the patch, again supporting Baker's claim that patching efficiency is independent of crack length. The average crack growth rates within the patch are shown in Table 37. There was a greater reduction in repaired crack growth rate over the unrepaired crack growth rate for longer crack lengths which was expected because da/dN is dependent on ΔK in
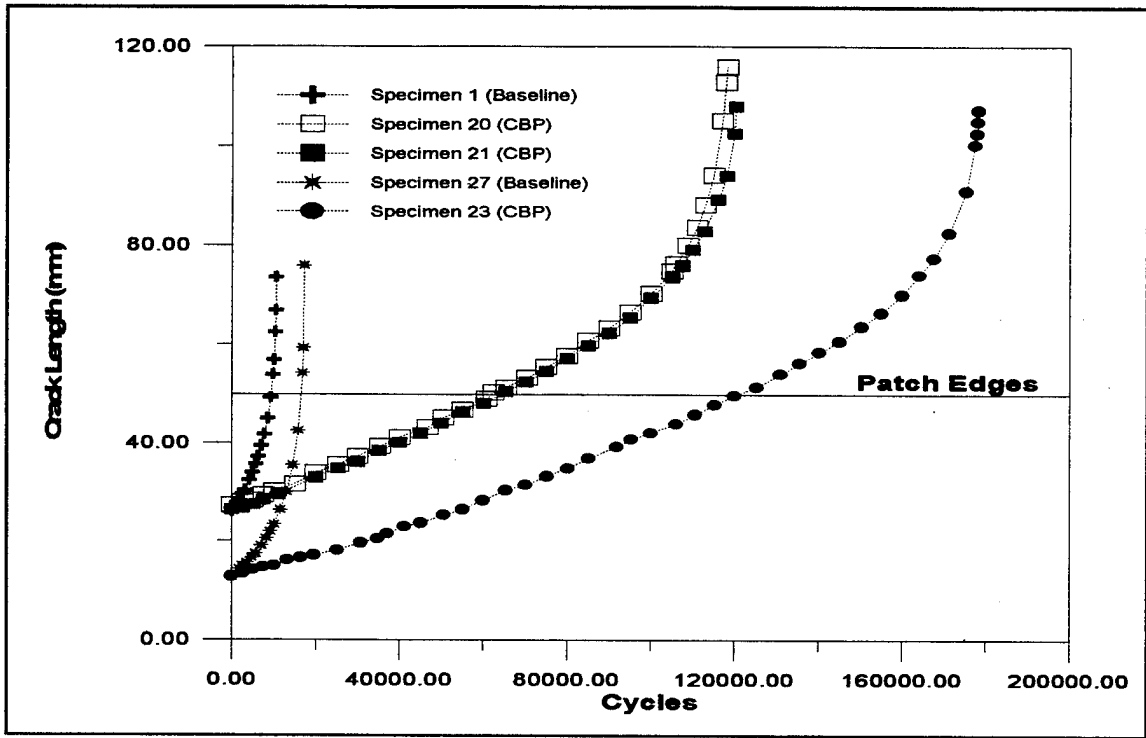
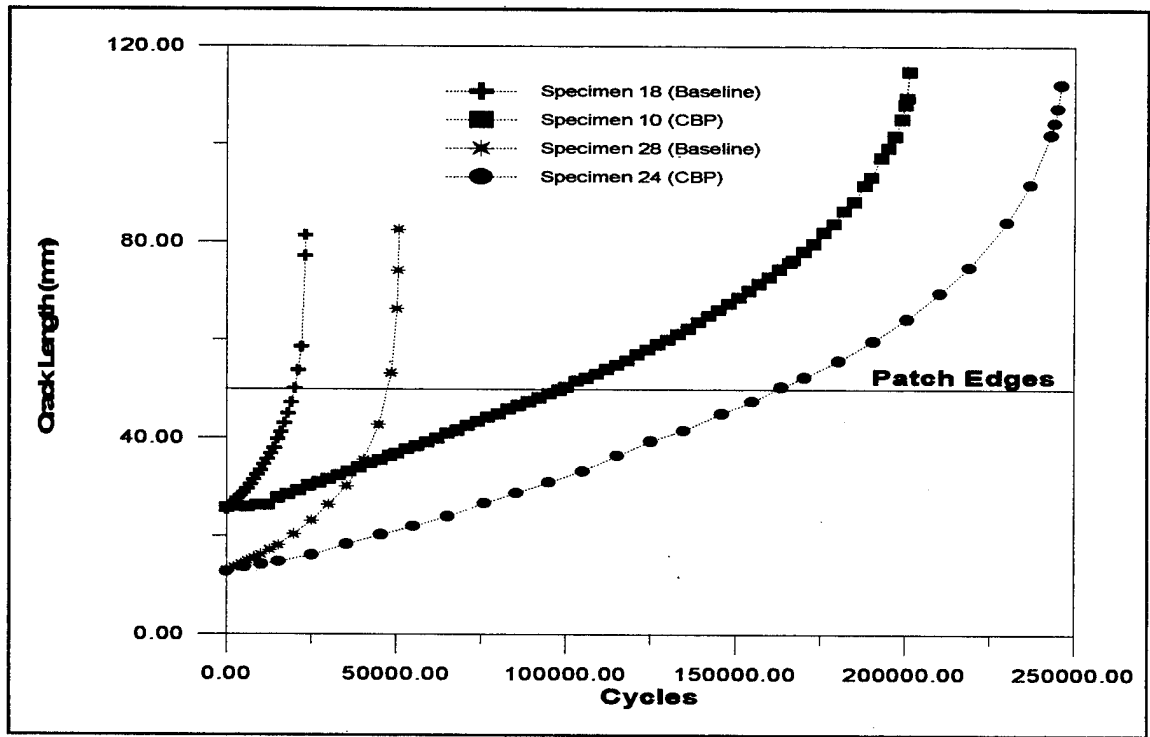**Figure 88. 120 MPa Crack Growth with Different Initial Crack Lengths**

Figure 89. 100 MPa Crack Growth with Different Initial Crack Lengths

accordance with Equation (16). The crack growth rates for the unrepaired cases were based on the first 5000 cycles of each specimen.

The bondline performance for the two shorter crack specimens was similar to that of the longer crack length specimens at both stress levels, i.e. insignificant cyclic disbonding during crack growth within the patch and increasing damage for crack growth outside the patch. Figure 90 shows the C-SCANs for Specimen 23 (120 MPa) and Specimen 24 (100 MPa). The Specimen 23 C-SCANs are for 0, 80,206 and 160,033 cycles corresponding to crack lengths of 12.865 mm (0.5065 inch), 34.831 mm (1.3713 inches) and 69.955 mm (2.75415 inches). The crack tips were still within the patch in the 80,206 cycle C-SCAN, therefore, very slight cyclic disbonding was observed with much higher levels of disbonding for crack growth outside the patch (160, 033 cycle C-SCAN). The 100 MPa CBP specimen (Specimen 24) C-SCANs revealed an interesting comparison to Specimen 10 (Figure 65) which was also fatigued at 100 MPa, however, Specimen 10's repair was applied to a longer initial crack length. For similar crack lengths, Specimen 24, starting with an initial crack approximately one-half the size of Specimen 10, demonstrated greater levels of cyclic disbonding for similar crack lengths. This was evident from the second and third C-SCANs for Specimen 24. This behavior occurred because Specimen 24, fatigued at the same stress level as Specimen 10, took significantly more cycles to reach the same crack lengths as a result of starting with a smaller initial crack length. Therefore, it can be concluded that cyclic disbonding is also a function of the number of cycles experienced in addition to peak stress level, stress ratio, and the adhesive shear modulus.

Specimen 23 (120 MPa)
0 Cycles

Specimen 24 (100 MPa)
0 Cycles

Specimen 23 (120 MPa)
80,206 Cycles

Specimen 24 (100 MPa)
163,665 Cycles

Specimen 23 (120 MPa)
160,033 Cycles

Specimen 24 (100 MPa)
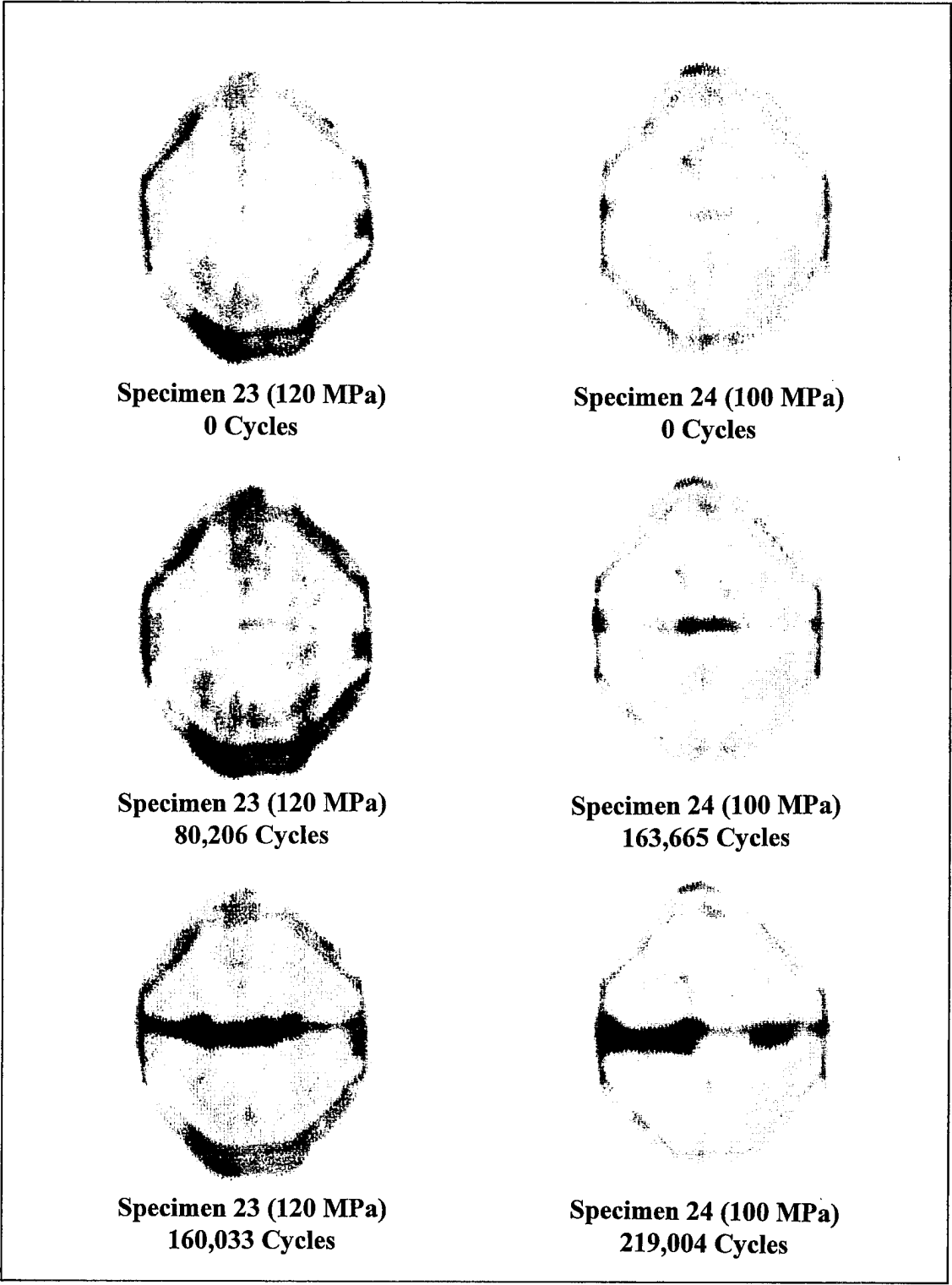**219,004 Cycles**

Figure 90. Specimen 23 and 24 C-SCANs

Bibliography

1.   Advanced Composite Program Office. Advanced Composites Repair Design Training Guide. McClellam AFB CA, March 1989.

2.   Air Force Flight Dynamics Laboratory. Primary Adhesively Bonded Structure Technology (PABST). Report No. AFFDL-TR-77-107. Wright-Patterson AFB OH, September 1978 (AD-AO77891).

3.   Air Force Joint Technology Applications Office. Composite Patches for Metallic Structures. No. TT-89034. Wright-Patterson AFB OH, 29 August 1989 (AD-B143611).

4.   "Air Frame Makers Use Aging Aircraft Experience to Refine Design Practices," Aviation Week and Space Technology: 110-111 (24 April 1989).

5.   American Society for testing and Materials. 1993 Annual Book of ASTM Standards: Metals Test Methods and Analytical Procedures. Vol. 03.01. Philadelphia: ASTM, 1993.

6.   Baker, A.A. "Bonded Composite Repair of Metallic Aircraft Components - Overview of Australian Activities," Proceedings of the 1994 AGARD Specialists' Meeting on Composite Repair of Military Aircraft Structures. Seville, Spain: October 1994.

7.   Baker, A.A. "Crack Patching: Experimental Studies, Practical Applications," Bonded Repair of Aircraft Structures. 107-172. A.A. Baker and R. Jones, editors. Dordrecht: Martinus Nijhoff Publishers, 1988.

8.   Baker, A.A. "Repair Efficiency in Fatigue-Cracked Aluminum Components Reinforced with Boron/Epoxy Patches," Fatigue and Fracture of Engineering Materials and Structures, 16: No. 7. 753-765 (1993).

9.   Broek, D. Elementary Engineering Fracture Mechanics (Fourth Revised Edition). Dordrecht: Kluwer Academic Publishers, 1991.

10.   Bureau of Accident Investigation. Aircraft Accident Report: Aloha Airlines Flight 243, Boeing 737-200, N73711, Near Maui, Hawaii, April 28, 1988. Report No. NTSB/AAR-89/03. Washington: National Transportation and Safety Office, 14 June 1989.

11.   Caruso, R. P. "Boron/Epoxy Composites for Aircraft Structural Repair," Composite Polymers, 4: 242-250 (1991).

12. Davis, M.J. "The Development of an Engineering Standard for Composite Repairs," Proceedings of the 1994 AGARD Specialists' Meeting on Composite Repair of Military Aircraft Structures. Seville, Spain: October 1994.

13. Ekstrom, M. "Bonded Repair of Aircraft Structures," Materials Evaluation, 50: 340-342 (March 1992).

14. Fotos, C. "Economic Impact of Aging Aircraft Fixes Remains Unclear," Aviation Week and Space Technology: 26-27 (29 May 1989).

15. Fredell, R. S. Damage Tolerant Repair Techniques for Pressurized Aircraft Fuselages. PhD dissertation. Delft University of Technology, Delft, The Netherlands, June 1994 (WL-TR-94-3134).

16. Fredell, R., R. Muller, and C. Borsboom. "Bonded Repair of Multiple Site Damage with GLARE Fiber Metal Laminate Patches," Proceedings of the 1994 USAF Aircraft Structural Integrity Program Conference. San Antonio, Texas: December 1994.

17. Fredell, R., W. van Barneveld and A. Vlot. "Analysis of Composite Crack Patching of Fuselage Structures: High Patch Elastic Modulus Isn't the Whole Story," Proceedings of the 39th International SAMPE Symposium and Exhibition. 610-623. Anaheim, California: April 1994.

18. Fredell, R., W. van Barneveld, and L.B. Vogelesang. "Design and Testing of Bonded GLARE Patches in the Repair of Fuselage Cracks in Large transport Aircraft," Proceedings of the 39th International SAMPE Symposium and Exhibition. 624-638. Anaheim, California: April 1994.

19. Gaffney, T. R. "Space Age Aids Span," The Dayton Daily News, 16 September 1995, sec. 4B.

20. Grabovac, I., R.A. Bartholomeusz, and A.A. Baker. "Composite Reinforcement of a Ship Superstructure - Project Overview," Composites, 6: 501-509 (1993).

21. Hart, K. "Today's Aircraft, Flying Tomorrow [Status of the USAF Flight Dynamics Directorate Approach to the USAF Aging Aircraft Problem]." Flight Dynamics Laboratory, Wright-Patterson AFB OH, 20 April 1995.

22. Hart-Smith, L.J. "Design and Analysis of Bonded Repairs for Metallic Aircraft Structures," Bonded Repair of Aircraft Structures. 31-47. A.A. Baker and R. Jones, editors. Dordrecht: Martinus Nijhoff Publishers, 1988.

23. Hysol Aerospace Products. <u>Structural Adhesives: EA-9394</u>. Company Product Brochure. Pittsburg, CA: Dexter Adhesives and Structural Materials Division, January 1991.

24. Jones, R. "Crack Patching: Design Aspects," <u>Bonded Repair of Aircraft Structures</u>. 49-76. A.A. Baker and R. Jones, editors. Dordrecht: Martinus Nijhoff Publishers, 1988.

25. Kelly, L.J. "Introductory Chapter," <u>Bonded Repair of Aircraft Structures</u>. 1-18. A.A. Baker and R. Jones, editors. Dordrecht: Martinus Nijhoff Publishers, 1988.

26. Mallick, P.K. <u>Fiber-Reinforced Composites</u> (Second Revised Edition). New York: Marcel Decker, 1993.

27. Mecham, M. "FAA Hiring Field Inspector to Monitor Aging Aircraft," <u>Aviation Week and Space Technology</u>: 110-111 (24 April 1989).

28. Muki, R. and Sternberg, E. <u>International Journal of Solids and Structures, 4</u>: 75-94 (1968).

29. "Old, New Aircraft Costs are Similar," <u>Aviation Week and Space Technology</u>: 95(24 July 1989).

30. Ott, James. "NTSB Raps Aloha, Aviation System for Fuselage Failure," <u>Aviation Week and Space Technology</u>: 24-26 (29 May 1989).

31. Ratwani, M. M. Characterization of Fatigue Crack Growth in Bonded Structure. Report No. AFFDL-TR-77-31. Vol. II. 55-64, June 1977.

32. Reinhart, T.J. "Surface Treatments for Bonded Repairs of Metallic Components," <u>Bonded Repair of Aircraft Structures</u>. 19-29. A.A. Baker and R. Jones, editors. Dordrecht: Martinus Nijhoff, Publishers, 1988.

33. Rose, L.F. "A Cracked Plate Repaired by Bonded Reinforcements," <u>International Journal of Fracture, 18</u>: No. 2. 135-144 (February 1982).

34. Rose, L.F. "An Application of the Inclusion Analogy for Bonded Reinforcements," <u>International Journal of Solids and Structures, 17</u>: 827-838 (1981).

35. Rose, L.F. "Theoretical Analysis of Crack Patching," <u>Bonded Repair of Aircraft Structures</u>. 77-105. A.A. Baker and R. Jones, editors. Dordrecht: Martinus Nijhoff Publishers, 1988.

36. Russel, A.J. "Fatigue Crack Growth in Adhesively Bonded Graphite/Epoxy Joints Under Shear Loading," Proceedings of the ASME Symposium on Advances in Adhesively Bonded Joints. 87-92. New York: ASME (1988).

37. "Standard Test Methods for Measurement of Fatigue Crack Growth Rates," ASTM E647, 1991.

38. Sun, C. T. and Arendt, C. "Bending Effect of Unsymmetric Adhesively Bonded Composite Repairs on Cracked Aluminum Panels," International Symposium of Advanced Structural Integrity Methods for Damage Tolerance. Hampton, Virginia, May 1994.

39. Swift, T. "Repairs to Damage Tolerant Aircraft," Structural Integrity of Aging Airplanes. 433-483. S.N. Alturi, editor. Heidelberg: Springer-Verlag, 1991.

40. United States Air Force Academy. CalcuRep for Windows: Beta Version. Colorado Springs: USAFA Department of Engineering Mechanics, May 1995.

41. United States Department of Transportation. Composite Repairs of Cracked Metallic Airframe Structures. DOT/FAA/CT-92/32. Atlantic City: FAA Technical Center, May 1993 (AD-A277680).

Vita

Captain Jason J. Denney ███████████████████████. He graduated from Satellite High School, Satellite Beach, Florida, in 1986. He then entered the University of Central Florida and graduated with a Bachelor of Science in Aerospace Engineering on 6 May 1991. Also on 6 May 1991, he was commissioned through the Air Force Reserve Officer Training Corp (ROTC). Captain Denney's first assignment was as a project engineer in the Titan System Program Office at Los Angeles AFB, California. During his time there, he served as the chief of the Titan II and Titan IV Liquid Rocket Engines (LREs) Section responsible for all LRE development, reliability, production, and flight programs. Captain Denney entered the Air Force Institute of Technology School of Engineering in May 1994.

Permanent Address: ████████████████

REPORT DOCUMENTATION PAGE

Form Approved
OMB No. 0704-0188

1. AGENCY USE ONLY (Leave blank)	2. REPORT DATE	3. REPORT TYPE AND DATES COVERED
	December 1995	Master's Thesis

4. TITLE AND SUBTITLE
FATIGUE RESPONSE OF CRACKED ALUMINUM PANEL
WITH PARTIALLY BONDED COMPOSITE PATCH

5. FUNDING NUMBERS

6. AUTHOR(S)

Jason J. Denney, Captain, USAF

7. PERFORMING ORGANIZATION NAME(S) AND ADDRESS(ES)

Air Force Institute of Technology, WPAFB, OH 45433

8. PERFORMING ORGANIZATION REPORT NUMBER

AFIT/GAE/ENY/95D-7

9. SPONSORING/MONITORING AGENCY NAME(S) AND ADDRESS(ES)

Mr. Michael L. Zeigler
WL/FIBEC
Wright-Patterson AFB OH 45433-7542

10. SPONSORING/MONITORING AGENCY REPORT NUMBER

11. SUPPLEMENTARY NOTES

12a. DISTRIBUTION/AVAILABILITY STATEMENT

Approved for public release; distribution unlimited

12b. DISTRIBUTION CODE

13. ABSTRACT (Maximum 200 words)
This research investigated the fatigue response of a precracked 508x152x1 mm 2024-T3 aluminum panel repaired with a partially bonded, unidirectional, three-ply boron/epoxy reinforcement with ply lengths of 68, 56 and 50 mm, and a width of 50 mm. Disbonds were simulated in the bondline of the repair using teflon inserts. The repaired panels were subjected to constant amplitude fatigue testing at a peak stress of 120 MPa. The effects of various disbond locations and sizes were investigated and compared to each other as well as to panels repaired with a completely bonded reinforcement and to cracked panels without any reinforcement. It was found that disbonds around the crack resulted in greater crack growth rates. The degree of repair efficiency reduction was a function of how much of the crack was covered by the disbond as well as the size of the disbond perpendicular to the crack. No pre-existing disbond growth was observed, only cyclic disbonding in the wake of the crack tip was evident, thus disbonds in front of or away from the crack did not reduce the repair efficiency. Even with severe disbonds equal to twenty-percent of the total bond area, the partially bonded repairs still provided significant improvement in fatigue life.

14. SUBJECT TERMS
Crack Patching, Aircraft Repair, Fatigue, Damage Tolerance, Adhesive Bonding, Surface Pretreatment, Aging Aircraft, Crack Arrest

15. NUMBER OF PAGES
175

16. PRICE CODE

17. SECURITY CLASSIFICATION OF REPORT	18. SECURITY CLASSIFICATION OF THIS PAGE	19. SECURITY CLASSIFICATION OF ABSTRACT	20. LIMITATION OF ABSTRACT
Unclassified	Unclassified	Unclassified	UL

GENERAL INSTRUCTIONS FOR COMPLETING SF 298

The Report Documentation Page (RDP) is used in announcing and cataloging reports. It is important that this information be consistent with the rest of the report, particularly the cover and title page. Instructions for filling in each block of the form follow. It is important to *stay within the lines* to meet *optical scanning requirements*.

Block 1. Agency Use Only *(Leave blank)*.

Block 2. Report Date. Full publication date including day, month, and year, if available (e.g. 1 Jan 88). Must cite at least the year.

Block 3. Type of Report and Dates Covered. State whether report is interim, final, etc. If applicable, enter inclusive report dates (e.g. 10 Jun 87 - 30 Jun 88).

Block 4. Title and Subtitle. A title is taken from the part of the report that provides the most meaningful and complete information. When a report is prepared in more than one volume, repeat the primary title, add volume number, and include subtitle for the specific volume. On classified documents enter the title classification in parentheses.

Block 5. Funding Numbers. To include contract and grant numbers; may include program element number(s), project number(s), task number(s), and work unit number(s). Use the following labels:

C	- Contract	PR	- Project
G	- Grant	TA	- Task
PE	- Program Element	WU	- Work Unit Accession No.

Block 6. Author(s). Name(s) of person(s) responsible for writing the report, performing the research, or credited with the content of the report. If editor or compiler, this should follow the name(s).

Block 7. Performing Organization Name(s) and Address(es). Self-explanatory.

Block 8. Performing Organization Report Number. Enter the unique alphanumeric report number(s) assigned by the organization performing the report.

Block 9. Sponsoring/Monitoring Agency Name(s) and Address(es). Self-explanatory.

Block 10. Sponsoring/Monitoring Agency Report Number. *(If known)*

Block 11. Supplementary Notes. Enter information not included elsewhere such as: Prepared in cooperation with...; Trans. of...; To be published in.... When a report is revised, include a statement whether the new report supersedes or supplements the older report.

Block 12a. Distribution/Availability Statement. Denotes public availability or limitations. Cite any availability to the public. Enter additional limitations or special markings in all capitals (e.g. NOFORN, REL, ITAR).

DOD - See DoDD 5230.24, "Distribution Statements on Technical Documents."
DOE - See authorities.
NASA - See Handbook NHB 2200.2.
NTIS - Leave blank.

Block 12b. Distribution Code.

DOD - Leave blank.
DOE - Enter DOE distribution categories from the Standard Distribution for Unclassified Scientific and Technical Reports.
NASA - Leave blank.
NTIS - Leave blank.

Block 13. Abstract. Include a brief *(Maximum 200 words)* factual summary of the most significant information contained in the report.

Block 14. Subject Terms. Keywords or phrases identifying major subjects in the report.

Block 15. Number of Pages. Enter the total number of pages.

Block 16. Price Code. Enter appropriate price code *(NTIS only)*.

Blocks 17. - 19. Security Classifications. Self-explanatory. Enter U.S. Security Classification in accordance with U.S. Security Regulations (i.e., UNCLASSIFIED). If form contains classified information, stamp classification on the top and bottom of the page.

Block 20. Limitation of Abstract. This block must be completed to assign a limitation to the abstract. Enter either UL (unlimited) or SAR (same as report). An entry in this block is necessary if the abstract is to be limited. If blank, the abstract is assumed to be unlimited.